MODELING AN ULTRA-SENSITIVE DETECTOR FOR LARGE AREA EXPERIMENTS

Shubham Verma
Roll No: MS13032

A dissertation submitted for the partial fulfilment of BS-MS dual degree in Science

Under the guidance of
Dr. Satyajit Jena

April 2018

Indian Institute of Science Education and Research Mohali
Sector - 81, SAS Nagar, Mohali 140306, Punjab, India

Certificate of Examination

This is to certify that the dissertation titled **"Modeling an Ultra-sensitive Detector for Large Area Experiments"** submitted by **Shubham Verma** (Reg. No. MS13032) for the partial fulfillment of BS-MS dual degree program of the Institute, has been examined by the thesis committee duly appointed by the Institute. The committee finds the work done by the candidate satisfactory and recommends that the report be accepted.

Dr. Sanjeev Kumar Dr. Kamal P. Singh Dr. Satyajit Jena
(Supervisor)

Dated: 20.04.2018

Declaration

The work presented in this dissertation has been carried out by me under the guidance of Dr. Satyajit Jena at the Indian Institute of Science Education and Research Mohali.

This work has not been submitted in part or in full for a degree, a diploma, or a fellowship to any other university or institute. Whenever contributions of others are involved, every effort is made to indicate this clearly, with due acknowledgement of collaborative research and discussions. This thesis is a bonafide record of original work done by me and all sources listed within have been detailed in the bibliography.

Shubham Verma
(Candidate)

Dated: April 20, 2018

In my capacity as the supervisor of the candidate's project work, I certify that the above statements by the candidate are true to the best of my knowledge.

Dr. Satyajit Jena
(Supervisor)

Acknowledgement

First and foremost, I would like to thank my thesis supervisor Dr. Satyajit Jena, without whose help and supervision, this thesis would have never been possible. The discussions that I had with him has enhanced my capabilities as a researcher.

I would also like to thank my thesis committee members Dr. Sanjeev Kumar and Dr. Kamal P. Singh for their valuable suggestions and criticism of my work.

I owe my deepest gratitude to Rohit Gupta and Nishat Fiza, PhD students at IISER Mohali for helping me with various discussions related to my work as well as for proofreading my thesis. I would like to mention my heartiest gratitude to all my lab members.

I would like to thank all my friends for supporting and helping me during the entire period of the project. I would like to acknowledge the moral support and encouragement, that I have received from my family.

Finally, I am thankful to IISER Mohali for providing me infrastructure and Computer Centre for all the technical support. I would like to acknowledge DST INSPIRE, Government of India for the financial support.

Shubham Verma
MS13032
IISER Mohali.

Abstract

Cosmic ray particles which hit the Earth's atmosphere, carrying information about the extra-terrestrial events are characterized by large flux and varying angular distribution which makes it necessary for detectors to have larger volumes for their detection. Same goes for detecting neutrinos, which are weakly interacting and have smaller interaction cross-section but carry useful physics. Charged particles with large flux produced in various ground-based particle accelerators (like in ALICE at LHC, CERN) also need to be detected precisely with good time resolution to identify their various properties. Thus, a detector which can have better time resolution and is also economical for use in large numbers is needed for detecting such particles. One such detector is *Multi-gap Resistive Plate Chamber (MRPC)* which is a gas ionization detector with improved time resolution (in picoseconds). Current work involves modeling a five-gap MRPC detector using Garfield simulation package where geometry has been prepared by providing various dimensional parameters, in order to optimize this detector for the best possible time resolution.

MRPC is a gas ionization detector with multiple gas gaps made up of highly resistive electrodes. MRPC was first conceptualized and developed in 1996. There is a single set of anode and cathode readout electrodes, placed at the outer surfaces of the two outermost resistive plates. The presence of multiple narrow sub-gaps with high electric fields results in faster signals on the outer electrodes, thereby boosting the detector time resolution. Advantages of MRPC over conventional Resistive Plate Chamber include improved time resolution of less than 100 picoseconds, reduced time jitters of the signal, improved rate capability, and it is economical to be used in large area experiments.

We have prepared a five-gap glass MRPC geometry of dimension 20 mm × 20 mm × 6.5 mm using Garfield simulation package. The geometry consists of 6 glass electrodes with dielectric constant 8. The width of outer two electrodes is 1 mm and that of inner four electrodes is 250 microns each separated by 200-micron gas-gap. Then above the outer electrodes, 50-micron conductive Graphite coat is present above which 200-micron insulating Mylar sheet is kept. Finally on each side, 18 readout strips with thickness and width as 1 mm and pitch 0.1 mm are kept in the perpendicular orientation. Then we have optimized

this MRPC by using various gas mixtures and electric fields to obtain time resolution in some 10's of picoseconds.

MRPCs are being used as Time-of-Flight (TOF) detectors devoted to charged hadron identification in the mid-rapidity region of the ALICE experiment at Large Hadron Collider (LHC). It is also being used in medical imaging as an efficient detector for the TOF based Positron Emission Tomography (PET), and also in Muon tomography with cosmic ray muons which is a novel technology for high-Z material detection in security services. Thus, R&D for optimizing the time resolution of MRPC is indeed necessary for bringing breakthroughs in detector technology which instead will help us not only for elementary particle identification but also for direct applications to various challenges which society faces in the sphere of science and technology.

Contents

List of Figures

Chapter 1

Introduction

1.1 High Energy Physics

1.1.1 Journey Through the History of Sub-atomic Particles

From time immemorial, people have been pondering over questions on the fundamental basis of the matter which we see around us and we ourselves are made up of. The earliest of the ideas on atom dates back to 6^{th} century BC and were studied by ancient Greek philosophers such as Democritus, Epicurus, and others, primarily from a natural philosophical point of view. Meanwhile, at the beginning of 18^{th} century, physicists such as Robert Boyle and Sir Isaac Newton studied gases and proposed a mechanical universe with small, solid masses in motion thereby suggesting the possibility of the existence of atoms. The idea that matter consists of smaller particles i.e., atoms gained physical credibility only in the beginning of 19^{th} century, when John Dalton, who was then working on stoichiometry (which deals with the calculation of relative quantities of reactants and products in a chemical reaction) came up with the conclusion that each chemical element was composed of a single and unique type of a particle which he and his contemporaries believed were the fundamental particles of nature and named them as 'atoms' which indeed comes from the Greek word *atomos*, meaning 'indivisible' or 'uncut'. Then, towards the end of 19^{th} century, physicists discovered that the atoms proposed by Dalton indeed are not the fundamental particles of nature and are consists of even smaller particles. Between 1879 and 1897, through the works of William Crookes, Arthur Schuster and J.J. Thomson, *Electron* was discovered which we now know is a constituent of an atom and it soon was established to be the first elementary particle (indivisible) to be discovered. The term *Electron* was proposed by George Johnstone Stoney which he referred to as 'fundamental unit quantity of electricity'.

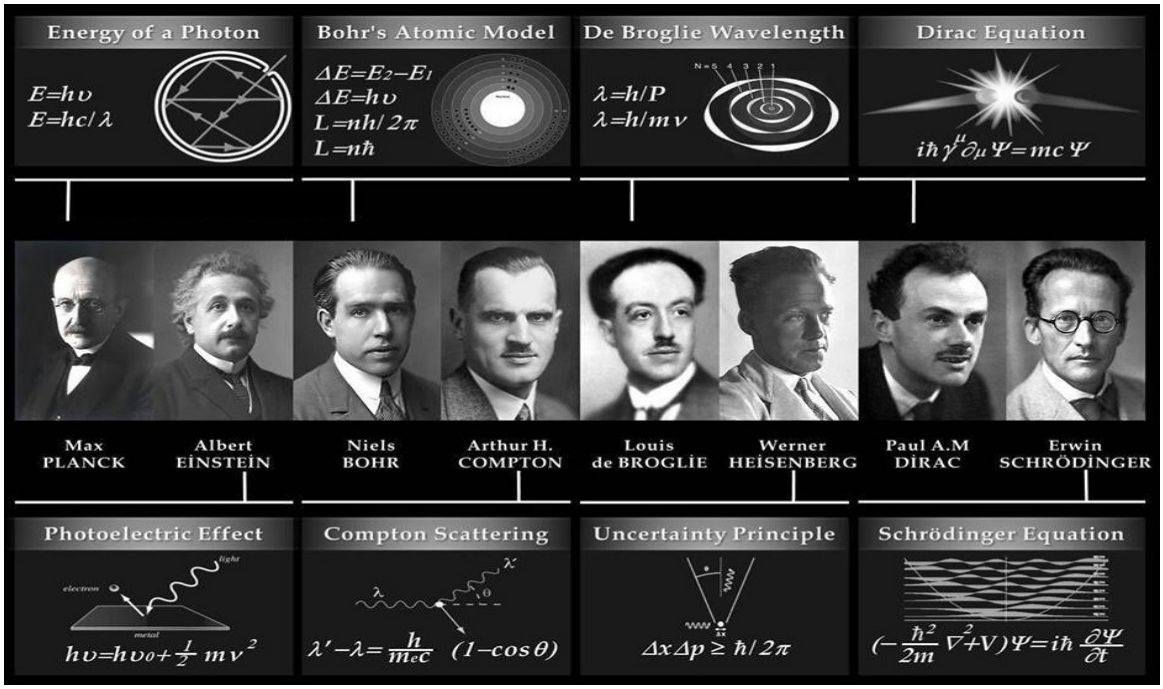

Figure 1.1: History of Atomic theory.

Then the inception of Quantum Theory by Max Planck who suggested that radiation is *quantized* i.e., it comes in discrete packets of energy back in 1900, which was carried forward by Albert Einstein who introduced photo-electric effect in 1905. Einstein also explained the Brownian motion which occurs due to the bombardment of molecules using Kinetic Theory and then Francois Perrin used Einstein's formula and measured Avogadro's number thereby proving the existence of atoms in 1907. Then in 1911, Ernest Rutherford along with Hans Geiger and Ernest Marsden, working on his famous gold foil experiment formulated the *Rutherford Model* of the atom, according to which a small positively charged nucleus carrying most of the atom's mass is orbited by low-mass electrons. Experiments by other physicists such as Henry Moseley, James Franck, and Gustav Hertz supported Rutherford's discovery that an atom has a positively dense nucleus surrounded by lighter electrons, thereby establishing the structure of atom by 1914. Then, in order to explain as to how atoms are stable, though the classical theory predicts that the electron releases electromagnetic radiation while orbiting a nucleus thereby losing its energy and would eventually collapse into the nucleus, Niels Bohr in 1913 proposed an atomic model known as Bohr's Model of the atom, using the quantum theory suggesting that the electrons travel in specific orbits (with definite energies) around the nucleus and that outer orbits can hold more electrons than the inner orbits and that these orbits determine the chemical properties of the atom. In 1917-19, Rutherford used alpha-particles to bombard heavy elements and saw H-particles kicked off from all of them, thereby proving that hydrogen nucleus is present

in other nuclei, which is regarded as the discovery of *proton*. Meanwhile, the wave-particle duality of electrons proposed by Louis de Broglie in 1924, Uncertainty Principle by Heisenberg in 1925, Schrodinger's famous wave equation governing the propagation of probability wave function of a quantum system, the existence of anti-particles proposed by Paul Dirac in 1928 by combining relativity and quantum mechanics followed by an experimental discovery of positron (which has same mass that of an electron but opposite charge) in 1932 by Carl David Anderson etc. helped us understand the mysterious governing the quantum world. In 1932 James Chadwick discovered the *neutron* (a charge-less particle with the mass slightly larger than proton which also constitutes the nucleus of an atom), thereby completing the structure of an atom. But, there was a lot to dig out of the atom.

In order to explain the continuous distribution of energy of the electrons emitted in beta decay, Wolfgang Pauli postulated the existence of the *neutrinos* (a charge-less elementary particle with much smaller mass than other particles) in 1930. The term *neutrino* was coined by Enrico Fermi who in 1934 proposed a theory of beta decay (in which he applied the principles of quantum mechanics to matter particles) which introduces the *weak interaction*. With this, begins the never-ending story of modern particle physics. Before 1934, only two kinds of fundamental interactions were known i.e, the gravitational and the electromagnetic interactions. With the introduction of weak interaction which causes radioactive decay, physicists were keen to explore the possibilities of more such fundamental interactions. Then, from 1932 to 1950s, the studies of cosmic rays (high-energy particles arriving from the outer space) opened the door to a world of new particles beyond the confinement of an atom and variety of new particles were discovered such as positron in 1932, the muon in 1937, followed by kaon, pion and many more. Then, upon the advent of high-energy particle accelerators in the early 1950s, a variety of particles were found in collisions of particles from increasingly high-energy beams which is referred to as *particle zoo*. The step towards classifying the variety of new particles discovered and explain the fundamental interactions between them comes out in the form of the Standard Model of Particle Physics.

1.1.2 The Standard Model

The Standard Model of particle physics which was developed in the early 1970s, encapsulates our basic understanding of the new particles discovered using various experimental facilities and the interaction of these particles with three of the four fundamental forces i.e., electromagnetic, strong and weak nuclear forces. Fitting gravity into the framework of the Standard Model has been a difficult challenge and a lot of attempts is still underway for this inclusion. Since, on an atomic scale, the effect of gravity is so weak as to be negligible, which is why the Standard Model still works well despite the exclusion of one of the four

fundamental forces.

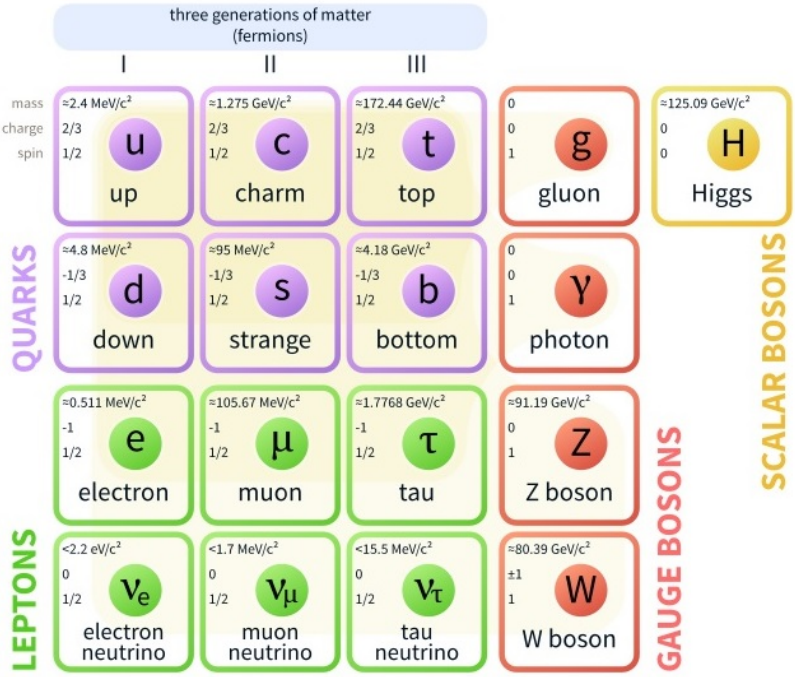

Figure 1.2: The Standard Model of particle physics.

Figure 1.2 gives an overview of the Standard Model of Particle Physics. As per the Standard Model, two major categories of particles are the *fermions*, from which all the known matter is built up, and the *bosons*, which mediate interactions between the fermions.

The fermions are subdivided into six *leptons* (electron, muon, tau and the corresponding three leptonic flavors of neutrinos) and six *quarks* (up, down; charm, strange; top, bottom). The leptons are only affected by electroweak interaction which is the unification of electromagnetic and weak interactions, whereas the quarks also interact through the strong forces. Both these groups i.e., leptons and quarks are further split into three generations as shown in figure 1.2. The lightest and the most stable particles constitute the first generation of particles, whereas the heavier particles which are usually less stable belong to the second and third generations. Thus, most of the known matter is made up of the particles from the first generation. The three charged leptons i.e., the electron, the muon, and the tau have sizable mass whereas the three neutrinos are charge-less and have very less mass. All fermions have half-integer spin and obey the Fermi-Dirac Statistics.

The bosons are the force-carrier particles whose exchange results in the fundamental forces. The four fundamental forces work over different ranges and have different strengths. Each fundamental force has its own corresponding boson, as in the 'photon' is the force-carrying particle for the electromagnetic interaction, the strong force is carried by the 'gluon' and weak force is carried by 'W and Z bosons'. The 'graviton' is hypothesized as the force-

carrying particle for the gravitational interaction, but its existence is not yet known. Figure 1.3 shows the properties of the bosons for the four fundamental forces.

Property \ Interaction	Gravitational	Weak (Electroweak)	Electromagnetic (Electroweak)	Strong: Fundamental	Strong: Residual
Acts on:	Mass – Energy	Flavor	Electric Charge	Color Charge	See Residual Strong Interaction Note
Particles experiencing:	All	Quarks, Leptons	Electrically charged	Quarks, Gluons	Hadrons
Particles mediating:	Graviton (not yet observed)	W^+ W^- Z^0	γ	Gluons	Mesons
Strength relative to electromag for two u quarks at: 10^{-18} m	10^{-41}	0.8	1	25	Not applicable to quarks
Strength relative to electromag for two u quarks at: 3×10^{-17} m	10^{-41}	10^{-4}	1	60	
for two protons in nucleus	10^{-36}	10^{-7}	1	Not applicable to hadrons	20

Figure 1.3: Fundamental forces and properties of corresponding bosons.

On 4th of July 2012, a new particle was observed in the mass between 125 and 127 GeV/c^2 in the ATLAS and CMS experiments at CERN's Large Hadron Collider (LHC), which is found to be consistent with the Higgs boson, yet another elementary particle in the Standard Model. Higgs boson is the quantum excitation of the scalar Higgs field or in another way it is a visual manifestation of the Higgs field which pervades the entire universe and has a non-zero value in the vacuum, unlike other fields (such as electromagnetic field). In 1964, three groups of researchers (Robert Brout and François Englert; Peter Higgs; Gerald Guralnik, C. Richard Hagen, and Tom Kibble) independently published papers which show how gauge bosons acquire non-zero masses as the result of spontaneous symmetry breaking within electroweak theory and suggested the existence of an unusual *field* for such a symmetry breaking. The field required is known as the *Higgs field* and the mechanism by which it led to the breaking of symmetry is known as Brout-Englert-Higgs mechanism (Higgs mechanism). The discovery of Higgs boson in 2012 is significant as it helps us to understand as to how fundamental particles acquire mass and why do they have different masses, which is quite evident from that the 2013 Nobel Prize in physics was awarded to Peter Higgs and François Englert for their work on Higgs mechanism. Since Higgs field is scalar, Higgs boson has zero spin angular momentum. It has even-parity and it is its own anti-particle. It will take further work to establish that this discovery is the Higgs boson predicted by the Standard Model of Particle Physics. The story doesn't end here, perhaps this is the beginning towards discovering more particles and related interactions which make up the Universe. The elementary particles in the standard model make up all the known matter in the Universe. *Hadrons* which are composite particles made of quarks held together by the strong force, are of two types - *baryons* which are made of three quarks (a proton is a baryon consisting of two 'up' and one 'down' quarks and also the neutron which consists of one 'up' and two 'down' quarks), and *mesons*, made of one quark and one anti-quark (the pion is a meson consisting of one 'up' quark and one 'anti-down' quark).

1.1.3 Shortcomings of the Standard Model

With the discovery of Higgs boson in 2012, all the elementary particles predicted by the Standard Model seem to have been observed, but the story of elementary particle physics is far from over. Maybe it is only the part of a bigger picture hidden deep in the subatomic world and we have a long way to know about the Universe we live in and what it is made up of. Following are some of the inadequacies of the Standard Model which motivate physicists to build bigger experimental set-ups and go beyond the regime of the Standard Model in quest of the theories which can describe the Universe exclusively,

- The Standard Model doesn't account for the gravitational interaction. The Model is inconsistent with the theory of general relativity in the sense that one or both theories break down within the known space-time singularities such as the black hole event horizon and the Big Bang.
- The mathematical structure of the Standard Model does not have a verified and more fundamental explanation.
- According to the cosmological observations, *dark matter* (an unknown type of matter which pervades the Universe and is not yet observed which is why, it is called as 'dark' matter) and *dark energy* (again an unknown form of energy which permeate all of space and is believed to cause accelerated expansion of the Universe) constitute 95.1% of total mass-energy content of the Universe. The Standard Model provides no suitable candidate for the dark matter and neither account for dark energy.
- As per the Standard Model, neutrinos are massless, but the experimental discovery of *neutrino oscillation* at Super-Kamiokande Observatory in Japan, led by Takaaki Kajita and Sudbury Neutrino Observatories in Canada, led by Arthur B. McDonald in 2001, has shown that neutrinos indeed have mass thereby paving a way to the physics beyond the Standard Model. It also doesn't account for the neutrino mass hierarchy problem.
- It doesn't account for the question that why the Universe is made up of mostly matter, though the Model predicts that matter and anti-matter should have been created in almost equal amounts at the beginning of the Universe. In order to find an explanation for this matter-antimatter asymmetry, physicists have to go beyond the regime of the Standard Model.

Several attempts are being done to unify the relativity and the Standard Model with the hope to combine the four fundamental forces of nature into a *Theory of Everything*. Physicists are

also trying hard to unify the existing electroweak and strong forces (which are still separate in the Standard Model) of the Standard Model into a *Grand Unified Theory*.

A theoretical framework called *supersymmetry* (SUSY), which predicts the existence of *supersymmetric particles* (abbreviated as 'sparticles') for every particle in the Standard Model, might help to get answers to the above questions which the Standard Model is unable to account for. Each particle in the Standard Model would have a sparticle with its spin differing by half from the ordinary particle, for example, fermions having boson partners and vice versa. The sparticles are predicted to be much heavier than their counterparts which is why the existing particle colliders may not be very powerful to produce them. Thus, in order to search for the physics Beyond the Standard Model (BSM), continuous efforts are needed to develop powerful accelerators and more sensitive detectors in the following years.

1.2 Experiments in High-Energy and Astro-Particle Physics

1.2.1 Collider Based Experiments in High Energy Physics

Modern High Energy Physics Experiments generally use a beam of charged particles accelerated at very high kinetic energies either linearly or in a circular fashion so as to hit a target or collide with another beam coming from opposite direction. This collision gives rise to a pool of yet another particles which are then detected using various particle detectors and are then analyzed to find various physics results. Figure 1.4 shows some of the particle colliders at work along with various other parameters like the colliding particles, luminosity, particle energies etc.

1.2.2 The Large Hadron Collider (LHC)

At present, the largest and the most powerful particle accelerator in the world is the Large Hadron Collider (LHC) situated at CERN (European Organization for Nuclear Research) on the France-Switzerland border near Geneva. LHC lies in a tunnel which is 27 Kilometers in circumference underground with a mean depth of 100 m. Circular particle accelerators such as LHC, consist of radio frequency cavities that accelerate charged particles and superconducting magnets which maintain the circular orbit of these particles. Currently (LHC run resumed in 2015 until present) at LHC, two beams of proton, with each beam consisting of 2808 bunches (and each bunch consisting of 10^{11} protons), are accelerated to 0.999999991 times the speed of light with 6.5 TeV of kinetic energy per proton and are

Accelerator	Centre, city, country	First operation	Accelerated particles	max energy per beam, GeV	Luminosity, 10^{30} $cm^{-2}s^{-1}$	Perimeter (length), km
VEPP-2000	INP, Novosibirsk, Russia	2006	e^+e^-	1.0	100	0.024
VEPP-4M	INP, Novosibirsk, Russia	1994	e^+e^-	6	20	0.366
BEPC II	IHEP, Beijing, China	2008	e^+e^-	3.7	700	0.240
DAFNE	Frascati, Italy	1999	e^+e^-	0.7	436[12]	0.098
KEKB	KEK, Tsukuba, Japan	1999	e^+e^-	8.5 (e-), 4 (e+)	21100	3.016
RHIC	BNL, United States	2000	pp, Au-Au, Cu-Cu, d-Au	100/n	10, 0.005, 0.02, 0.07	3.834
LHC	CERN	2008	pp, Pb-Pb, p-Pb, Xe-Xe	6500 (planned 7000), 2560/n (planned 2760/n)	15000, 0.003, 0.9	26.659

Figure 1.4: Particle Colliders and their Parameters.

collided at around 13 TeV center of mass energy of proton-proton collision. As the bunches of protons reach the collision points, they are squeezed to about 20 microns (the human hair is around 50 microns thicker) for proton-proton (p-p) collision and this is where the significance of 13 TeV collision energy is apparent which is concentrated in such a tiny region. The spacing between the bunches is 25 nanoseconds (ns), that means after every 25 ns there is a p-p collision. At LHC, bunches cross on average around 30 million times per second, thereby generating 1 billion particle collisions per second (because of the very tiny size of the colliding particles). These collisions result in a shower of a large number of particles which are then detected using various particle detectors. The two beams collide at four detectors - ALICE, ATLAS, CMS, and LHCb as shown in figure 1.5 which gives the basic layout of the LHC at CERN. Each of these detectors has specific physics goals and corresponding detector system.

To search exotic particles like the Higgs boson, supersymmetric particles, candidates for dark matter and dark energy; providing answers to questions on matter-antimatter asymmetry; understanding Quark-Gluon-Plasma (QGP) to better understand the beginning of the Universe are some of the main physics goals of the LHC at CERN. In order to increase the potential of discoveries after 2025, the LHC aims to upgrade its apparatus by increasing the luminosity by a factor of 10 beyond its design value i.e., it targets to achieve a peak luminosity of $5 \times 10^{34}\ cm^{-2}\ s^{-1}$, thereby significantly increasing the particle rate. Thus, R&D for advanced detector technology is needed to cope up with this increased particle rate in HL-LHC. Hopefully, this upgrade of the LHC will help us to get answers to unsolved mysteries in particle physics today.

The Large Hadron Collider is one example for experiments based on colliders in particle

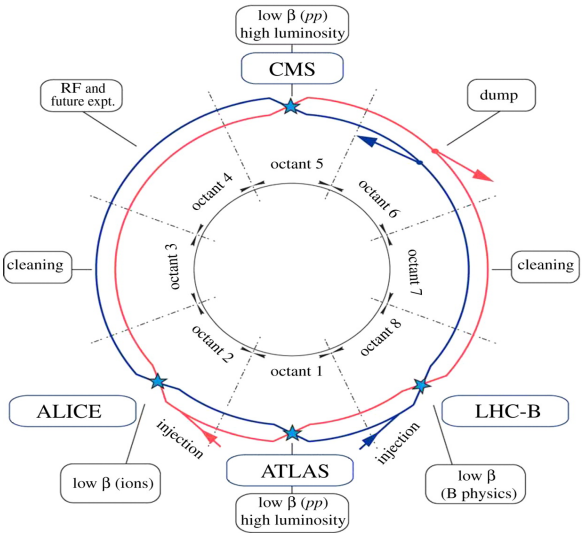

(a) Schematic representation of the LHC layout.

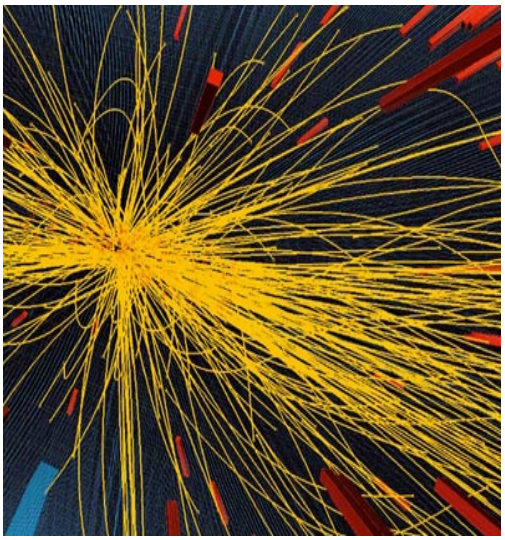

(b) A 7 TeV proton-proton collision in CMS yielding more than 100 charged particles.

Figure 1.5: LHC Layout and a proton-proton collision event at CMS.

physics. There are also various non-collider based experiments in particle and astroparticle physics which use cosmic-rays as the source of incoming particles which instead help us to know about various extra-galactic phenomena as well as physics of elementary particles.

1.2.3 Non-Collider Experiments

In order to study various components of cosmic-rays, measurements of neutrino oscillation, and searches for neutrinoless double beta-decay, magnetic monopoles and dark matter candidate etc., non-collider experiments have become increasingly important in particle physics.

Cosmic-rays are high-energy particles coming from outer space which strike the Earth's atmosphere with varying angular distribution and large flux. The primary cosmic-rays mainly consist of protons (90%), alpha particles (9%) and other heavy nuclei (1%) [Gai90]. These primary cosmic-rays collide with the nuclei of atoms in the upper atmosphere, thereby creating secondary particles which include protons, neutrons, pions (both charged and neutral), kaons, photons, electrons and positrons as shown in figure 1.6. The charged pions decay with a proper lifetime of 26 ns to muons and muon-neutrinos. The muons travel unimpeded through the atmosphere, with their flux at sea-level being one muon per square centimeter per second, thereby constituting the major part of the cosmic-rays at the sea level. The primary cosmic-ray energies range from 10^8 eV to 10^{20} eV, which is far higher than the beam energy of the LHC. The rate of the arrival of cosmic rays at the top of the atmosphere

falls off with increasing energy (the rate approximately falls off with increasing energy as $E^{-2.7}$), from 10,000 particles per square metre per second at 1 GeV of energy to less than one particle per square kilometre per century for the highest energy particles [Ref].

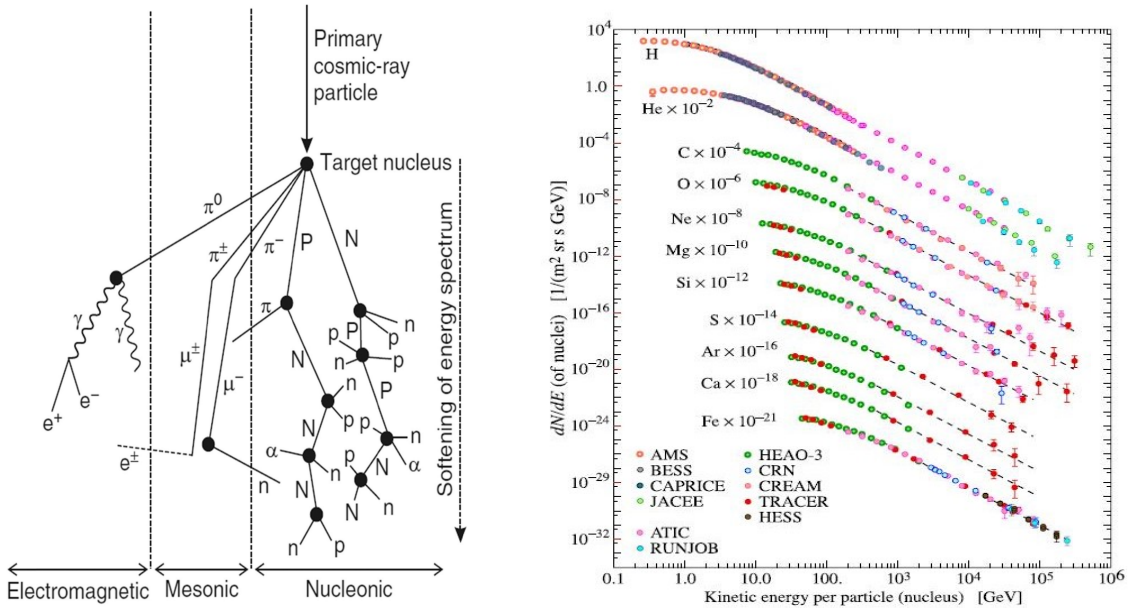

(a) Schematic representation of the interaction of primary cosmic-rays in the upper atmosphere.

(b) Fluxes of nuclei of the primary cosmic radiation in particles per energy-per-nucleus are plotted vs energy-per-nucleus. The figure was created by P. Boyle and D. Muller.

Figure 1.6: Interaction of Primary Cosmic-ray particles in upper atmosphere and Primary Cosmic-ray Flux.

Studying various properties of the incoming cosmic-rays can provide us information on extra-galactic events, which is why detecting and measuring various parameters of these particles becomes essential to unfold various mysterious of the far-reaching cosmos where we cannot perform direct experiments and thus have to rely on indirect sources such as cosmic rays. In order to precisely detect cosmic-rays, we need large area experiments with a large number of very sensitive detectors, which can account for both larger flux as well as energy distribution of the incoming cosmic rays. *ARGO-YBJ* experiment in Tibet [Sta08], *Pierre Auger Project* in Argentina [Man], *KASCADE-Grande* experiment in Germany [10b], *GRAPES-3* experiment in India [GUP14], are some of the ground-based large area experiments to study various properties of the cosmic rays.

Nuclear fusion process that power the Sun and other Stars, Radioactive decay (beta-decay), Nuclear reactors, Cosmic-rays, Supernova events and other such extra-galactic phenomena are some of the sources of neutrinos. The significance of studying various properties of neutrinos is quite evident from that the 2015 Nobel Prize in Physics was given for the discovery of *Neutrino Oscillation* which indeed was the first realization towards physics

beyond the regime of the Standard Model. Other such mysteries like neutrino mass hierarchy, the absolute scale of neutrino mass etc. need to be studied very precisely which may give us more insight into the physics beyond the Standard Model. Just like the muons, neutrinos also travel unimpeded and can penetrate to significant depths underground. Since neutrinos are weakly interacting because of their smaller interaction cross-section, they need to be detected using detectors deployed deep beneath the surface of the Earth to avoid background. Neutrino detection also needs larger detector volume and mass in order to get significant neutrino events. Neutrinos are not directly detected as they are very weakly interacting, which is why an absorber medium is used in which neutrinos undergo decay into charged particles and then, these charged particles are detected and traced back to study the properties of the corresponding neutrinos. *The Sudbury Neutrino Observatory (SNO)* in Canada [ED05], India Based Neutrino Observatory (INO)-ICAL experiment in India [Col17], *Super-Kamiokande* neutrino detection experiment in Japan [Wal08] etc. are some of the underground experiments using various detector technologies to study different properties of atmospheric neutrinos.

Other such exotic particles such as the Weakly Interacting Massive Particle (WIMP) which is a postulated dark matter candidate, is another area of interest for astroparticle physicists. The weak interaction of WIMP makes its detection an extraordinarily challenging task, requiring highly sensitive detectors with larger active volume and mass to maximize the observations. *Super Cryogenic Dark Matter Search (SuperCDMS)* experiment in Minnesota, United States [SC15, MAH12], *Large Underground Xenon (LUX)* experiment in US [10a] etc. are some of the experiments which are involved in the quest to unfold the mysteries of the dark matter.

As we have seen that in order to detect such exotic particles which indeed carry useful information which will help us to know more about this world and also to detect new fundamental particles such as the Higgs boson, we need highly sensitive detectors which can precisely give us information about the incoming particles, thereby unfolding many unsolved mysteries in physics. One category of such detectors is *Gaseous Ionization Detectors*, which are easy to manufacture and have found to be very useful for the precise measurement of various properties of the incoming charged particles which either come from accelerator sources or are measured directly (through their availability in the atmosphere). These detectors are elaborately explained in the following Chapter.

(a) GRAPE-3 experiment at Ooty(India), designed to study cosmic rays with air-shower detectors and large area muon detector (scintillator).

(b) ARGO-YBJ is a Chinese-Italian experiment located at Tibet, to observe very high energy gamma rays using an extensive air-shower array consisting of a carpet of RPCs.

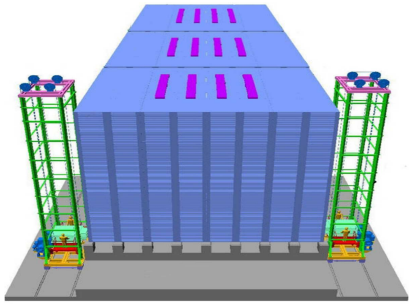

(c) INO ICAL detector being built in INDIA with the aim of detecting Neutrinos using an array of RPC detectors with iron sheets as absorbing medium.

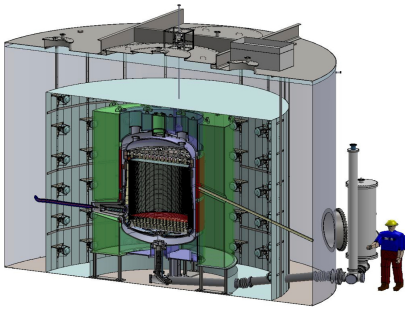

(d) LUX experiment located at Stanford, 1,480m underground, aimed at detecting dark matter using liquid Xenon time projection chamber.

Figure 1.7: Some Large Area experiments in Astroparticle Physics.

1.3 Motivation for the current work

As we have seen in section 1.2.2, that the future upgrade of Large Hadron Collider (LHC) at CERN aims to achieve a peak luminosity of 5×10^{34} particles $cm^{-2}\ s^{-1}$ during its next run in 2025 in order to increase the potential for discoveries. With this increased luminosity, particle rate will increase significantly and thus, highly sensitive detectors are required to cope up with such high particle rate. In order to have precise timing information, which is an important parameter in particle identification, of various particles hitting the detectors, the detector time resolution which is discussed in section 1.3.2 should be very good. Same goes for non-collider experiments such as in the case of cosmic-ray experiments, in which the cosmic-ray particles hitting the earth's atmosphere have varying angular and energy distribution and large flux. In order to get precise information about the energies and timing of the incoming cosmic-rays, again highly sensitive detectors with good time resolution are needed. Moreover, cosmic-ray experiments are spread over a larger area in order to account

for their large flux. Thus, a large number of detectors are needed to be deployed in such large areas. For this, the detector being used has to be economical so that it can be used in large numbers.

One such detector which has been identified to satisfy all these criteria for particle identification both for large area experiments and accelerator experiments is the Multigap Resistive Plate Chamber (MRPC) detector which is the variation of conventional Resistive Plate Chamber (RPC) detector. MRPC has a time resolution of less than 100 picoseconds, improved rate capability and is easy to manufacture which makes it a suitable candidate to be used in large area experiments as well as in other experiments involving large particle flux. Apart from particle identification, MRPC is also being used for medical applications such as in Positron Emission Tomography (PET) as well as in homeland security applications especially in Muon Tomography because of its improved time resolution. Hence, looking at future demands for larger and more sensitive experiments which are aiming to increase the potential for discovering more exotic physics results, research and development on Multigap Resistive Plate Chamber (MRPC) detector will be a useful endeavor towards bringing breakthroughs in detector technology. With this in mind, we have worked on the optimization of a five gap MRPC detector to get the best possible time resolution by varying various parameters. Addressing the questions such as why MRPC is preferred over conventional RPC and detail analysis and optimization of MRPC is provided in the following chapters.

Chapter 2

Gaseous Ionization Detectors

Gaseous ionization detectors are the radiation detectors used in particle physics to detect charged particles directly or indirectly (in which the charged particles are the decay products of particles which do not directly interact with matter as in the case of neutrinos). The earliest of the particle detectors consist of cloud chambers (built in 1911 by C.T.R. Wilson), bubble chambers (invented by Donald A. Glaser in 1952), spark chambers etc. which were not very efficient and had poor spatial and temporal resolution and were short-lived. Then, in the late 1960s, the development of the Multi-Wire Proportional Chamber and later the Drift Chamber, the Time Projection Chamber, and the Resistive Plate Chamber which are highly sensitive and efficient, helped to renew the interest in gaseous detectors and are now extensively used in various high-energy physics experiments. The detection of charged particles happens through their interaction with the detector mass, in which they lose their energy which then can be converted into a detectable signal.

2.0.1 Passage of Particles through Matter

When charged particles pass through the detector mass (matter), they lose energy and leave characteristic signatures which are produced through different mechanisms. Electrically charged particles lose energy mainly by *ionization or excitation*, as well as by other processes such as *bremsstrahlung*, *transition radiation* and *Cherenkov radiation*. Photons on the other hand interact with matter by processes such as *the Compton scattering*, *the photo-electric effect*, and *the pair production*. For brevity, we will mainly deal with the interaction of charged particles with the matter as this is what is needed to understand the working of gaseous detectors.

Interaction by Ionization and Excitation : When a charged particle passes through matter, it undergoes inelastic collisions with the atomic electrons and thus, due to Coulomb

multiple scattering, the charged particle loses energy. If a charged particle of mass m_0 and reduced velocity $\beta = \frac{v}{c}$ undergoes collision with an atomic electron with mass $m_e << m_0$ while traversing through some matter, then the maximum kinetic energy T_{max} transferred to the atomic electron is [Maj02],

$$T_{mas} = \frac{2m_e c^2 \beta^2 \gamma^2}{1 + 2\gamma \frac{m_e}{m_0} - \frac{m_e}{m_0}^2}$$

where, c = speed of light and $\gamma = \frac{1}{\sqrt{1-\beta^2}}$.

Having calculated the maximum energy transferred to an atomic electron, the mean energy loss per unit length or the stopping power of a fast-moving charged particle (excluding electrons and positrons) traversing through a medium is given by *Bethe-Bloch formula* as shown below,

$$-\langle \frac{dE}{dx} \rangle = KZ^2 \frac{Z}{A} \frac{1}{\beta^2} \Big[\frac{1}{2} ln\Big(\frac{2m_e c^2 \gamma^2 T_{max}}{I^2} \Big) - \beta^2 - \frac{C}{Z} - \frac{\delta}{2} \Big]$$

where,

$K = 4\pi N_A r_e^2 m_e c^2$;
N_A = Avogadro's number;
r_e = classical electron radius;
T_{max} = maximum kinetic energy transferred to electron;
m_e= mass of an electron;
I = mean excitation energy;
A = atomic mass of the medium;
Z = atomic number of the medium;
δ = density effect correction;
C = shell correction.

As can be inferred from the above formula that the energy loss is independent of the mass of the incoming particle. At lower energies (non-relativistic), the energy loss i.e., $\frac{dE}{dx} \propto \beta^{-2}$ and it decreasing with increasing the velocity till v = 0.96c, where a minimum is reached. In this case, all particles of the same charge have the same mean energy loss per unit length and are called as *minimim ionizing particles (MIPs)* [Maj02, Leo87]. Figure 2.1 shows the energy loss of positive muons due to ionization and excitation in copper versus the muon momentum (which depicts the muon energy).

Different regions of the plot in figure 2.1 are: (a) for $\beta\gamma < 3$, dE/dx $\propto \frac{1}{\beta^2}$; (b) for $\beta\gamma$ = 3.5, dE/dx = 1-1.7 MeV $cm^2\ g^{-1}$ (minimum); (c) for $\beta\gamma > 3.5$, there is a logarithmic rise and dE/dx $\approx$ 2 MeV $cm^2\ g^{-1}$; (d) for $\beta\gamma > 1000$, Bremsstrahlung process (electrons and positrons while passing through matter lose energy by radiating photons because of their deceleration in the Coulomb field of a nucleus, this process is known as bremsstrahlung) dominates. Each particle exhibits a unique dE/dx curve, for energies below the minimum

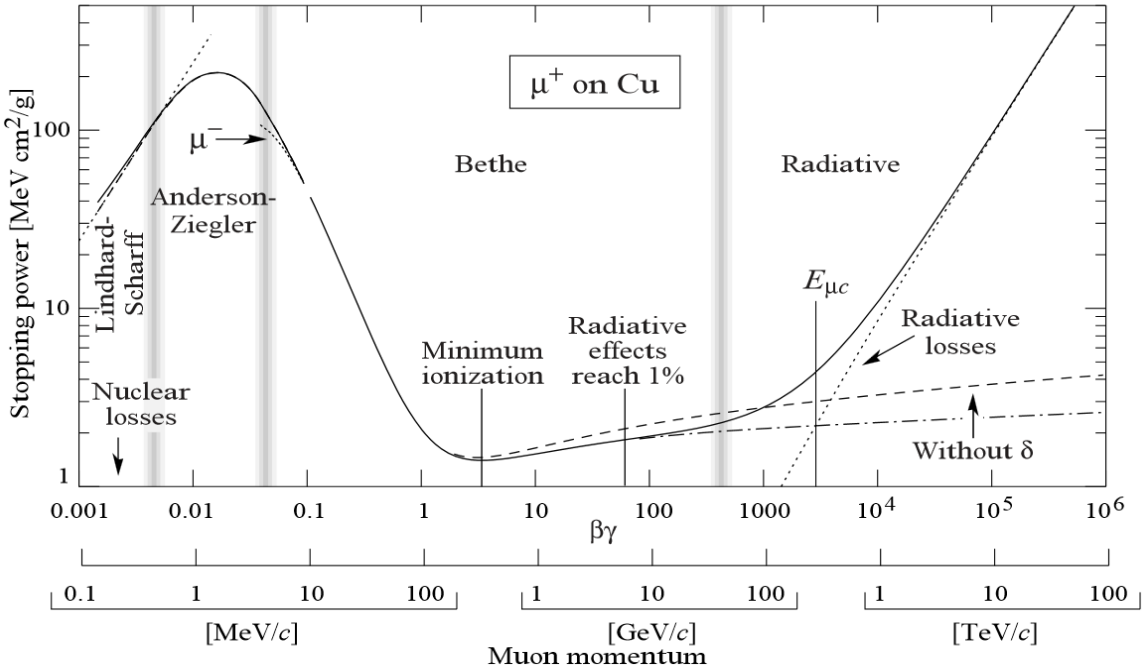

Figure 2.1: Stopping power (= $-\langle dE/dx \rangle$) for positive muons in copper as a function of $\beta\gamma$ = p/Mc over nine orders of magnitude in momentum (12 orders of magnitude in kinetic energy). The material density has here been factored out of the expression and divided out, giving the Y-axis units of MeV $cm^2\ g^{-1}$. Solid curves indicate the total stopping power. Particle Data Group (2012).

ionizing value and this characteristic is used to identify different particles in this energy range as shown in figure 2.2 [Leo87]. There will be fluctuations in the energy loss by the particles when repeated measurements are taken. For low-density material or thin layers, the energy loss distribution follows Landau distribution and high-density material or thicker layer, the energy loss distribution is more towards Gaussian distribution.

Interaction by Cherenkov Radiation: A charged particle moving in a dielectric medium with velocity greater than the phase velocity of light in that medium (β c = v > c/n, where 'n' is the index of refraction of the medium and 'c' is the velocity of light in vacuum), emits a characteristic radiation called as the *Cherenkov radiation*. When a charged particle traverses through a medium, due to its electric field it disrupts the local electromagnetic field of that medium causing electric polarization of the medium. If the particle travels fast enough such that the medium does not get time to get back to its mechanical equilibrium state after the disturbance caused by the particle, this energy which is contained due to disturbance is radiated as a coherent shockwave (just like a sonic boom of a supersonic aircraft) and the emitted radiation is the Cherenkov radiation. The contribution due to Cherenkov radiation to the total energy loss by a charged particle is very small.

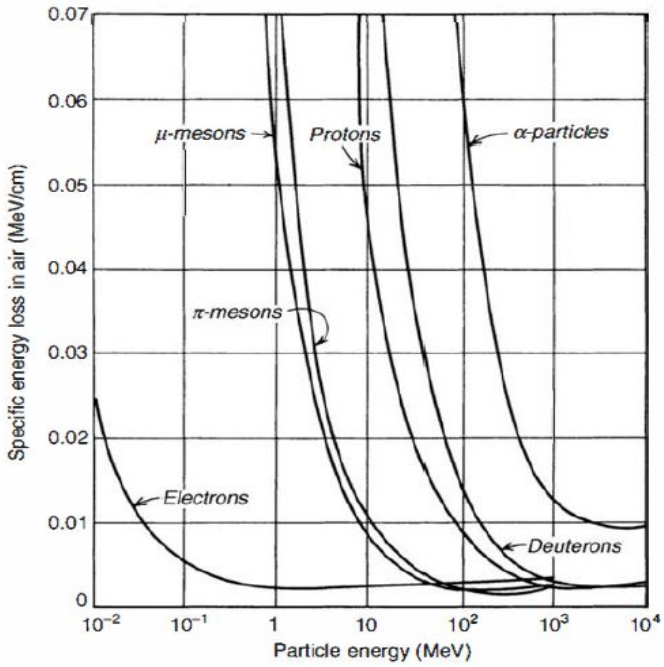

Figure 2.2: Variation of energy loss in air versus energy of different charged particles [Kno10].

Interaction by Transition Radiation: While crossing the boundary between two dielectric mediums with different dielectric constants, a charged particle emits a characteristic electromagnetic radiation called as *the transition radiation*. The emitted energy in the form of transition radiation is directly proportional to the Lorentz factor γ or in other words particles with larger γ results in more photons, hence transition radiation is very useful for identification of particles (especially in high momentum/energy range). Transition Radiation Detectors (TRDs) which are being used in many high energy physics experiments use this concept for particle identification.

2.0.2 General Characteristics of Detectors

As we have seen in the previous section that the charged particles traveling through detectors transfer radiation energy to the detector mass which then can be converted into a measurable signal which corresponds to different properties of the incoming particle. No particular detector can be used to study the properties of all charged particles. Depending upon the kind of particles need to be studied and various applications, particle detectors are designed. There are several characteristics specifying different features of the particle detectors which have to be considered before going into the specifics of the working of gaseous detectors.

Sensitivity: It is the capability of a detector to produce a measurable signal for a given

type of radiation or incoming particle. Detectors are designed in such a way that they are sensitive to certain radiations or incoming particles in some energy range. The sensitivity of a detector to a given type of radiation in certain energy range depends on the following factors [Leo87],

- the cross-section of the interaction of the incoming particle with the detector material
- the detector noise
- the detector mass
- the protective shielding around the active area of the detector

For example, to detect neutrinos which have smaller cross sections, we need detectors with larger detector volume and mass so that reasonable number of neutrino events are recorded.

Detector response: When a charged particle passes through a gaseous detector, the amount of ionization produced is proportional to the energy it loses in the active detector volume. Since, the output is obtained in the form of a current pulse whose time integral gives the total amount of charge produced in the detector, thereby indirectly providing information about the energy of the incoming particle. If this pulse does not change from one event to another, then the relation between the radiation energy or the energy of the incoming particle and the total charge or the pulse height of the signal obtained is referred to as the *response of the detector* . In many detectors, the response is linear over a certain energy range. In the case of charged particles with definite energies which are stopped inside the detector, the response is Gaussian because of the fluctuations in the energy loss due to ionization as discussed in the previous section.

Detector Efficiency: There are two types of efficiency when dealing with particle detectors. *The total or absolute efficiency* is defined as the fraction of events registered by the detector out of the total events emitted by the source and is the function of detector geometry and interaction probability in the detector.

$$\epsilon_{tot} = \frac{n_{registered}}{n_{emitted}}$$

Another one is called *the intrinsic efficiency* which is the fraction of events registered by the detector out of the events actually hitting the detector. Intrinsic efficiency is a function of the detector material, the type of incoming radiation and its energy.

$$\epsilon_{intrinsic} = \frac{n_{registered}}{n_{hitting}}$$

Energy Resolution: This is the extent to which a detector can distinguish between the closely separated energies of the incoming particles. Even for a monoenergetic particle, due

to fluctuations in the number of excitation and ionization produced in the detector volume, the resulting energy spectrum has a Gaussian-like peak. Thus, the energy resolution (ΔE) is given in terms of the *Full Width at Half Maximum (FWHM)*. For Gaussian distribution with standard deviation σ, FWHM = 2.355σ. Only when two peaks are separated by a distance greater than their FWHM, their energy is resolvable. The relative energy resolution at energy E is given by,

$$Resolution = \frac{\Delta E}{E}$$

The energy (of the incoming particle) dependence on the resolution of the detector is given by,

$$R = 2.355\sqrt{\frac{FWHM}{E}}$$

Response Time (Time Resolution) of the Detector: This is the time difference between the arrival of the charged particle or radiation and the formation of the signal by the detector. With good timing information, precise measurements can be made for the incoming charged particles. Time resolution can be improved by developing detectors in which signals are generated relatively faster and one such detector which gives time resolution in picoseconds is Multi-gap Resistive Plate Chamber which will be discussed exclusively in the following chapter.

Dead Time: This is the finite time required to process the signal by the detector after a charged particle passes through its active area. If another particle happens to pass through the detector during this time, no signal can be obtained for such particle and the information about such particles is potentially lost. During dead time, the detector basically remains insensitive to any radiation.

2.0.3 Basic Principle of Gaseous Ionization Detectors

The gaseous ionization detectors work on the basic principle of the collection of ionization electrons and ions at respective electrodes, which are produced when a charged particle ionizes the gas while traversing through the detector. *The ionization chamber*, *the proportional counter* and *the Geiger-Muller counter* were the earliest of the ionization detectors used for radiation detectors. There has been a substantial progress in the design of gaseous detectors to meet the challenges in high energy and astroparticle physics and are now being used extensively in big experiments for getting precise information about the incoming particles. For gas-filled detectors, a strong electric field is applied across the electrodes in order to draw the electrons and the ions produced in the ionization process towards the respective electrodes which then can be converted into a measurable signal. Depending on the electric

field strength, operation of gas-filled detectors can be divided into various regions as shown in figure 2.3.

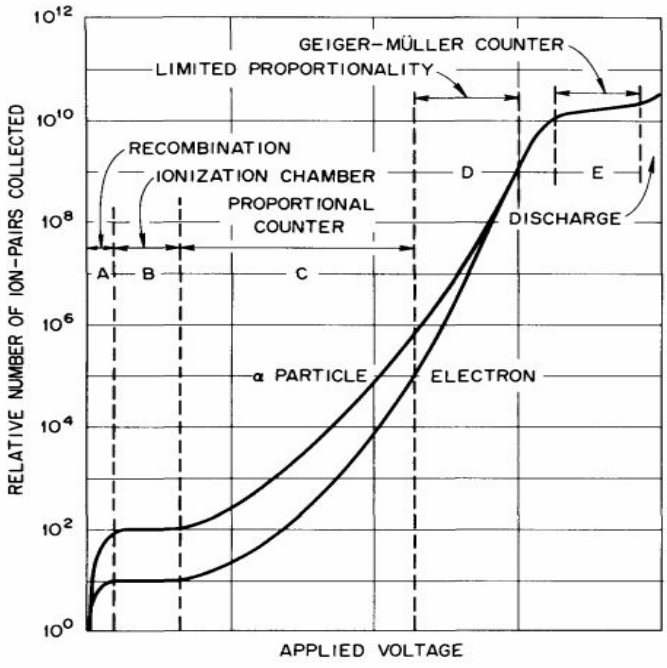

Figure 2.3: Number of ions collected versus applied voltage in a gas chamber showing the relationship between the ionization chamber, proportional counter, and Geiger-Muller counter regions of operation. Source: G.D.O'Kelley, Detection and Measurement of Nuclear Radiation.

When a charged particle passes through the active area of the detector, it ionizes the gas, thereby producing electrons and ions which then move to respective electrodes under the influence of external electric field. Different operating regions of a gaseous detector as shown in figure 2.3 are,

1. *The recombination region A:* If the voltage applied across the electrodes is zero, then the electron-ion pairs thus produced recombine under their own Coulomb interaction and no charge is collected at the electrodes.

2. *The ionization region B:* If some voltage is applied across the electrodes then more electron-ion pairs are collected before they can recombine. At some point, all the electron-ion pairs thus created will be collected at the electrodes and increase in the voltage thereafter will show no effect. Hence, the region B is called as ionization regions since the ionization electrons and ions produced by the charged particle are collected directly.

3. *The proportional region C:* If the voltage is increased beyond the region B, at this point the electric field is strong enough to accelerate the free electrons which then

further give rise to more such free electrons thereby causing secondary, tertiary etc. ionization i.e., the ionization cascade or avalanche. The number of electron-ion pairs in the avalanche is directly proportional to primary electron-ion pairs which is why it results in a proportional amplification of current and thus, this region is called as the proportional region.

4. *The region of limited proportionality D:* If the voltage is further increased, the number of ionization produced through multiplication goes beyond limit such that it results in the space charge effect. The electron-ion pairs produced inside the gas chamber drift towards respective electrodes and while drifting they usually attain a shape of liquid-drop, with the electrons forming the base and ions forming the tail of the charge distribution as shown in figure 2.6 (a). This distribution of electrons and ions distorts the local external electric field which results in the lost of proportionality and hence this region is called as the region of limited proportionality.

5. *The Geiger-Muller region E:* If we increase the voltage beyond the region D, it leads to a chain reaction of many avalanches over the entire region. The photons which are emitted by the de-exciting molecules travel to other regions in the chamber to further ionize the gas thereby causing secondary avalanches, which ultimately leads the breakdown of the detector. This process leads to the saturation of the output current which is then unaffected by the energy of the initial events, as can be inferred from the plateau (known as Geiger-Muller plateau) in figure 2.3. Quenching gas is used to absorb the photons and drain their energy in some other channel, in order to prevent the discharge. This voltage region is known as Geiger-Muller region (GM counter works primarily in this region). The width of the Geiger-Muller plateau depends upon the efficiency of the quencher. Further increasing the voltage leads to continuous breakdown (complete discharge) which can even damage the detector, hence this region should be avoided to prevent any such damage to the device.

Energy Loss Mechanisms in Gaseous Detectors: There are primarily three process through which a charged particle loses energy in a gas-filled detector and they are as follow,

- *Excitation:* A charged particle 'p' colliding with the atoms of the gas molecule (X) may cause excitation of the atom and this requires the correct amount of energy or resonant energy to cause excitation. The excited atoms or molecules may participate in further reactions to cause ionization.

$$X + p \longrightarrow X^* + p$$

- *Ionization:* In this process the incoming charged particle ionizes the gas releasing an electron-ion pair. This process has relatively higher energy threshold and since low energy transfers are more preferred, excitation reactions dominate in general [Leo87]. The process of the creation of electrons and ions by the incident radiation is called as *Primary Ionization*. These electrons thus produced may have sufficient energies (δ-electrons) to further ionize the gas thereby causing *secondary ionization* and so on.

$$X + p \longrightarrow X^+ + e^- + p$$

- *Penning effect:* In some atoms, excited metastable states created during the process of excitation (X^*) are unable to deexcite immediately by emitting photons. Such atoms undergo deexcitation when they collide with other atoms (Y) and result in the ionization the later (Y). This is known as Penning effect.

$$X^* + Y \longrightarrow X + Y^+ + e^-$$

- *Molecular-ion formation:* In this process a positively charged ion (X^+) collides with the neutral atom of the same type (X) and produces a molecular ion and an electron.

$$X^+ + X \longrightarrow X_2^+ + e^-$$

- *Auger effect:* When an electron is knocked out of the innermost shell of an atom during ionization, an electron from the higher shell jumps into its place and emit a photon which further can knock out an electron from the outer shell and this electron is known as an *Auger electron*.

- *Electron-attachment:* In this process the free electrons are captured by electronegative atoms.

$$X + e^- \longrightarrow X^- + h\nu$$

An important point worth noting is that empirical observations have shown that the average energy lost by the incident particle per electron-ion pair formed (W-value) is a constant parameter for different types of radiations and gases which is equal to approximately 30 eV. That means if a particle with energy 3 KeV is incident and is stopped within the gas, it will produce on an average 100 (3000/30) electron-ion pairs. Figure 2.4 shows different gas properties such as 'ρ' which is the gas density, 'I_0' is the first ionization potential, 'W_i' is the mean energy lost by an incident particle per electron-ion pair formed, 'dE/dx' is the energy lost per unit length and 'n_t' is the total number of electron-ion pairs produced per path length for a MIP. Processes such as recombination ($A^+ + e^- \longrightarrow A + \gamma$) and electron attachment ($A + e^- \longrightarrow A^- + \gamma$) reduces the primary electrons thereby affecting the efficiency

of the detector, hence it is recommended to minimize the use of electronegative gases which causes electron capture.

Gas	ρ (g/cm^3) (STP)	I_o (eV)	W_i (eV)	dE/dx (MeVg^{-1}cm^2)	n_t (cm^{-1})
H_2	$8.38 \cdot 10^{-5}$	15.4	37	4.03	9.2
He	$1.66 \cdot 10^{-4}$	24.6	41	1.94	7.8
N_2	$1.17 \cdot 10^{-3}$	15.5	35	1.68	56
Ne	$8.39 \cdot 10^{-4}$	21.6	36	1.68	39
Ar	$1.66 \cdot 10^{-3}$	15.8	26	1.47	94
Kr	$3.49 \cdot 10^{-3}$	14.0	24	1.32	192
Xe	$5.49 \cdot 10^{-3}$	12.1	22	1.23	307
CO_2	$1.86 \cdot 10^{-3}$	13.7	33	1.62	91
CH_4	$6.70 \cdot 10^{-4}$	13.1	28	2.21	53
C_4H_{10}	$2.42 \cdot 10^{-3}$	10.8	23	1.86	195

Figure 2.4: Important Gas Parameters. Source: K. Kleinknecht, Detektoren fur Teilchenstrahlung, B.G. Teubner, 1992.

Transport Properties of Electrons and Ions in Gases: In order to understand various characteristics of gaseous detectors it is indeed important to understand the motion of the electrons and the ions. The transport properties such as diffusion, drift velocity, avalanche growth etc. are briefly discussed which will further help us to understand the working of gaseous detectors.

- *Diffusion:* When the external electric field is switched off, the electrons and the ions created by the passage of a charged particle, move away from the point of their creation uniformly and this movement is known as *diffusion*. These electrons and ions undergo multiple scattering with the gas molecules during their free movement until they reach thermal equilibrium with the gas (which is at temperature 'T' and pressure 'P') and finally recombine. The mean diffusion velocity of these charges is given by Maxwell Distribution as follows,

$$v_{diff} = \sqrt{\frac{8KT}{\pi m}}$$

where, 'm' is the mass of electron or ion and 'K' is the Boltzmann constant. At room temperature, the speed of an electron is about 10^6 cm/s and that of an ion is about 10^4 cm/s. The distribution of charges after diffusing for time 't' follows Gaussian

statistics as,

$$\frac{dN}{dx} = \frac{N_0}{\sqrt{4\pi Dt}} exp\Big(-\frac{x^2}{4Dt}\Big)$$

where,

N = number of free charged carriers after time 't';

N_0 = initial number of charge carriers;

D = diffusion coefficient;

x = distance from the point of creation of the charged carriers.

The width of the distribution (i.e., spread in x) in one dimension is given by,

$$\sigma_x = \sqrt{2Dt}$$

and the width in three dimension is,

$$\sigma_r = \sqrt{6Dt}$$

where, r is the radial distance. The diffusion coefficient (D) can be found by using the mean free path γ of the electrons and the ions in the gas (which comes from the kinetic theory) as,

$$D = \frac{1}{3} v_{diff} \gamma$$

and since for a classical ideal gas we have the expression for the mean free path as,

$$\gamma = \frac{1}{\sqrt{2}} \frac{KT}{\sigma P}$$

where σ is the total cross section for collision with the gas molecule. Substituting the value of γ in the expression for D, we get the diffusion coefficient as follow,

$$D = \frac{2}{3\sqrt{\pi}} \frac{1}{\sigma P} \sqrt{\frac{(KT)^3}{m}}$$

The magnitude of charge diffusion coefficients under an external electric field along the field direction is called as *longitudinal diffusion coefficient* and that perpendicular to the field direction is called as *transverse diffusion coefficient*

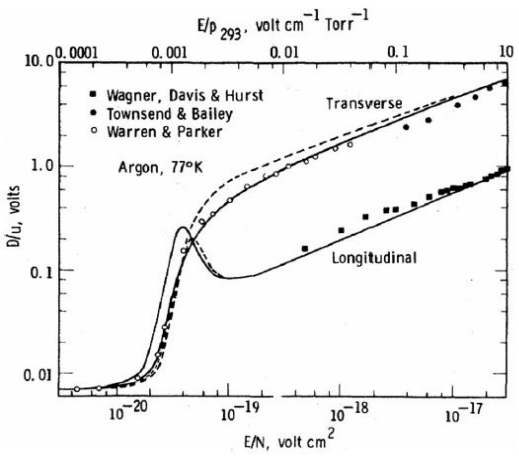

(a) Longitudinal and transverse diffusion in argon (Lowke and Parker, 1969 [LP69]).

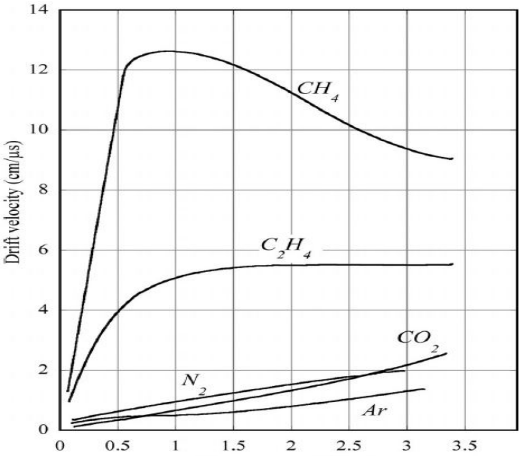

(b) Electron drift velocity as a function of field in pure gases at NTP (Sauli, 1977 [Sau77]).

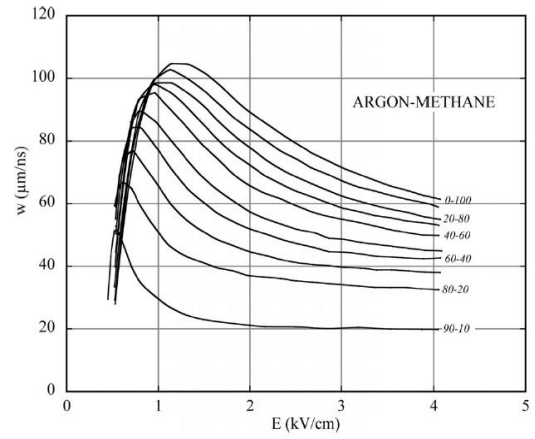

(c) Electron drift velocity in argon–methane mixtures at NTP (Jean-Marie et al., 1979 [79a]).

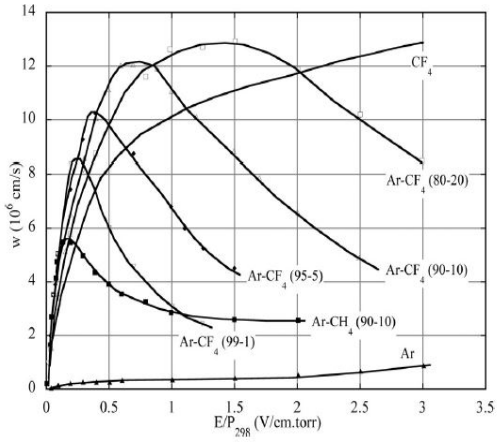

(d) Electron drift velocity as a function of field in CF4, pure and in mixtures with argon (Christophorou et al., 1979 [79b]).

Figure 2.5: Diffusion coefficients and drift velocity of electron for different gases.

- *Drift Velocity:* If the external electric field is switched on, the electrons and the ions are accelerated towards the respective electrodes under the influence of this external field and move along the field lines with some velocity which is known as *the drift velocity*. The acceleration of the charge carriers is interrupted by collision with gas molecules which limits the drift velocity. The mean drift velocity (v_d) is given by,

$$\vec{v_d} = \tau(\vec{E}, \sigma) \cdot \frac{q}{m} \cdot \vec{E} \cdot \frac{p_0}{p} = \mu \cdot \vec{E} \cdot \frac{p_0}{p}$$

where,

q,m = charge and mass of the charge carrier;

τ = mean time between the collisions;

E = external electric field;

p = pressure of the gas;

p_0 = standard pressure;

μ = mobility of the charge carrier and $\mu = \frac{eD}{KT}$ (Einstein Relation), D is diffusion coefficient. Figure 2.5 shows the diffusion coefficients and drift velocity for an electron in different gases.

- *Avalanche Multiplication:* Electrons produced in the primary ionization gain enough energy due to the external electric field to further ionize the gas i.e., to cause secondary ionization which then further results in tertiary ionization and so on. This process leads to avalanche formation in the gas chamber. Due to high electron mobility, the avalanche has liquid-drop shape with the electrons forming head and ions forming the tail of the avalanche as shown in figure 2.6 (a).

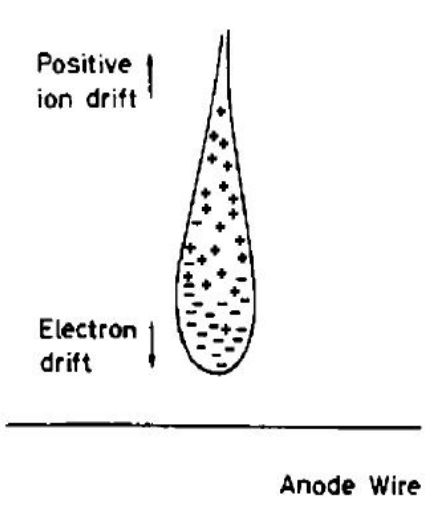

(a) Avalanche formation in gaseous detectors.

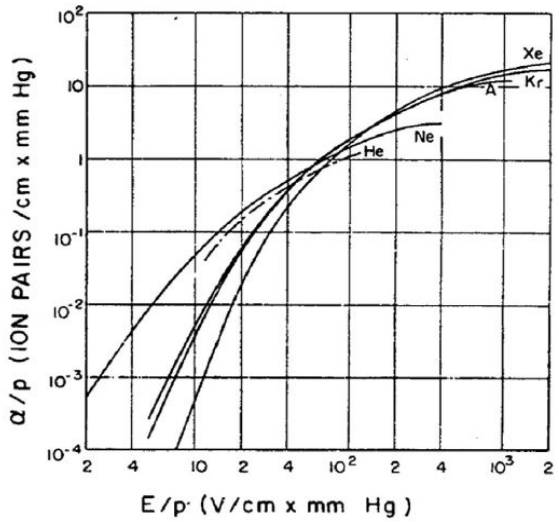

(b) First Townsend coefficient as a function of field for the different gases (Druyvesteyn and Penning, 1940)

Figure 2.6: Avalanche formation and first Townsend coefficient for different gases.

An average distance an electron travels before encountering an ionizing collision is known as the mean free path (λ). Inverse of the mean free path, i.e., $\lambda^{-1} = \alpha$, which is known as *first Townsend coefficient* and it represents the number of electron-ion pairs produced per unit path length. From α we can find the total number of electrons created after the avalanche has progressed though a distance 'x', which is given by,

$$N = N_0 e^{\alpha x}$$

where, N_0 = original number of electrons. The multiplication factor $M = N/N_0 = e^{\alpha x}$ and for the case of non-uniform electric field in which the first Townsend coefficient

(α) depends on 'x', the multiplication factor is given by,

$$M = e^{\int_{x_1}^{x_2} \alpha(x) dx}$$

If the multiplication factor goes beyond 10^8 or $\alpha x > 20$, it leads to the breakdown of the detector i.e., the detector enters streamer mode with uncontrolled avalanches eventually resulting in the complete discharge. This limit is known as *Raether limit*.

With this brief explanation on the working principle of gaseous ionization detectors, we can now understand the basics of different gaseous detectors such as the Multiwire Proportional Chamber (MWPC), the Drift Chambers, the Micropattern Detectors, the Resistive Plate Chambers (RPCs), the Gas Electron Multiplier (GEM) etc. which differ in their geometries with the basic working principle being almost the same. In this work, we will deal with a variation of the conventional Resistive Plate Chamber (RPC) i.e., we will analyze in detail the working principle, signal collection, applications of the Multigap RPC which is being used extensively in various high energy and astroparticle physics experiments. We will use simulation tools to improve some characteristics of this detector by changing various parameters.

Chapter 3

Multigap Resistive Plate Chamber (MRPC) Detector

3.1 Introduction

3.1.1 Resistive Plate Chamber (RPC) Detector

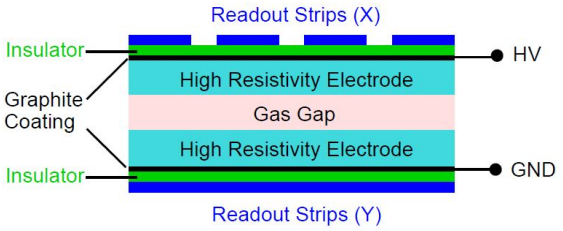

Figure 3.1: Schematic of Resistive Plate Chamber (RPC) [SC81].

Before diving into the details of Multigap Resistive Plate Chamber (MRPC), let us understand the conventional Resistive Plate Chamber (RPC) first and then we will analyze why MRPC is preferred over RPC. The Resistive Plate Chamber (RPC) is a gaseous parallel plate avalanche detector consisting of two parallel plate electrodes with high volume resistivity between 10^9 to 10^{10} Ω cm, separated by a narrow gas-gap containing an ionization gas mixture as shown in figure 3.1. The RPC was developed by R. Santonico and R. Cardarelli in 1981 [SC81]. With the gas-gap of few mm thick, RPCs can achieve the time resolution in few nanoseconds and much-improved detector efficiency. When a charged particle passes through RPC, it ionizes the gas thereby producing the ionization electrons and ions. These electrons under the influence of an external electric field (which is the result of the high voltage applied to the graphite coating with surface resistivity around 200-300 KΩ/square on the outer surface of the resistive electrodes) further ionizes the gas leading to secondary ionization and resulting electrons again ionizes the gas causing the avalanche of charged carriers which travel towards respective electrodes and due to the movement of charged carriers (especially electrons), current is induced in the outer electrodes. There are two operational modes of an RPC - *avalanche*

mode and *streamer mode* which are described as,

Avalanche mode: In avalanche mode, when the incoming charged particle ionizes the gas, the electrons thus produced, result in more electrons through ionization. The charge carriers grow exponentially corresponding to Townsend avalanche. When the gas gain is large, space charge effect (reduction in the local electric field due to the field developed by a liquid-shaped distribution of charge carriers during the avalanche growth) comes into picture which hinders the multiplication process, thereby preventing the avalanche to grow further. Avalanche mode allows the RPC to operate at larger particle rate up to a few KHz/cm^2. For this, the streamer mode must be prevented, which is usually done by adding small amounts of an electronegative gas such as SF_6 which absorbs extra photons preventing the streamer mode. The development of an avalanche is an RPC is shown in figure 3.2.

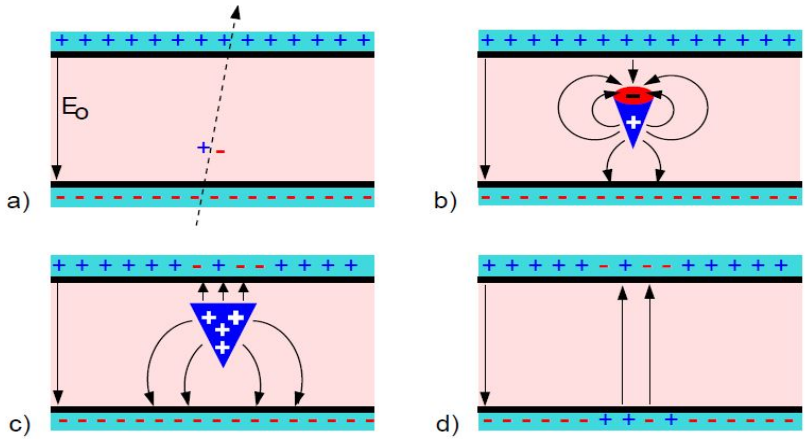

Figure 3.2: Development of an Avalanche in RPC. E_0 is the external electric field. a) A charged particle ionizes the gas, b) Space charge effect comes into picture due to large avalanche size, c) the electrons reaches the anode while the ions drift slowly, d) Charges at the resistive electrodes disturbs the field in the small region where an avalanche is developed.

Streamer mode: Figure 3.3 shows the development of a streamer in the RPC. During the multiplication process of the charge carriers, if the gas gain is increased further than that in the case of avalanche mode, in this case even photons contribute to the avalanche and thus, the avalanche grows in an uncontrolled fashion leading to local discharge (streamer) in the gas gap. A spark may be created during this process. [vCLaK]. In streamer mode, the output current pulse is relatively large, but the rate capability is only few 100 Hz/cm^2 as shown in figure 3.3. As can be seen from the following figure that in the streamer mode the maximum flux for efficiently detecting the minimum ionizing particle is reduced by several orders of magnitude.

The use of highly resistive electrodes in (M)RPC helps the localization of discharge in

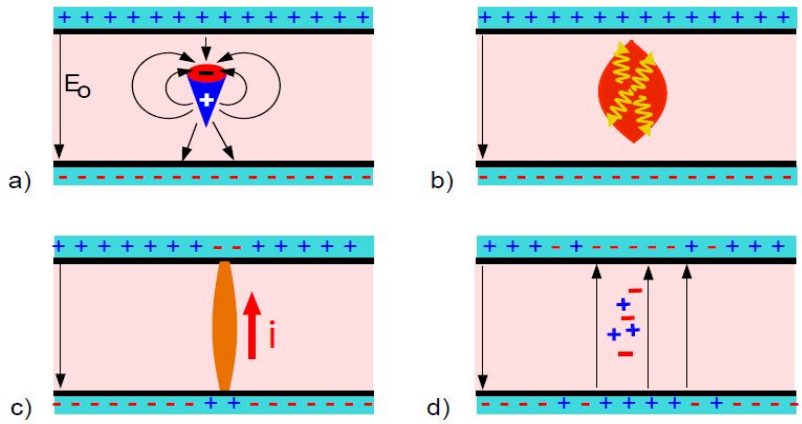

Figure 3.3: Development of a Streamer in RPC. E_0 is the external electric field. a) Avalanche formation, b) Photons contribute to the avalanche growth resulting in a streamer, c) Weak spark creation, d) Strong decrease in electric field around the spot of the avalanche.

the gas-gap (presence of an electronegative gas which absorbs photons and prevents the streamer mode also helps the localization). If a charge Q_0 enters the surface of a resistive electrode, it decomposes with time 't' as follows,

$$Q(t) = Q_0 e^{-\frac{t}{\tau}}$$

with

$$\tau = \rho \epsilon_0 \epsilon_r$$

where, ϵ_0 and ϵ_r are the dielectric constant and relative permittivity of the resistive electrode and ρ is the volume resistivity of the material of which the electrode is made up of. τ is known as *the relaxation time* (time for the redistribution of charges on the surface of the electrodes) [vCLaK]. The charges accumulated on the surface of the resistive electrodes due to ionization in the gas-gap results in an electric field in the opposite direction to that of applied field thereby reducing the effective electric field locally around the initial avalanche as shown in figures 3.2 and 3.3. During this time, the spot where the local electric field is disturbed becomes potentially dead (it cannot respond to more charge collection due to incoming radiation) for a time which is equal to the relaxation time τ. Hence, in RPCs the relaxation time τ can be referred to as the dead time of the detector. This reduction in the local electric field is sensed using capacitors and this is how the signal is obtained in RPCs. Note that the relaxation time τ is proportional to the volume resistivity ρ, that means with increasing the volume resistivity of the electrodes, the relaxation time (or the dead time) of an RPC will increase, thereby decreasing the efficiency of the detector (if a detector is dead for a long time, its efficiency effectively decreases). Then why do we use highly resistive electrodes for (M)RPC? Another point to note is that increasing the volume resistivity reduces the spread of charges on the surface of the electrodes thereby narrowing the width of

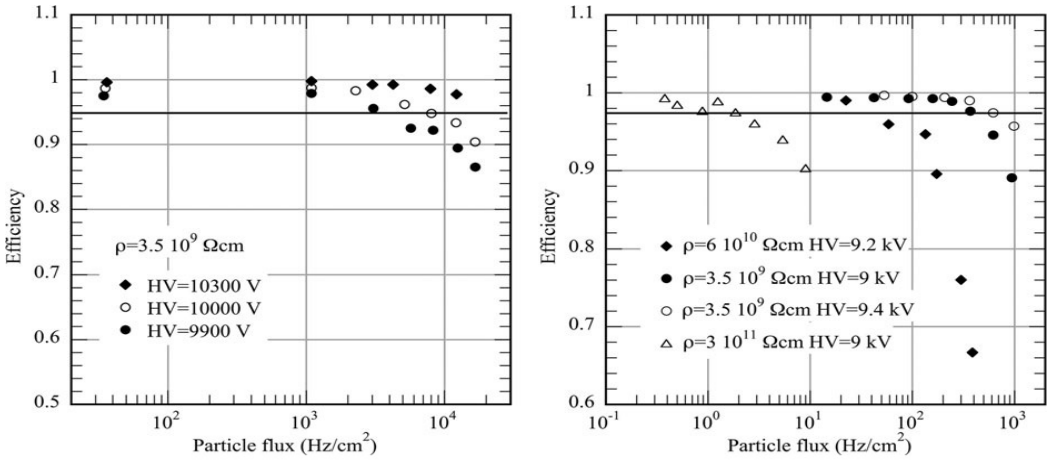

Figure 3.4: Efficiency of an RPC as a function of particle flux and voltage in the avalanche (left) and streamer modes (right) for several values of bulk resistivity (Arnaldi et al., 1999 [99]).

the discharge in the gas-gap, which can be used to obtain the spatial resolution of the incoming particles more precisely. The resistive electrodes serve a two-fold purpose in RPCs, one is to reduce the maximum current so that streamers do not develop into sparks and second is to reduce the variations in gas gain due to unavoidable changes in the dimension of gas-gap. Hence, it is important to optimize the volume resistivity of the electrodes to be used in (M)RPC so that we can reduce the width of the local discharge without any cost to the efficiency of the detector. The resistive electrodes are usually made up of bakelite (which has a volume resistivity of around 10^9 Ω cm) or glass (having volume resistivity of around 10^{11}-10^{12} Ω cm). The volume resistivity of an RPC determines the rate capability, whereas the width of the gas-gap determines its time resolution. The conventional 2 mm gas-gap RPC operated in avalanche mode has time resolution in few nanoseconds and rate capability of few KHz/cm^2. Since, RPCs are easy to manufacture and have fairly good time resolution, they are being used in large numbers as muon detectors in experiments such as *BaBar at SLAC [Fer09]*, *CMS [09a]*, *ALICE and ATLAS at CERN [09b, Bin12]*, *ARGO-YBJ in Tibet [Cam09]* etc.

3.1.2 Shortcomings of the RPC detectors

In spite of RPCs being used in large numbers in various high energy and astroparticle physics experiments, they pose a lot of challenges such as long-term operational stability, aging effects due to HF production, increase in dark current with time, degradation in efficiency with time due to large streamers in 2 mm gap RPCs, temperature effects, dead channels, gas leaks, low rate capability and time resolution for future upgrades, connectors,

electronics [VP12] etc. The conventional 2 mm gas-gap RPCs if operated in avalanche mode, have the time resolution of few nanoseconds and rate capability of few KHz/cm^2 which indeed is not enough for particle identification in the case of high particle rate which is expected from proton-proton collisions in LHC at CERN as described in section 1.2.2. Time resolution in sub-picoseconds range (better than 100 ps) and the rate capability of the order of 10 KHz/cm^2 is required to cope up with the large particle rate as part of the future high-luminosity upgrade of Large Hadron Collider at CERN as well as for getting precise energy and temporal resolution in some astroparticle physics experiments.

Since the avalanche is generated across the gas-gap by the multiplicative gain-gain ($N = N_0 e^{\alpha x}$, where N_0 is the number of initial electrons generated in the primary cluster), the electron which traverses the entire gas-gap results in the largest gain. If an electron is produced at a distance 'x' from the anode, then it has a gain of $G^{x/D}$, where 'D' is the gas gap and 'G' is the gain of an electron traversing the whole gas-gap [IA95]. In an avalanche, if the number of electrons exceeds $\sim 10^8$, then transition to streamer mode occurs which is why in RPCs the high voltage is chosen such that the maximum gain does not increase above 10^8. RPCs also suffer from rate effects because the increase in gas gain results in the space charge in the gas-gap which limits the avalanches thereby affecting the output pulse. The fluctuations in the formation of the ionization clusters in the conventional 2 mm gas-gap RPC limits its intrinsic time resolution to few nanoseconds. These fluctuations also result in time jitters in the output signal. In 2 mm gas-gap RPCs, the gas gain varies rapidly with the applied voltage as shown in figure 3.5.

One way to deal with these challenges is to decrease the gas-gap of RPCs or use a multi-gap design with narrow gas-gaps. The following sections exclusively deal with the Multigap Resistive Plate Chamber (MRPC) detectors which have been found to have improved time resolution and efficiency besides retaining other qualities of the conventional RPCs.

3.2 The Operating Principle of MRPC

Multigap Resistive Plate Chambers (MRPCs) are gaseous ionization detectors consisting of multiple equally-spaced gas-gaps made up of highly resistive electrodes which are separated by insulating spacers. MRPC is a modification of the conventional RPC which is discussed in the previous section.

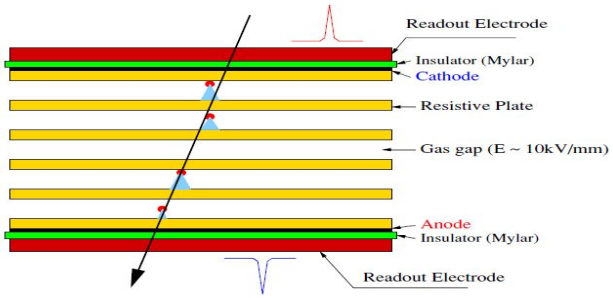

Figure 3.6: Schematic of Multigap Resistive Plate Chamber (MRPC).

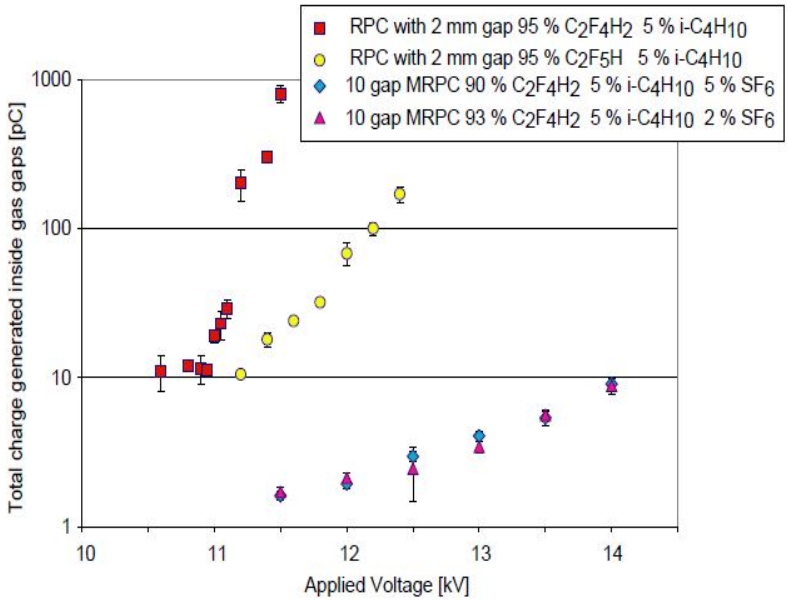

Figure 3.5: Charge produced in the gas gaps versus applied voltage. The voltage is applied across the single gap for 2 mm gas-gap RPC and for MRPC, the data were obtained using a double stack device with 10 gaps of 250 mm: The voltage shown is the voltage applied across 5 gas gaps [Wil04].

The first Multigap Resistive Plate Chamber was originally designed in 1996 to get improved time resolution in orders of picoseconds besides retaining other qualities of the wide gap RPCs such as the fairly good rate behavior and ease of manufacturing [ECZ96]. It was later found that MRPCs have better rate capability and longer efficiency plateau (the detector works efficiently even for larger values of applied voltage across the electrodes). In order to better understand as to why MRPCs work so well, let us first explore the basic working principle of MRPCs.

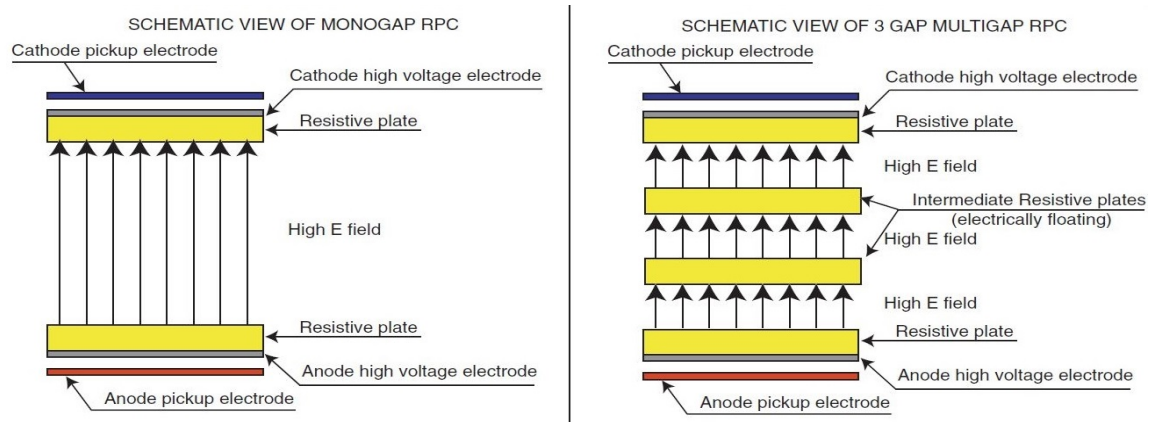

Figure 3.7: Schematic representation of single-gap and multigap RPC.

3.2.1 Basic Geometry and Advantages of Floating Electrodes in MRPC

Multigap Resistive Plate Chamber (MRPC) as shown in figure 3.6 consists of a stack of equally-spaced resistive electrodes (having a volume resistivity of 10^{10} - 10^{12} Ω cm) which create a series of gas-gaps. The outer layer of the outermost resistive plate is coated with a conductive graphite layer to which high voltage is applied in order to create a uniform electric field in the gas gaps. Then, above the graphite coating, we have an insulating Mylar layer above which pick-up strips are placed to sense the induced current due to the movement of charges in the gas-gaps. Intermediate resistive electrodes (a, b, c, d as shown in figure 3.8) are electrically floating i.e., no direct voltage source is applied to these electrodes, thus they acquire the voltage using the principles of electrostatics as shown in figure 3.8. All the electrodes are separated using spacers having a volume resistivity of around 10^{13} Ω cm. The advantage of the floating electrodes is that the voltage which they assume due to electrostatics is self-regulating (i.e., they are maintained at correct voltage due to the flow of electrons and ions in the avalanches) and provide same electric field in all the gas-gaps which results in the simultaneous occurrence of avalanches in all sub-gaps and thus the induced signal is the sum of all the gaps. Let us analyze this mechanism in detail.

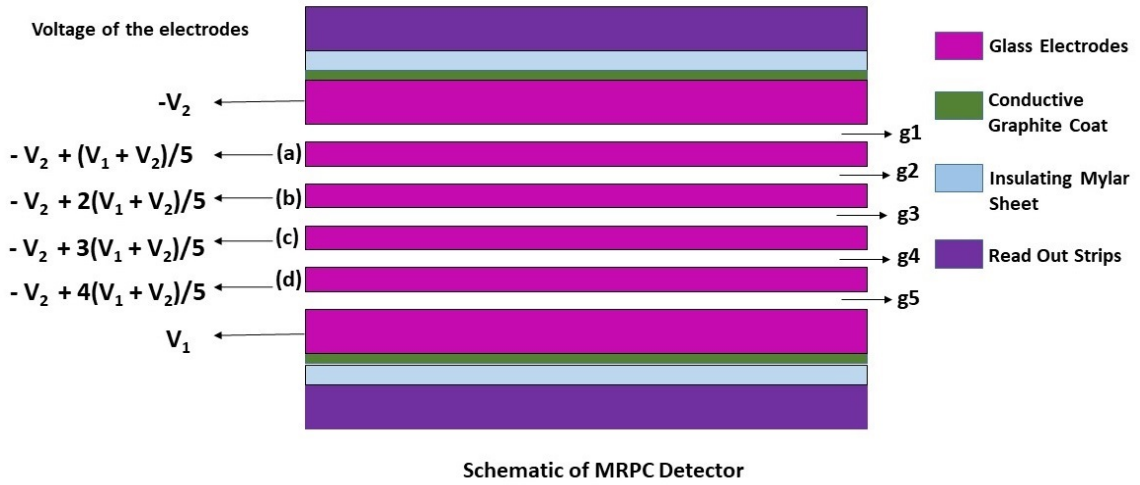

Figure 3.8: Voltage on the floating resistive electrodes (a,b,c and d) in MRPC with gas-gaps (g1, g2, g3, g4, g5).

When a charged particle passes through MRPC, under the influence of the strong electric field, ionization electrons and ions undergo multiplication and results in an avalanche just like in the case of RPC. Since all the sub-gaps are of uniform dimension, the electric field is same in all the gaps and thus, the rate of the avalanche in each sub-gap is approximately same. Into each intermediate resistive electrode the flow of electrons from one side is equal to the flow of ions from the other side, thus the net charge flowing into each electrode is

zero. Let us imagine that the voltage applied to the conductive graphite sheet is $V_1 = V_2 =$ 6000 V. In this case, the electric field (E = ΔV/d, where d is the gas-gap) in each sub-gap is 12 KV/mm assuming each gas-gap to be 200 microns. Then, as per the voltage division, as shown in the above figure, the voltage that each electrode (a, b, c and d) assumes is -3600 V, -1200 V, 1200 V, 3600 V respectively. If due to some reason the voltage on the electrode 'b' becomes -1000 V instead of -1200 V, then the electric field in the gas-gap 'g2' increases thereby increasing the gain and the electric field decreases in the gap 'g3' thereby decreasing the gain. Thus, into the electrode 'b', there is an increase in flow of positive ions from gas-gap 'g2' (which has more gain) and decrease in the flow of electrons from the gap 'g3' (which has lesser gain) and this exchange brings back the electrode 'b' back to the potential -1200 V and this is how the voltage on the floating electrodes is self-adjusting, resulting in the same electric field in each sub-gap. As mentioned earlier, the consequence of this process is that the avalanche growth is almost same in every gap and the output induced signal is indeed the sum of all the gas-gaps. In MRPC, the intermediate electrodes also act as physical barriers to the avalanche growth, which allows the operation of the detector at a higher electric field in the avalanche mode which is restricted in the case of RPCs. Thus, being able to use higher voltages is advantageous for better time resolution and rate capability. With increasing the number of floating electrodes, the operating voltage also increases.

3.2.2 Advantages of Narrow Sub-gaps in MRPC

As mentioned earlier that an electron has a gain of $G^{x/D}$, if it is produced at a distance 'x' from the anode with 'D' as the gas-gap and 'G' being the gain of an electron traversing the whole gas-gap. According to this, for the single-gap RPC, detectable avalanches will be produced by an electron generated within hundreds of microns close to the cathode (with an increase in 'x', the gain increases). The time jitters in the signal for RPCs is caused by the drift speed of an electron which has to travel a relatively longer distance [ECZ96]. Same goes for the multigap RPC in which also an electron has to be generated near the (sub)-cathode in each gas-gap to produce a detectable avalanche. The advantage of narrow sub-gaps is that the electrons have to travel lesser distance which effectively reduces the fluctuations in their drift-speed, thereby reducing the time jitters in the case of MRPC. Another merit of MRPC is that the avalanche generated in any one of the sub-gaps can be induced and used to get information about the incoming particle. As electrons have to travel lesser distance in these narrow gaps, this results in a faster signal on the outer electrodes, which is the reason for an improved time resolution in MRPC.

The time resolution of single gap RPC is given by [WR03],

$$\sigma_t = \frac{1.28}{(\alpha - \eta)\, v}$$

and for multigap RPC, the time resolution is given by [DGD16],

$$\sigma_t = \frac{1}{\sqrt{N}} \sqrt{\frac{\lambda_0}{g}} \frac{M}{(\alpha - \eta)\, v_d}$$

where, N is the number and g is the thickness of the gas-gaps, λ_0 is the mean free path of the incoming particle before it undergoes ionization, M is a factor (of order 1) that accounts for the avalanche statistics as well as for the fact that not all primary ionization contribute equally, $\alpha_{eff} = (\alpha - \eta)$ is the effective Townsend coefficient with α as the Townsend coefficient, η as the attachment coefficient and v as the drift velocity of the electrons. If an electronegative gas is used in the MRPC, then there is a probability that an electron drifting through the gas under the influence of an external electric field may be captured by a gas molecule thus forming a negative ion (electron-attachment). This probability is defined as the *attachment coefficient* η. Figure 3.9 shows the Townsend and attachment coefficient as calculated using Imonte [Biaa] for 4-gap RPC with 300 microns gas-gap which has electric field of around 100 KV/cm resulting in the Townsend coefficient of around 113/mm and single gap RPC with 2 mm gas-gap having electric filed of around 50 KV/cm which results in the Townsend coefficient of around 10/mm[WR03]. Apparently for narrower gas-gaps, due to an increased electric field, the Townsend coefficient and the drift velocity of electrons are relatively more as shown in figure 3.9, thus even analytically we can see that for small gas-gaps, there is an improvement in the time resolution. Due to the process of electron-attachment, the number of positive ions equals the number of negative ions generated plus the number of free electrons, but the fast signal is still due to the movement of the electrons. Thus, by incorporating electron attachment, the ratio of fast signal to total signal becomes $1/(\alpha_{eff} + \eta)$.

Another important consequence of narrow sub-gaps in MRPC is the improved space charge effect. With narrower gas-gaps having the high electric field, the charge density substantially increases which causes strong space charge effects in MRPC. In the case of MRPC, space charge effect indeed has an advantage as it limits the growth of avalanches in gas-gaps thereby preventing the streamer mode and this in-turn helps in less rapid variation in gas-gain with the applied voltage i.e., resulting in longer streamer-free efficiency plateau as shown in figure 3.10. Strong space charge effect in MRPCs also results in the recombination of negative ions (formed due to electron attachment) with the positive ions formed during ionization, thereby enhancing the ratio of fast signal to the total signal even after using an electronegative gas (which is also used as an electron quencher to prevent streamer mode) [04].

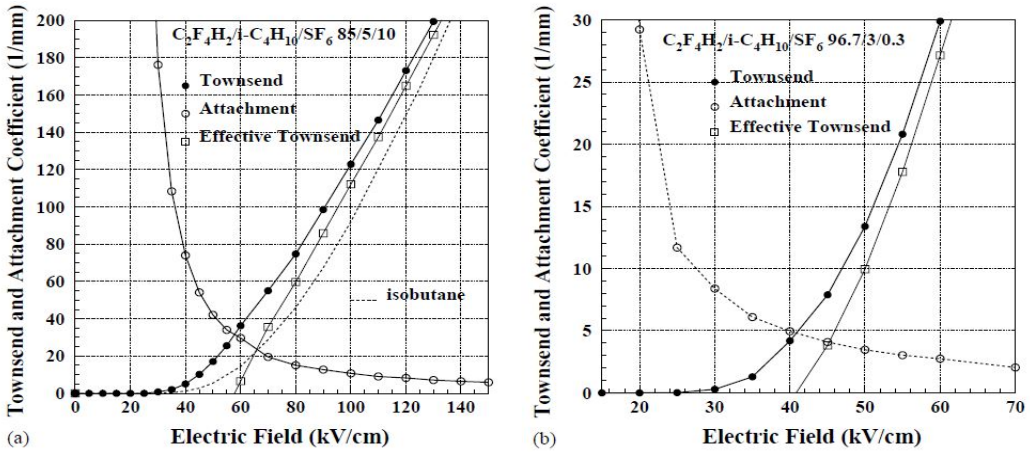

Figure 3.9: Townsend and attachment coefficient as calculated by Imonte for the 4-gap RPC with 300 mirons gas-gap (a) and single gap RPC with 2 mm gas-gap (b) gas [WR03].

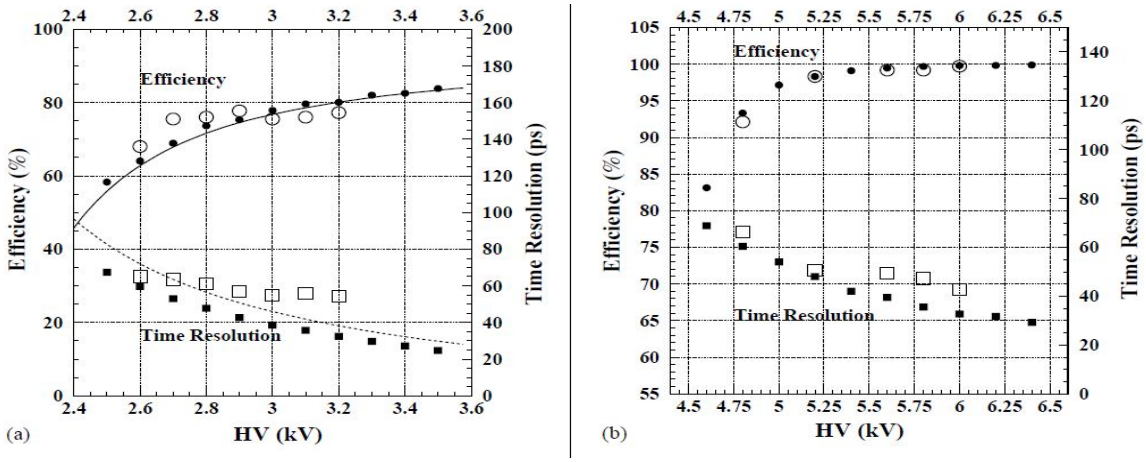

Figure 3.10: Efficiency and time resolution for single gap (a) and 4-gap (b) RPC. The open symbols are measurements and filled symbols are from simulation [WR03].

In MRPC, the electrodes act as dielectrics and are transparent to fast signals which are generated by avalanches in the gas-gaps. These fast signals are produced only by the speeding electrons which move towards the anode. The ratio of the fast signal to the total signal is given by,

$$\frac{Q_{fast}}{Q_{slow}} = \frac{1}{\alpha D} \approx 0.07$$

where, D is the gas-gap and α is the first Townsend coefficient. In other words, only 7% of the total charge generates the fast signal which is detected in MRPC. The resulting signal is the sum of the induced signal from all the gas-gaps which basically increases the amplitude of the output pulse.

3.2.3 Signal Induction in MRPC

As already mentioned that in MRPCs the readout strips are placed above the conductive graphite coating separated by an insulating Mylar sheet. These readout strips are kept at zero potential. The signal on the readout strips is induced by the movement of charged particles. In the presence of an infinite grounded metal plane, a point charge (q) will induce a total charge (-q). In case of MRPC, the plane which is grounded is segmented in the form of strips which act as readout electrodes for the output signal. Now, due to the movement of a charged particle (q), charge distribution will change as shown in figure 3.11 and hence the induced charge on each strip will change. In this way, the movement of a charged particle induces a current in the readout strips in MRPC. The induced current on a grounded electrode by a charge q moving along a trajectory $\vec{x}(t)$ can be calculated using *Ramo's theorem* [RAM39, Rie02]. The total induced current is the sum over all the clusters. The induced current for one such cluster is given by,

$$I(t) = qN(t)\vec{E_w}(\vec{x}(t)) \cdot \dot{\vec{x}}(t)$$

where, q is the electron charge, N(t) is number of electrons at time t which can be calcu-

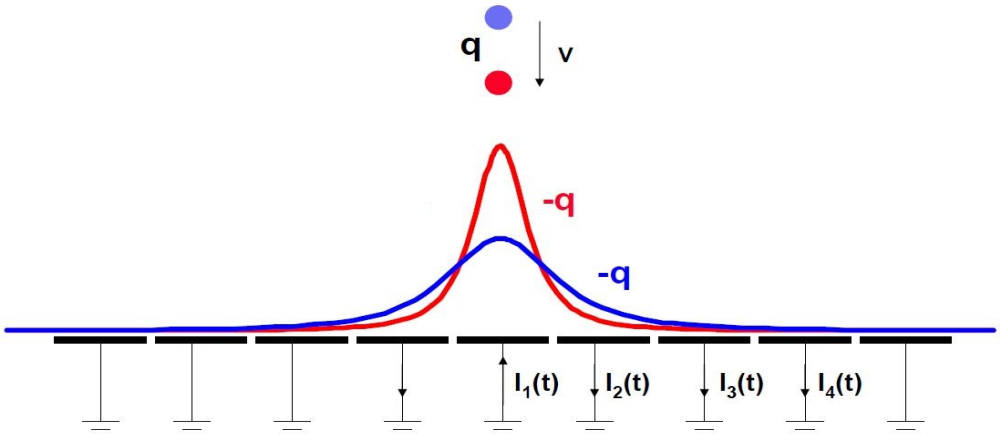

Figure 3.11: Change in the induced charge distribution in the readout strips due to the movement of a charged particle.

lated by the simulation of avalanches of the individual primary electrons, $\dot{\vec{x}}(t) = \vec{v}(t)$ is the electron drift velocity and $\vec{E_w}(\vec{x}(t))$ is the electric field in the gas-gap if the charge (q) is removed and the electrode in question is raised to the unit potential while other electrodes are grounded. This electric field $\vec{E_w}(\vec{x}(t))$ is called as the *normalized weighting field*. Figure 3.12 shows a schematic of the signal induction process using a weighting field.

The physical significance of the weighting field vector is how well a charge moving with the velocity $\vec{v}(\vec{x}, t)$ at position $\vec{x}$ couples into the electrode thereby giving a current per coulomb of charge. The weighting field for the MRPC geometry with n gaps and m electrodes is

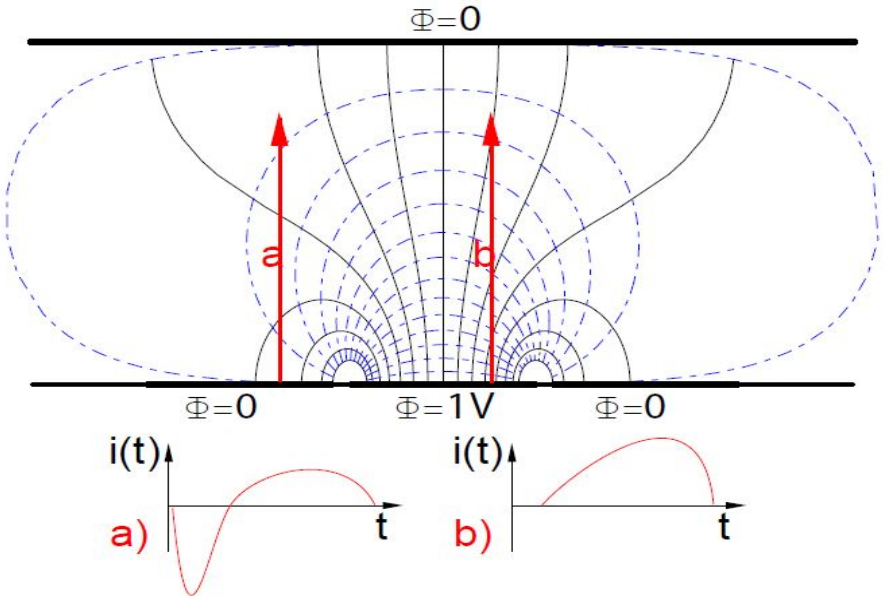

Figure 3.12: Schematic plot of the weighting field in a strip detector and the signal induction process in two examples. The induced current is calculated using the scalar product of the weighting field vector and the velocity vectors of the moving charges.

given by [Bae],

$$E_w = \frac{\epsilon_{elec}\epsilon_{gas}}{nd\epsilon_{elec} + mb\epsilon_{gas}}$$

where, ϵ_{elec} and ϵ_{gas} are the dielectric constants of the resistive electrodes, d is the thickness of the gas-gap and b is the electrode thickness. The time integral of the induced current gives the induced charge in MRPC.

3.3 Summary of the Advantages of MRPC over conventional RPC

Having understood the basic working principle of the MRPC and how it solves the problems related to single gap RPCs, it is best to summarize all the advantages of MRPCs over conventional RPCs which will help to strengthen the motivation to invest our resources on the research and development of MRPCs which promises better physics results in the near future.

Following is the summary of the advantages of MRPCs over conventional RPCs (the reasons behind these merits are already explained in the previous section),

- MRPCs have better time resolution (less than 100 picoseconds) compared to single gap conventional RPCs (which have the time resolution of few nanoseconds).

- Additional sub-gaps in MRPCs improves the space-charge effect which limits the avalanche growth resulting in longer streamer-free efficiency plateau.
- Narrow gas-gaps in MRPCs also result in reduced time-jitters in the output signal and dark current is also reduced.
- Recombination of positive and negative ions in smaller gas-gaps improves the ratio of the fast signal to the total signal and also improves the rate capability. MRPCs have rate capabilities of few KHz/cm^2, whereas RPCs have rate capabilities of few hundreds of KHz/cm^2.
- In MRPCs, the resulting induced signal is the sum of the signal from all the gas-gaps which results in the increased amplitude of the output pulse.
- In MRPCs, any aging-effects are largely reduced (due to strong space charge effects) which is the main problem with the conventional RPCs.
- MRPCs are also cost-effective detectors and can be used in large numbers either in accelerator-based or in Gamma-ray experiments.

3.4 Other Applications of MRPC

Multigap Resistive Plate Chamber (MRPC), because of its much better time resolution, high rate capability and relatively low manufacturing cost finds applications not only for particle identification in high energy and astroparticle physics, but also in various societal applications as discussed below (following is the brief list of applications of MRPC which are discussed in more details in the appendix),

- Multi-gap Resistive Plate Chamber (MRPC) detectors have been used as Time-of-Flight detectors devoted to charged hadron identification in the mid-rapidity region of the ALICE experiment at Large Hadron Collider (LHC).
- They have also been implemented at STAR detector at Relativistic Heavy-Ion Collider (RHIC) at the Brookhaven National Laboratory as TOF detectors.
- MRPC is also used in Medical Imaging as an efficient detector for the Time of Flight (TOF) based Positron Emission Tomography (PET), where the sensitivity of the system depends largely on the time resolution of the detector.
- MRPC also finds an application in Muon tomography with cosmic ray muons which is a novel technology for high-Z material detection.

Having understood the basic working principle of the Multigap Resistive Plate Chamber (MRPC), it is time to get into the real business i.e., to work out an MRPC detector which can be used for various applications and the first step towards the realization of an MRPC detector (to make MRPC in the laboratory) is to simulate one by incorporating all the possible parameters so that we can make the desired MRPC detector in the laboratory later. The following chapter discusses various computer tools for the simulation of an MRPC (or gaseous detector in general).

Chapter 4

Computer tools for the Simulation of MRPC

4.1 Basic Strategy for the Simulation

From the description of the gaseous detectors given in Chapter-2, we have very well understood the basic processes such as ionization, charge amplification, transport properties and various detector characteristics which are involved in order to fully exploit the endless applications of gas-based detectors. The simulation of detectors, in general, provides us a tool to improve various properties associated with the working of a detector used for a particular application without actually making the detector in practice which may cause wastage of resources if the detector doesn't work the way as it was anticipated. Thus, simulation plays an important role in the research and development of various detectors in high energy physics.

The basic strategy for the simulation of gas-based detectors is as follow,

- Various parameters related to detector geometry is defined using a simulation package called 'Garfield'.
- Calculations related to the weighting field, the electromagnetic field, and the potential is carried out using the 'neBEM (nearly exact boundary element method)' field-solver. Other methods used to calculate electrostatic potential and field in gaseous detectors are the analytic method, the finite element method (FEM) and the boundary element method (BEM) [Vee09].
- Gas mixture to be used in the detector is made using another tool called 'Magboltz' which is interfaced with Garfield program and it also helps to calculate various elec-

tron transport properties such as drift velocity, Townsend and attachment coefficients etc.

- Ionization, which is the dominant process by which an incoming charged particle loses energy in the gaseous detectors, results in the formation of clusters containing ion-electron pairs which are modeled using yet another program called 'HEED' and it also gives information about the gas gain. It uses various methods for tracking particles such as Runge-Kutta-Fehlberg (RKF), Monte-Carlo (MC), microscopic integration methods.

- Finally, the signal which can be either direct or an induced one is generated using Garfield package and is analyzed to improve the detector characteristics. Figure 4.1 shows a schematic of the basic strategy used for simulating gaseous detector.

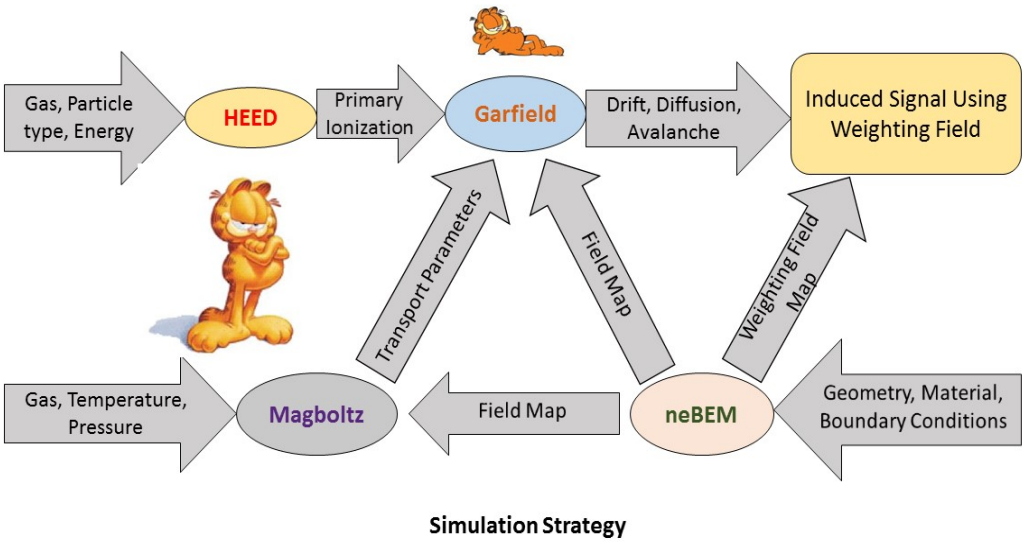

Figure 4.1: Strategy for Simulating Gaseous Detectors Using Garfield.

We have used Garfield, Magboltz and HEED simulation tools for simulating 5-gap MRPC. These simulation packages are explained in detail in the following sections.

4.2 Garfield

Garfield is a computer simulation program used for the detailed simulation of two and three-dimensional drift chambers. It was designed by Rob Veenhof back in 1984 at CERN. We have used Garfield Version-9 which is written in Fortran-77 for the simulation of five gap MRPC. This program can calculate field maps, arrival time distribution, x(t) relations,

drift velocity and diffusion in gases, induced signals [Vee93] etc. Originally, Garfield was written for defectors such as drift chambers, time projection chambers (TPCs), multiwire counters etc. in which two-dimensional wires and planes are used. It uses Monte-Carlo techniques for tracking particles inside the detectors [Sch]. In order to handle relatively sophisticated detectors containing dielectric materials and complex geometries in three dimensions, Garfield is interfaced with neBEM (nearly exact boundary element method) program which defines field maps for two or three-dimensional complex geometries. To calculate electron transport properties like the drift velocity, the Townsend and the attachment coefficients in an arbitrary gas mixture, Garfield is interfaced to the *Magboltz* program. And to get information about the clusters formed during ionization of the gas molecules by an incoming particle, Garfield is interfaced to *Heed* program.

In brief, Garfield can perform the following tasks [Vee93, Veed],

- It can plot any function of the field as a vector plot, histogram, counter lines, 3-dimensional surface plot.
- It can assist us in finding an optimum potential setting for various conditions.
- It calculates and plots electron and ion drift lines.
- It can calculate x(t) relation, arrival time distributions and can produce drift-time tables.
- It also simulates the induced signal on the sense wires or the specified electrodes when a charged particle traverses the defined geometry.

The input to the Garfield is structured in a set of sections (cell, gas, magnetic, optimize, field, drift, and signal) and each section contains a set of instructions performing certain tasks. Some primers before using Garfield are,

- Different sections in Garfield are initiated using a header which is prefixed by an ampersand (&), for example, to initiate 'CELL' section, we write '&CELL' and so on.
- The order of the sections is of some importance, for example, the &CELL and the &GAS sections should appear before other sections which may use their data. Sections can be repeated any number of times in Garfield.
- Using &STOP (or &EXIT or &QUIT) stops the execution of the program.
- Use of an ellipsis (...) at the end of a line in the program indicated that the instruction continues on the next line.

- On each line in the program, the first word is the proper command and other words after this can be a set of parameters which may have some assigned values.
- A blank ( ), a colon (:), a comma (,) or an equality sign (=) can be used to separate elements on the input.
- The commands in Garfield are not case sensitive. Where the input is written in upper or lower case, it will be translated to upper-case, unless it is enclosed by double quotes.
- It is better to make different files for geometry, field and signal generation for the ease of modification and execution.
- Although Garfield is not a programming language, but can be treated like one. We can use batch files or copy the code directly into Garfield.
- Default values for different parameters are indicated by an asterisk '$*$'.
- Using 'Global' command, a value to the global variable can be assigned.
- The default physical units used by Garfield for input and output are shown in figure 4.2

Physical units. Overview of physical units as used in Garfield

quantity	**unit**	**symbol**
distances	centimeter	[cm]
angles	degrees	[deg]
times	micro second	[μsec]
currents	micro ampere	[μA]
voltages	volt	[V]
pressures	torr	[torr]
energies	electron volt	[eV]
magnetic field		[Vμsec/cm^2]

Note: Note the unusual unit for magnetic fields ! Internally, charges per unit length are expressed in multiples of $1/2\pi\varepsilon_0$ and angles in radians. The built-in trigonometric functions also work in radians.

Figure 4.2: Different physical unites used by Garfield [Vee93].

The input to the Garfield is sub-divided into the following sections (information is taken from references [Vee93, Veed, Veeb, Jan]) ,

- *The Cell Section:* This section is entered using a header &CELL. The cell section allows us to define a geometry as per our requirement. We can either use polar or Cartesian coordinate for listing the cells (mixed coordinates are not allowed). The default coordinate used in Garfield is the Cartesian coordinate. Different commands used in this section are as follow,

Table 4.1: Commands used in the Cell section

Command	Description	Format
CELL-IDENTIFIER	Assigns an identification string to the cell description which can be used later in the plots whenever necessary (enclose the string by double quotes).	CELL-IDENTIFIER “string"
DEFINE	Defines a symbolic variable which can be used in the listing of the rows. It should appear before the wire listing.	DEFINE variable value
WRITE	Writes a compact format cell data file which later can be retrieved using ‘GET’ command.	WRITE DATASET file [member] [REMARK remark]
GET	Retrieves a compact format cell data file written using ‘WRITE’ command. This command is useful to avoid repetitions of cell description for different simulation steps.	GET file [member]

Continued on next page

Table 4.1 – continued from previous page

Command	Description	Format
OPTIONS	Selects some options for the cell. Options like 'CELL-PRINT' prints a detailed description of the cell when the cell section is left, 'WIRE-MARKERS' plots wires as polymarkers instead of circles, 'LAYOUT' plots the layout of the cell etc.	OPTIONS [NOLAYOUT|LAYOUT] [NOCELL-PRINT|CELL-PRINT] [NOTISOMETRIC|ISOMETRIC] [NOWIRE-MARKERS|WIRE-MARKERS] [NOCHARGE-CHECK|CHARGE-CHECK] [NODIPOLE-TERMS|DIPOLE-TERMS]
PERIODICITY	Indicates that the cell is periodic in the specified direction (x, y, ϕ) and the period repeats after the specified length.	PERIODICITY direction = length
PLANE	Defines an infinite equipotential plane at constant x, y ϕ or a circular plane with constant radius r.	PLANE direction coordinate [V potential] [LABEL label]
ROWS	Introduces wires in a cell. The wires are assumed to have infinite length along z-axis and the default diameter is 0.01 cm. Properties of the wires like the label which identifies the kind of wire (S for sense wires), the position, the potential, the diameter, the length etc. can be entered in this command.	ROWS [CARTESIAN|POLAR|TUBE] label n diameter x y [V [weight [length [density]]]]

Continued on next page

Table 4.1 – continued from previous page

Command	Description	Format
SOLIDS	Adds solid volumes to the chamber. This command generates fields with neBEM field solver. Shapes such as box, cylinder, extrusion, hole, ridge, sphere, wire etc. are available in the Solids command and are added followed by the specific parameters defining the required geometry.	SOLIDS BOX or CYLINDER or EXTRUSION or HOLE or RIDGE or SPHERE or WIRE parameters
TUBE	Defines a tube surrounding a wire. A tube can be of any shape (circular, triangular etc.) for which an option of 'edges' is provided. This command is useful as a wire cannot be placed at the exact center of a cell defined by circular plane.	TUBE [RADIUS r] [VOLTAGE v] [EDGES n] [LABEL label]

- *The Gas Section:* This section is entered using a header &GAS. The Gas section allows us to build the gas mixture which is used when drifting electrons and ions. Garfield has built-in gases and gas-mixtures which can be used or else a new gas-mixture can be established using this command. This section makes use of other programs such as Magboltz and HEED for calculating transport properties like the drift velocity, the Townsend and the attachment coefficients and information about the clusters formed during ionization. If we have experimental data for the various transport properties, we can also enter this data in the form of tables. Different commands used in this section are as follow,

Table 4.2: Commands used in the Gas section

Command	Description	Format
PRESSURE	Sets the pressure of the gas to be used. Default pressure value stored in Garfield is 760 Torr.	PRESSURE pressure [unit]
TEMPERATURE	Sets the pressure of the gas to be used. Default pressure value stored in Garfield is 300 K.	TEMPERATURE temp [unit]
MAGBOLTZ	Calls the Magboltz program to compute the drift velocity, the Townsend and the attachment coefficients, the longitudinal and the diffusion coefficients, the excitation and the ionization rates etc. for electrons. Magboltz is more accurate than the MIX command in this section as it takes the cross-sections for the non-elastic processes into account.	MAGBOLTZ [gas mixture in %]
HEED	Calls the HEED program which simulates the simulates the energy loss of a particle traversing through the gas mixture through ionization and gives information about the clusters formed during ionization. The temperature and pressure should be specified before using HEED command.	HEED [gas mixture in %]

Continued on next page

Table 4.2 – continued from previous page

Command	Description	Format
WRITE	Writes a compact format gas data-set which later can be retrieved using the GET command.	WRITE DATASET file [member] [remark]
GET	Retrieves a compact format gas data-set written using WRITE command .	GET file [member]
OPTIONS	Plots and prints gas tables.	OPTIONS [NOGAS-PLOT|GAS-PLOT] [NOGAS-PRINT|GAS-PRINT]
ADD	Adds or replaces elements or items such as drift velocity, ion-mobility etc. to/of the gas tables. For example, this command can be used to add ion-mobility to the transport tables prepared using Magboltz.	ADD item value

- *The Field Section:* This section is initiated using a header &FIELD. The Field section is used to plot electrostatic aspects of the simulation such as the electric field, the potential contours etc. Different commands used in this section are as follow,

Table 4.3: Commands used in the Field section

Command	Description	Format
AREA	In the Field section, Area command is used to select an area of the chamber for which electric field or contours need to be plotted.	AREA [xmin ymin xmax ymax|xmin ymin zmin xmax ymax zmax]
TRACK	Defines a track which can be used to make graphs using Plot-Field command.	TRACK x_start y_start x_end y_end
TEMPERATURE	Sets the pressure of the gas to be used. Default pressure value stored in Garfield is 300 K.	TEMPERATURE temp [unit]
GRID	Sets the number of sampling points used to produce plots and tables. The first parameter *grid_x*, is the number of x or r divisions and the second parameter *grid_y* is the y or ϕ divisions. We may assign value to only one argument in which case the value will be assigned for both the arguments. default number of grid divisions for both the arguments is 25.	GRID grid_x [grid_y]
PLOT-FIELD	Plots the contours, an histogram, a surface plot, a graph, a vector plot etc. for the electric and the magnetic fields.	PLOT HIST VECTOR SURF CONT

- *The Drift Section:* This section begins with a header &DRIFT. The Drift section is devoted to displaying the movement of electrons and ions in the chamber. This

section enables us to plot drift-lines for electrons and ions. Different commands used in this section are as follow,

Table 4.4: Commands used in the Drift section

Command	Description	Format
AREA	Defines an area in which electrons and ions are allowed to drift. It also establishes the viewing direction for the plots related to drift-lines.	AREA xmin ymin zmin xmax ymax zmax
TRACK	Defines a track which can be used with the DRIFT TRACK command.	TRACK x_start y_start z_start x_end y_end z_end
DRIFT	This instruction plots drift lines for electrons and ions as well as the contours of equal arrival time or isochrones (lines which connect points of equal travel time). The drift has five starting points which are, the TRACK, the EDGES of the AREA, the surface of WIRES and of SOLIDS, and the ZEROES of the electrostatic field. Each of these starting points have sub-options which can be indicated within this section.	DRIFT EDGES/TRACK/-SOLIDS/WIRES/ZEROES other-parameters

Continued on next page

Table 4.4 – continued from previous page

Command	Description	Format
INTEGRATION-PARAMETERS	This command enables the change in the accuracy of the Runge Kutta Fehlberg drift-line integration, step size of Monte Carlo drifting, the range of diffusion scaling factors in Monte Carlo drifting, isochrons, the method of projecting the cloud into the wire etc. Garfield has four integration techniques which are, Runge-Kutta-Fehlberg, Monte-Carlo, microscopic integration [Veec].	INTEGRATION-PARAMETERS [DIFFUSION-ACCURACY e_diff] [TOWNSEND-ACCURACY e_a] [DIFFUSION-STACK-DEPTH stack_diff] [TOWNSEND-STACK-DEPTH stack_a]

- *The Signal Section:* This section is entered using a header &SIGNAL. The Signal section is used to simulate the signal induced on the sense wires or the specified electrodes due to the movement of the charged particles in the detector. The signal registered at the specified electrodes can be either direct or induced as per the detector design. Signal information can be stored in a file for analysis. Different commands used in this section are as follow,

Table 4.5: Commands used in the Signal section

Command	Description	Format
AREA	Defines an area in which electrons and ions are allowed to drift. It is the part of the chamber used for plotting. The Drift and the Signal part uses common area for drifting and signal generation as well as for plotting various parameters.	AREA xmin ymin zmin xmax ymax zmax
AVALANCHE	Sets the probability distribution which can be used for the avalanche multiplication factor in the signal simulation. For example, if we set the avalanche as Townsend avalanche, the the multiplication factor will be exponential as we have seen earlier for the Townsend avalanche. Avalanches generated by the electrons hitting the electrodes are the ones affected by this command. No default avalanche is set.	AVALANCHE EXPONENTIAL mean|FIXED factor|FIXED-TOWNSEND|GAUSSIAN mean relative_sigma|NONE|POLYA-FIXED [mean [theta]]|POLYA-TOWNSEND [theta]|TOWNSEND
SELECT	Selects the electrodes for which signals are be computed when SIGNAL command is issued. Electrodes which are labelled in the Cell section are generally selected for signal generation. Signals for the labels enclosed within the brackets (e.g. (SR)) will be summed.	SELECT wire-codes

Continued on next page

Table 4.5 – continued from previous page

Command	Description	Format
TRACK	Specifies the place and the kind of particle which will traverse through the chamber. Clustering model such as HEED is also specified using this command.	TRACK [x0 y0 z0 x1 y1 z1] [HEED] [DELTA-ELECTRONS|NODELTA-ELECTRONS] [TRACE-DELTA-ELECTRONS|NOTRACE-DELTA-ELECTRONS] [NOMULTIPLE-SCATTERING|MULTIPLE-SCATTERING] [particle|MASS mass CHARGE charge] [ENERGY energy]
WINDOW	Sets the window of start and end time for the signal with step size. By default, the signal starts at t=0 with sampling it every 0.01μs. Using this command we can specify when to start the signal (t_start), step size of the signal (t_step) and total number of steps (n_step). Note that the unit used for time is microsecond.	WINDOW t_start t_step [n_step]
WRITE-SIGNALS	Writes the signal information in a data file which can be used later for analysis.	WRITE-SIGNALS [FILE-NAME file [member]] [REMARK remark] [FORMAT SPICE|SCEPTRE|SORIN] [WRITE-IF condition] [UNITS units]

Continued on next page

Table 4.5 – continued from previous page

Command	Description	Format
OPTIONS	Allows some local options to control the amount of output in the signal section. Using this command we can request printing the table of clusters, plot the track of the charged particle with the position and the drift-lines of the clusters, request the drawing of contours across all non-conducting media etc.	OPTIONS [CLUSTER-PRINT|NOCLUSTER-PRINT] [CLUSTER-PLOT|NOCLUSTER-PLOT] [CONTOUR-ALL-MEDIA|CONTOUR-DRIFT-MEDIUM] [NOWIRE-MARKERS|WIRE-MARKERS] [NOCHECK-MAP-INDICES|CHECK-MAP-INDICES]
SIGNAL	Computes the signals on the electrodes due to the passage of charged particles through the detector. Area, Track, Avaanche, Window and Select commands must be issued before issuing the Signal command. Signals generated by the hits of electrons onto the elctrodes is called as the “direct-signal" whereas the signal generated due to the movement of charged particle is called as the “cross-induced-signal".	SIGNAL [AVALANCHE|NOAVALANCHE] [DIFFUSION|NODIFFUSION] [ION-TAIL|NOION-TAIL] [NEW|ADD] [NOCROSS-INDUCED-SIGNAL|CROSS-INDUCED-SIGNAL] [NOELECTRON-PULSE|ELECTRON-PULSE] [NOINTERPOLATE-TRACK|INTERPOLATE-TRACK]

Continued on next page

Table 4.5 – continued from previous page

Command	Description	Format
PLOT-SIGNALS	Plots the signals generated using Signal command. If we want to find out which electrods are concerned with which signal, we may use the Select command without any arguments.	PLOT-SIGNALS [TIME-WINDOW AUTOMATIC|tmin tmax] [RANGE AUTOMATIC|smin smax] [WIRES ALL|ACTIVE|numbers, labels] [CROSS-INDUCED-SIGNALS|NOCROSS-INDUCED-SIGNALS] [DIRECT-SIGNALS|NODIRECT-SIGNALS]

4.3 Magboltz

The *Magboltz* program calculates electron transport properties in gases such as the drift velocity, the Townsend and attachment coefficients, the longitudinal and diffusion coefficients etc. by numerically integrating the Boltzmann transport equations for the electrons in gas mixtures with applied electric and magnetic field at arbitrary angles. The first version of this program was written by S.F. Biagi back in 1988. In 1999, he released Magboltz 2 which uses Monte Carlo integration techniques [S.F99]. We have used Magboltz version 7.1 which is interfaced with Garfield-9 for our purpose. In order to calculate electron transport properties like the drift velocity, Magboltz takes into account microscopic parameters such as the scattering cross sections (the measure of how likely the collisions occur), the energy loss per collision etc. of each gas used in the detector. It uses Monte Carlo integration method (traces electrons microscopically through numerous collisions with the gas molecules) to calculate various electron transport properties in gas mixtures. Cross-sections for various gases have been calculated and can be found in reference [Biab]. Details of the algorithm used in the Magboltz and Monte Carlo technique are given in references [S.F99, GF86, Sku68].

4.4 Heed

HEED, which stands for *High Energy Electrodynamics* is a popular tool for the simulation of charged particle ionization in gaseous detectors. It was written by I. Smirnov. Energy loss by a fast-moving charged particle due to ionization in gas-mixtures is well described by the “photo-absorption and ionization (PAI) model" formulated by Allison and Cobb [AC80], which is based on the relation between energy deposited by a charged particle traversing through a medium and the photo-absorption cross-section of the medium, but it does not describe the relaxation processes. HEED besides using the differential cross section of the PAI model, incorporates the relaxation processes along with absorption of the real photons and Auger- and photo- electrons which are emitted for the detailed simulation of primary ionization in gas detectors [Vee09, Sch].

Using the energy loss mechanism of the PAI model and the simulation of atomic relaxation along with microscopic tracking of the emerging δ-electrons, HEED fully simulates the primary ionization in gas mixtures using few parameters such as the electron scattering cross-sections, the photoabsorption cross-sections and the atomic transition probabilities.

Having learned the basic tools for the simulation of gaseous detectors using Garfield simulation package, it is right time to get into the business to optimize the 5-gap RPC to get the desired detector characteristics (in our case it is the best possible time resolution) using Garfield simulation package. In the following Chapter, we elaborately discuss different optimization parameters used for optimizing the 5-gap RPC and also discuss the results which we have obtained for the optimization of 5-gap RPC using Garfield-9 simulation package.

Chapter 5

Optimization of 5-gap MRPC

We have prepared a five-gap glass Multigap Resistive Plate Chamber (MRPC) detector geometry of dimension 20 mm × 20 mm × 6.5 mm using Garfield simulation package. The geometry consists of 6 glass electrodes with dielectric constant 8. The thickness of the outer two electrodes is 1 mm and that of the inner four electrodes is 250 microns each separated by 200 microns gas-gap. Then above the outer electrodes, 50-micron conductive Graphite coat is present (on which the high voltage is applied) above which 200-micron insulating Mylar sheet having dielectric constant as 2 is kept. Finally on each side, 18 readout strips with thickness and width as 1 mm and pitch 0.1 mm are kept in perpendicular orientation so as to get the spatial resolution of the incoming particle along with its time resolution (readout strips are maintained at zero potential). Figure 5.1 shows a schematic of this 5-gap MRPC which we intend to simulate in order to optimize it for the best possible time resolution which later will be made in our experimental high energy physics lab.

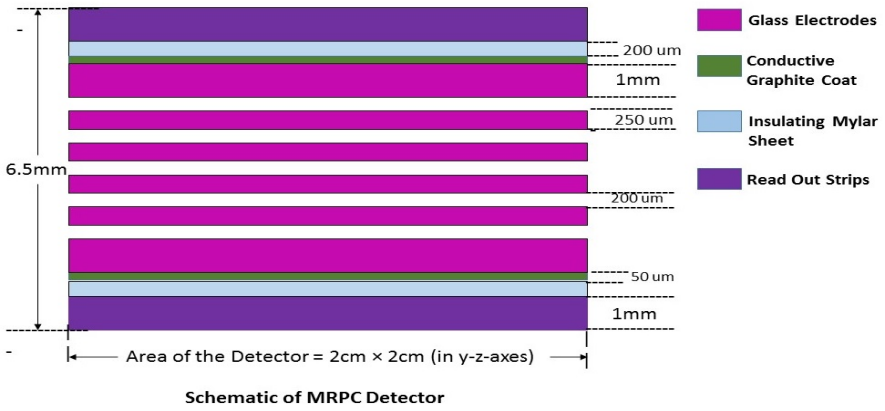

Figure 5.1: Schematic of the 5-gap MRPC detector.

5.1 Geometry construction using Garfield

In the first half of the project, we developed techniques to make the required geometry using Garfield simulation package by providing various dimensional parameters. The idea was to divide 2 mm gas gap used in the conventional RPCs into narrower gaps containing resistive electrodes to improve the time resolution from few nanoseconds to few picoseconds as explained in the previous chapters. Thus, we introduced 5-gap MRPC consisting of four inner glass-electrodes, each with the thickness of 250 microns and dielectric constant 8, resulting in five gas-gaps with the thickness of 200 microns each, thus the total thickness of the inner electrodes and the gas gap is 2 mm as shown in figure 5.1.

For preparing this geometry we have used the *Box* command which can be found in the *Solids* part of the Cell section in Garfield [Veea]. The Box command has various dimensional parameters using which we can construct a three-dimensional box and can also assign it the material properties of a conductor or a dielectric. Thus, this command is suitable for our purpose as we need rectangular electrodes which can either be a conductor or a dielectric. As shown in figure 5.2, the box command has dimensional parameters such as *centre* which specifies the location of the center of gravity for the required box, *half-lengths* which specifies half of the lengths for the box and *direction* specifying the orientation of the box. Other parameters include, *voltage* and *charge* which are used for applying voltage and charge to the box if it is conducting, *epsilon* defines the dielectric constant for the dielectric box, *material* lets us choose whether the box is a conductor or a dielectric, *label* helps us to mark the box which later can be used in the Signal section for obtaining signals on the marked electrodes.

```
box   centre -0.2525 0.0000 0.9200 ...
      half-lengths 0.0500 1.0000 0.0500 ...
      conductor-2 ...
      voltage 0 ...
      LABEL S
box   centre -0.1925 0.0000 0.0000 ...
      half-lengths 0.0100 1.0000 1.0000 ...
      dielectricum-2 ...
      epsilon 2
box   centre -0.1800 0.0000 0.0000 ...
      half-lengths 0.0025 1.0000 1.0000 ...
      conductor-1 ...
      voltage 5000 ...
      LABEL q
```

Figure 5.2: Example of a Box command for making 3-dimensional boxes using Garfield.

Different voltages are applied to the conductive graphite electrodes which will create a uniform electric field in the gas gaps. As already mentioned in Chapter-3 that the intermediate electrodes are electrically floating i.e., no direct voltage source is applied to them and they acquire the potential via electrostatics thereby maintaining a uniform gas-gain (or uniform electric field) in all the gas-gaps because of their self-potential regulating ability. For the five-gap MRPC, if the voltage applied on the conductive graphite electrodes is V_1 and V_2, then the intermediate floating electrodes (a, b, c, d) assume potential via electrostatics as shown in figure 5.3.

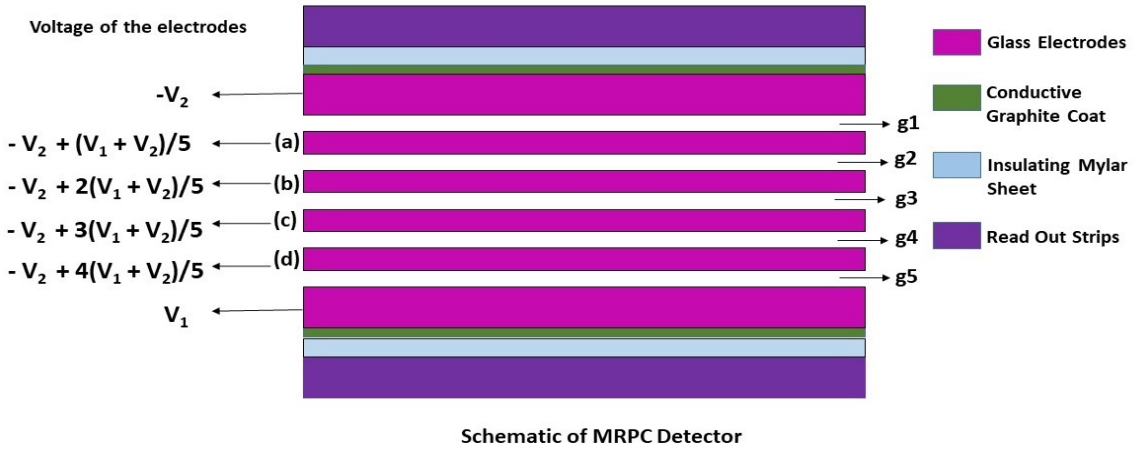

Figure 5.3: Voltage acquired by the floating electrodes in 5-gap MRPC if the voltage on the conductive graphite electrodes is set to V_1 and V_2.

The neBEM (nearly exact boundary element method) field solver program which is interfaced with Garfield-9 is used for solving electrostatic fields and potentials for our purpose. Figure 5.4 shows the geometry of the 5-gap MRPC constructed using Garfield-9 simulation package.

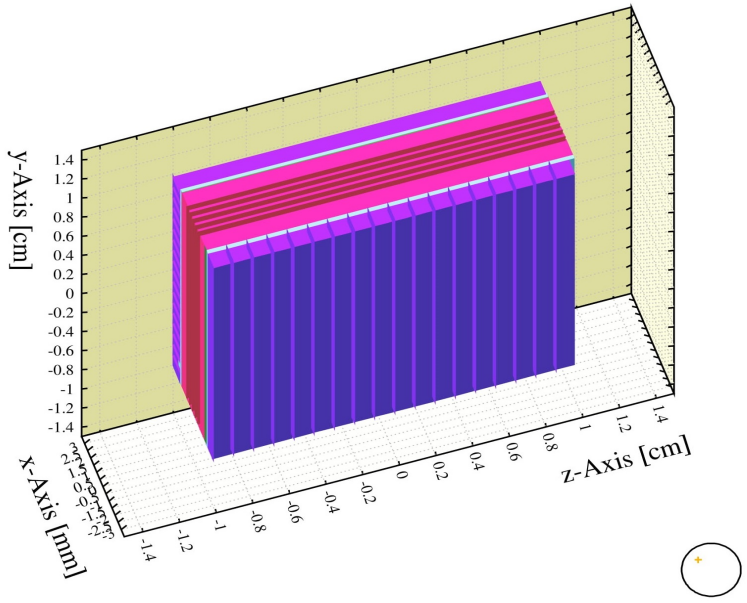

Figure 5.4: Geometry of the the 5-gap MRPC detector prepared using Garfield-9 simulation package.

As discussed in the previous Chapter that contours of the electrostatic potential as well as the vector plots for the electric field in x-, y- and z- directions can also be plotted using the Field section in Garfield-9 which is shown is figure 5.5 for the potential difference across the conductive graphite sheet as 12000 V (6000 V and -6000 V applied on the two

conductive graphite electrodes).

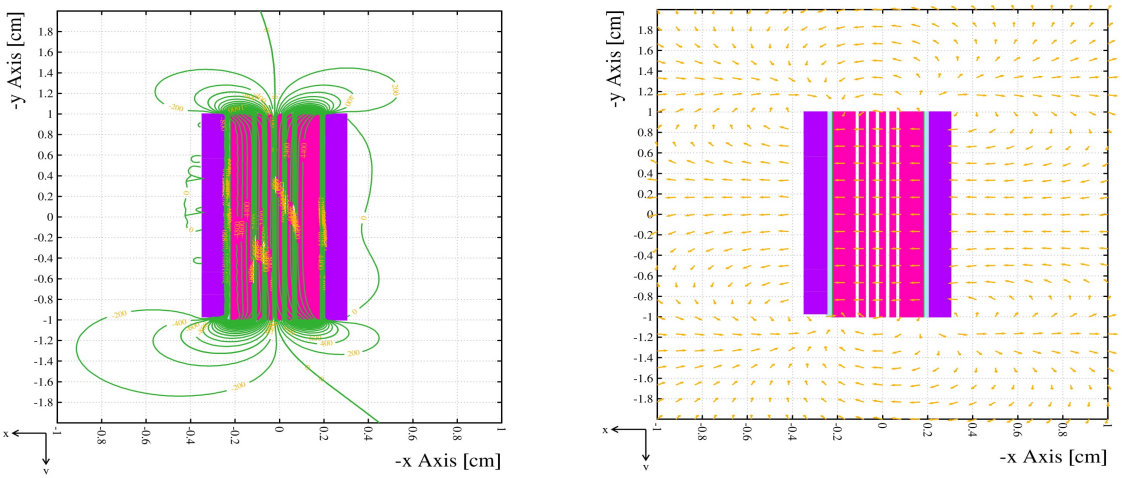

(a) Contours of potential V.

(b) Vector plot for electric fields in x-, y-, and z-directions.

Figure 5.5: Potential contours and vector plots for E_x, E_y, E_z for the 5-gap MRPC geometry with 200 micron gas gap and 12000V potentail difference across conductive graphite electrodes.

5.2 Simulating Gas Mixtures and Transport Properties using Magboltz

We have used two gas-mixtures (reasons will be clear in the following sections) i.e., 3.5% $i-C_4H_{10}$, 96% $C_2F_4H_2$, 0.5% SF_6 and 6% $i-C_4H_{10}$, 90% $C_2F_4H_2$, 4% SF_6. $C_2F_4H_2$ (1,1,2,2-Tetrafluoroethane also known as R-134a) is a heavy non-flammable gas which is to be ionized by an incoming minimum ionizing particle, $i-C_4H_{10}$ (iso-butane) is a quencher gas to absorb soft X-rays which can induce streamer mode and SF_6 (Sulfur hexafluoride) is an electronegative gas to prevent high multiplication process which again will result in the streamer mode. The gas mixtures have been prepared using Magboltz-7.1 package which is interfaced with Garfield-9. The cross sections for these gases used by Magboltz 7.1 are shown in Appendix A.

All the gas mixtures are used at 1 atm pressure and 300 K temperature. Magboltz also calculates electron transport properties such as the drift velocity, the longitudinal and transverse diffusion coefficients, the Townsend coefficient, the attachment coefficient etc. Magboltz along with HEED also helps to calculate ionization and excitation rates for different gas mixtures. Ion mobility is fixed to 1.5×10^{-6} cm^2/V/s. The plots of the various transport

properties versus electric field (varied from 100 to 100000 V/cm) obtained for the 5-gap RPC with 200 micron gas-gaps and gas mixture 3.5% $i-C_4H_{10}$, 96% $C_2F_4H_2$, 0.5% SF_6 are shown in figure 5.6.

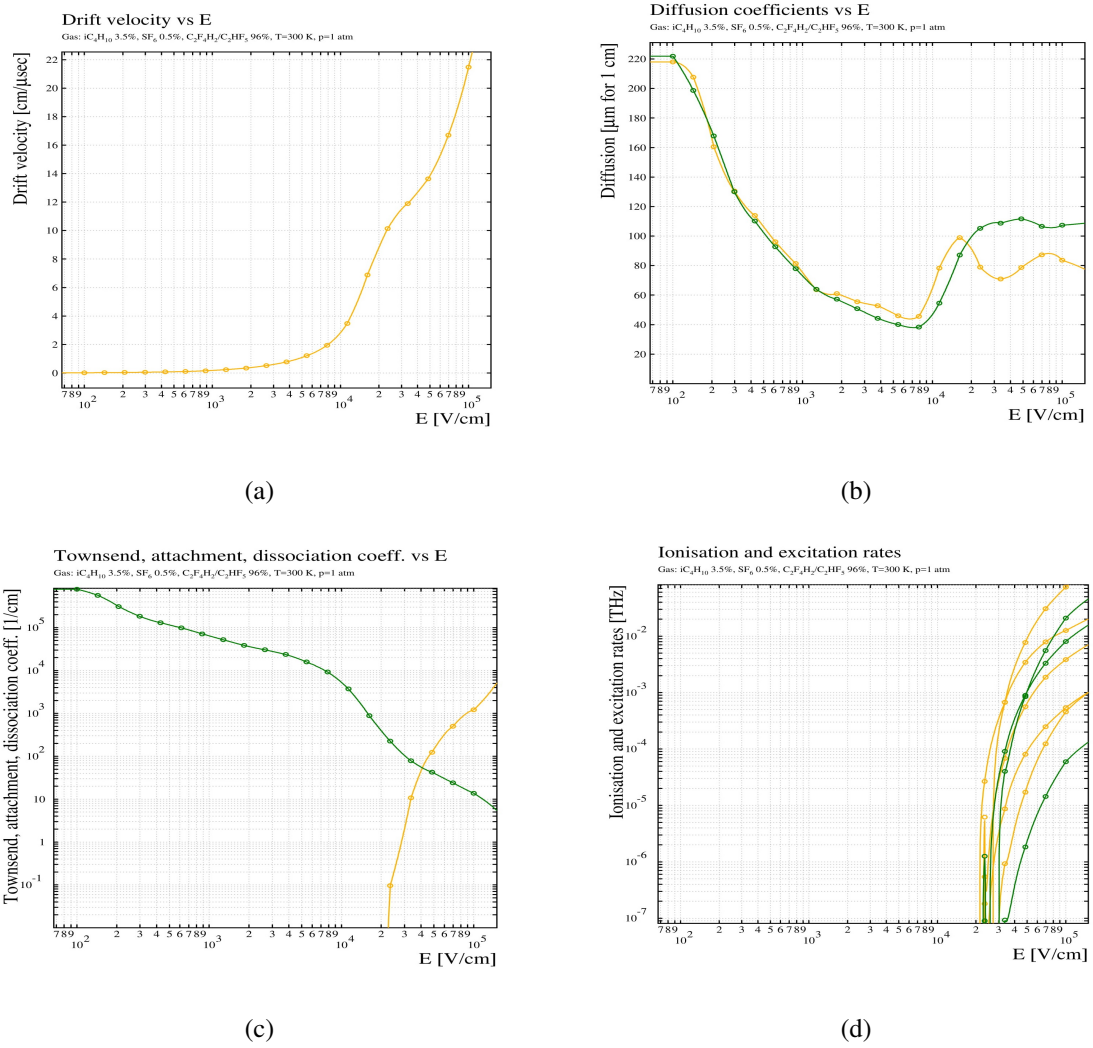

Figure 5.6: Plots of various transport properties versus electric field obtained for the 5-gap RPC with 200 micron gas-gaps and gas mixture 3.5% $i-C_4H_{10}$, 96% $C_2F_4H_2$, 0.5% SF_6 using Magboltz package. a)Drift velocity vs Electric field; b)Ion mobility vs Electric field; c)Diffusion coefficients vs Electric field; d)Townsend and attachment coefficients vs Electric field; e)Ionization and excitation rates vs Electric field.

And the plots of the various transport properties versus electric field (varied from 100 to 100000 V/cm) obtained for the 5-gap RPC with 200 micron gas-gaps and gas mixture 6% $i-C_4H_{10}$, 90% $C_2F_4H_2$, 4% SF_6 are shown in figure 5.7.

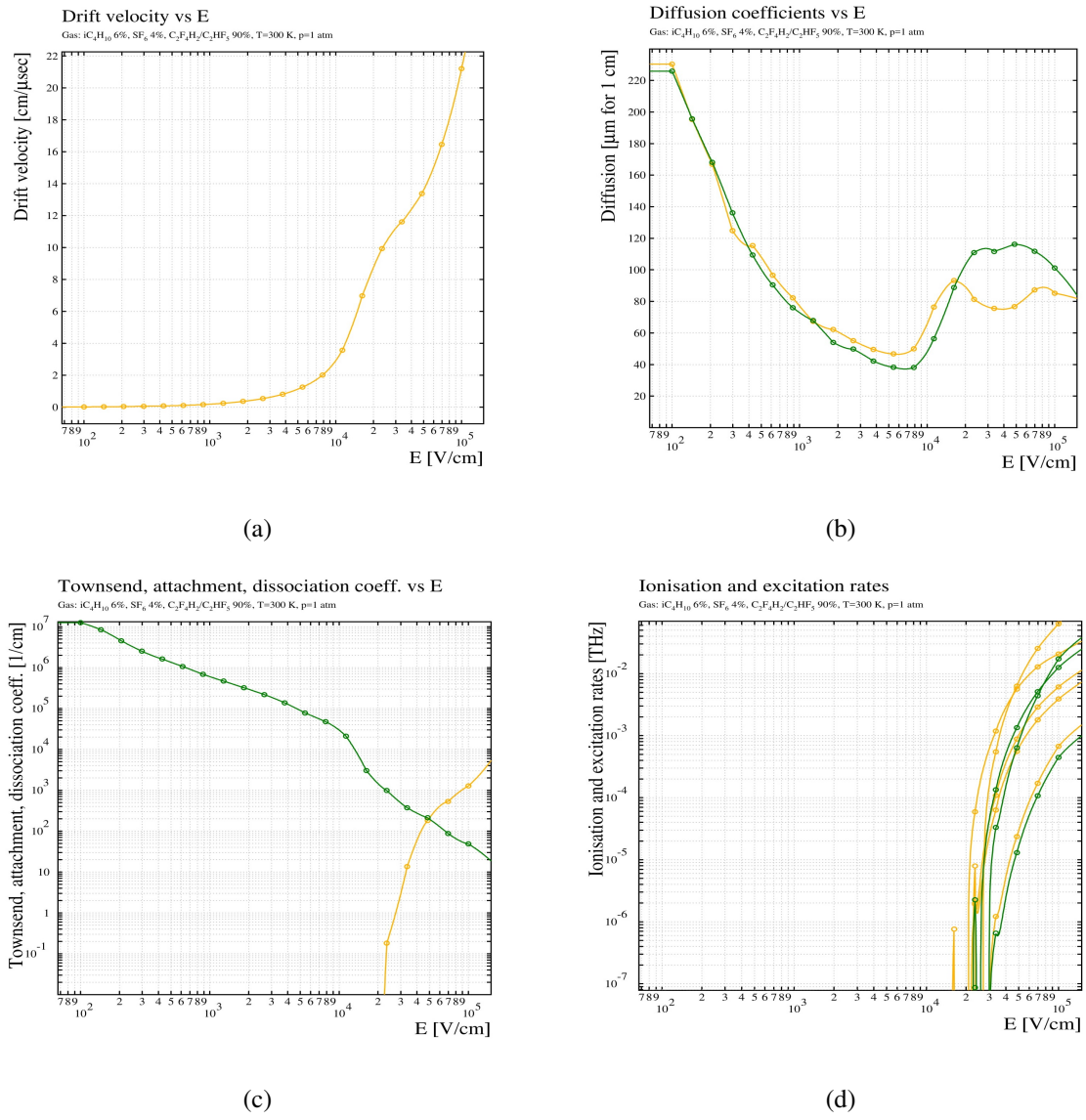

Figure 5.7: Plots of various transport properties versus electric field obtained for the 5-gap RPC with 200 micron gas-gaps and gas mixture 3.5% $i-C_4H_{10}$, 96% $C_2F_4H_2$, 0.5% SF_6 using Magboltz package. a)Drift velocity vs Electric field; b)Ion mobility vs Electric field; c)Diffusion coefficients vs Electric field; d)Townsend and attachment coefficients vs Electric field; e)Ionization and excitation rates vs Electric field.

5.3 Simulation of 5-Gap RPC with 200 micron gas-gaps

Our aim is to optimize the 5-gap RPC geometry which we have created using Garfield-9 simulation package so that we can obtain the best possible time resolution. The optimization parameters are the geometry (gas-gaps can be altered), the electric field or voltage applied on the conductive graphite electrodes and the gas mixture. We started optimizing the 5-gap RPC having 200-micron gas-gaps (the geometry which is discussed in the previous section) with 7 different gas mixtures which are being used at various experimental facilities worldwide. We have used 1 GeV muon with the negative charge (μ^-) as an incoming minimum ionizing particle which will traverse the detector and cause ionization. The particle is being passed perpendicular to the detector as shown in figure 5.8, so that the signal can conveniently be obtained only from those pick-up electrodes from which the particle will pass before entering and after leaving the detector. In general, the particle hits the detector at a certain angle which we are ignoring (because of this we might obtain more or less an ideal signal, but it won't make much difference even when the angle of an incoming particle is taken into account). Figure 5.8 also shows the drift lines of electrons and ions when they drift towards the respective electrodes under the influence of an external electric field.

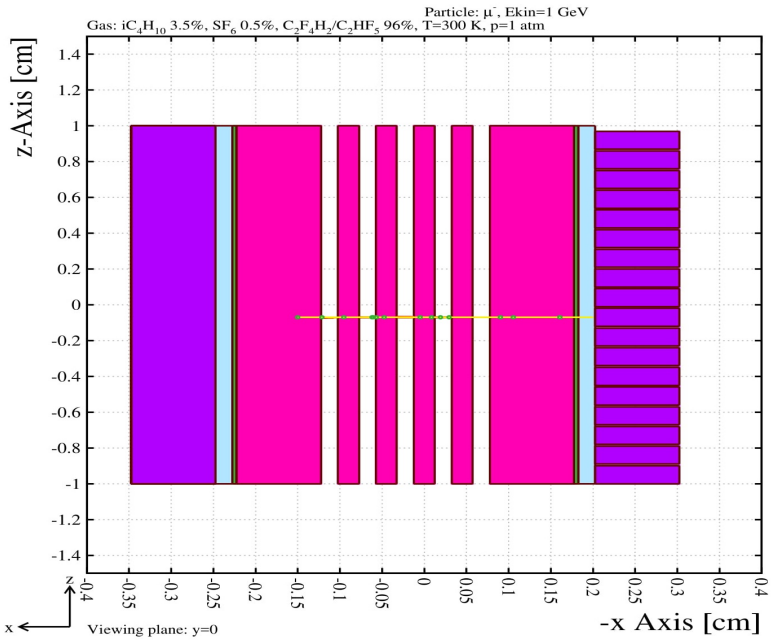

Figure 5.8: Track and drift lines of electrons and ions under the influence of an external electric field in the 5-gap RPC with 200 microns gas-gaps.

Figure 5.9 shows the signals obtained using following parameters,

– the voltage applied across the graphite electrodes is 12000 V (i.e., 6000 V and -6000 V on

each graphite electrode which results in the electric field of 120 KV/cm in each gas-gap),
– the geometry of the 5-gap RPC with 200-micron gasp-gaps which is described in the previous section is used for the simulation, thus two of the three parameters i.e., geometry and voltage are fixed and only the gas-mixture is altered for the following simulations.

Gas mixtures which are used are:

a) $i-C_4H_{10}$ = 5%, $C_2F_4H_2$ = 35%, Ar = 60%;

b) $i-C_4H_{10}$ = 10%, $C_2F_4H_2$ = 40%, Ar = 50%;

c) $i-C_4H_{10}$ = 8%, $C_2F_4H_2$ = 62%, Ar = 30%;

d) $i-C_4H_{10}$ = 6%, $C_2F_4H_2$ = 90%, SF_6 = 4%;

e) $i-C_4H_{10}$ = 3.9%, $C_2F_4H_2$ = 96%, SF_6 = 0.1%;

f) $i-C_4H_{10}$ = 3.7%, $C_2F_4H_2$ = 96%, SF_6 = 0.3%;

g) $i-C_4H_{10}$ = 3.5%, $C_2F_4H_2$ = 96%, SF_6 = 0.5%.

In figure 5.9, the x-axis is the time (in nanoseconds) and the y-axis is the induced current obtained due to the movement of fast electrons as described earlier (in nano Amperes). The time integral of the induced current i.e., the area under the curve gives us information about the total charge which has resulted in the output pulse and the full width at half maximum (FWHM) of the pulse which is calculated as $FWHM = 2.355 \times \sigma$ (sigma is the standard deviation of the function used for fitting the signal pulse) gives us the required time resolution of the detector.

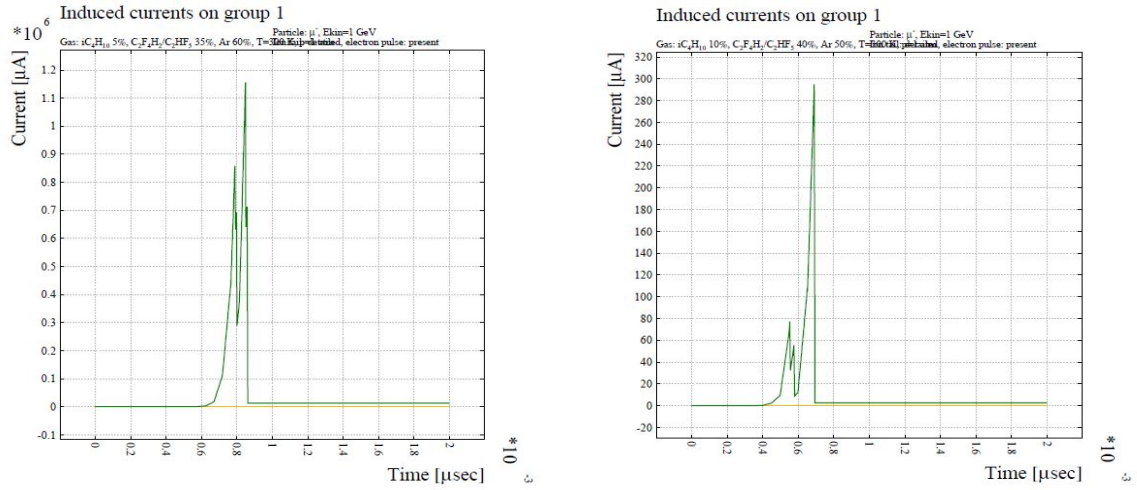

(a) (b)

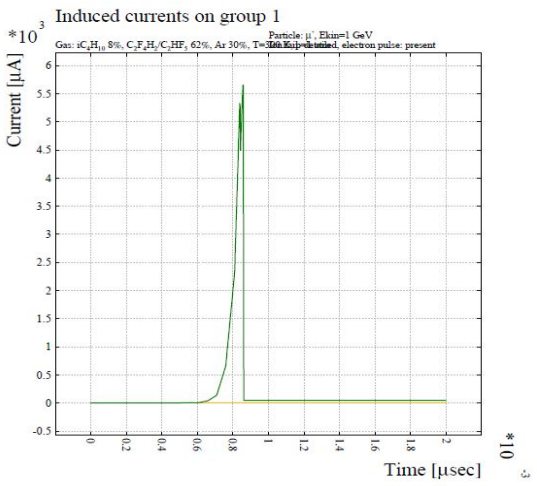

(c)

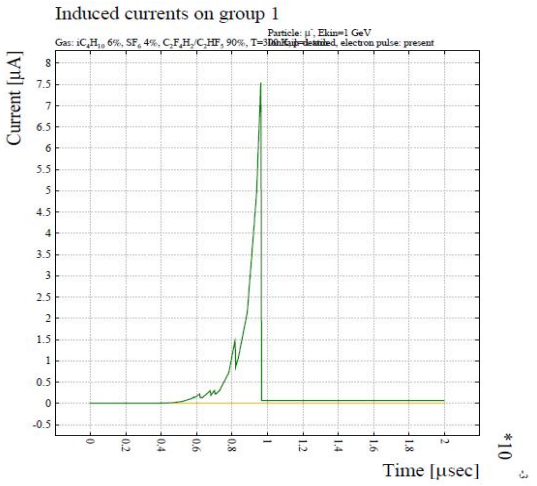

(d)

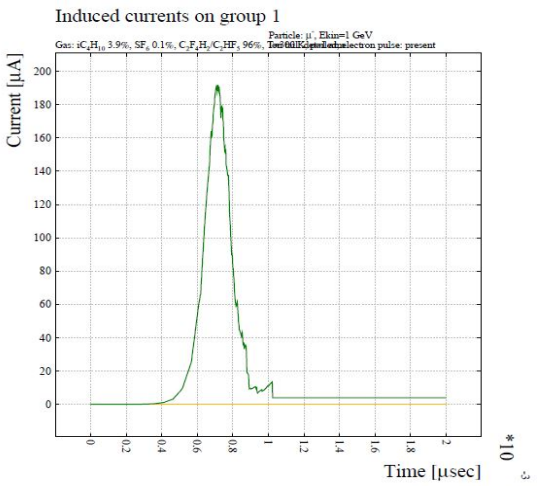

(e)

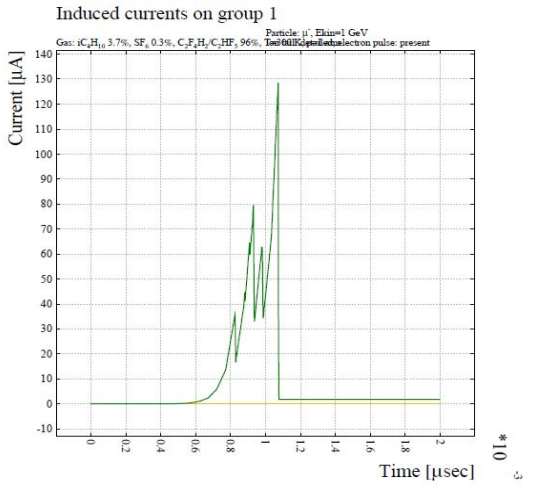

(f)

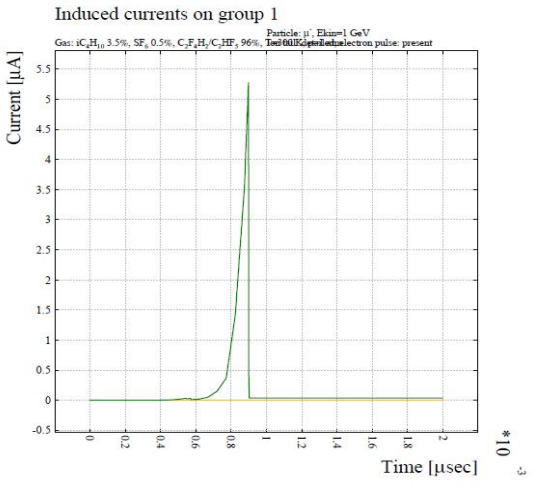

(g)

Figure 5.9: Signals obtained using Garfield-9 simulation package for the 5-gap RPC with 200 micron gas-gaps and the voltage across the conductive graphite electrodes is 12000 V. The signals are obtained for different gas-mixtures as already specified.

From the above results, we notice that the best time resolution is obtained for the gas mixture 3.5% $i-C_4H_{10}$, 96% $C_2F_4H_2$, 0.5% SF_6 (gas mixture-1) shown in figure 5.9 (g) which is around 55.6 picoseconds (ps) and for the gas mixture 6% $i-C_4H_{10}$, 90% $C_2F_4H_2$, 4% SF_6 (gas mixture-2) shown in figure 5.9 (d) which is around 60.1 ps. Now, we will take this two gas-mixtures and vary other two parameters to get the best possible time resolution for our detector.

Since from figure 5.9 (e and f), it can be observed that when 96% $C_2F_4H_2$ is used with different concentrations of SF_6 and $i-C_4H_{10}$ (other than 3.5% $i-C_4H_{10}$ and 0.5% SF_6), the time resolution deteriorates. We then tried to alter the gas mixture 3.5% $i-C_4H_{10}$, 96% $C_2F_4H_2$, 0.5% SF_6 by keeping the concentration of $C_2F_4H_2$ constant and changing the concentrations of SF_6 and $i-C_4H_{10}$ to check if we see any improvement in the time resolution. Following are the results for these simulations,

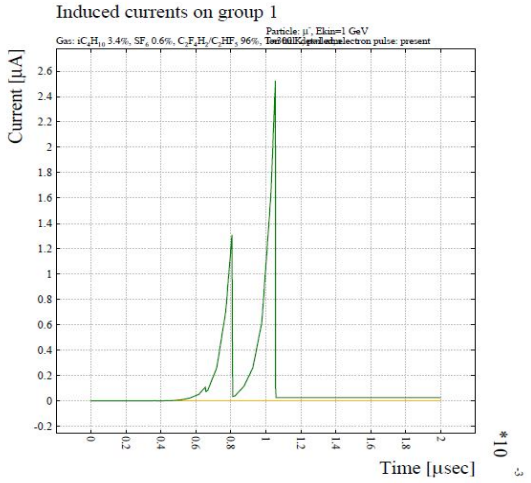

(a)

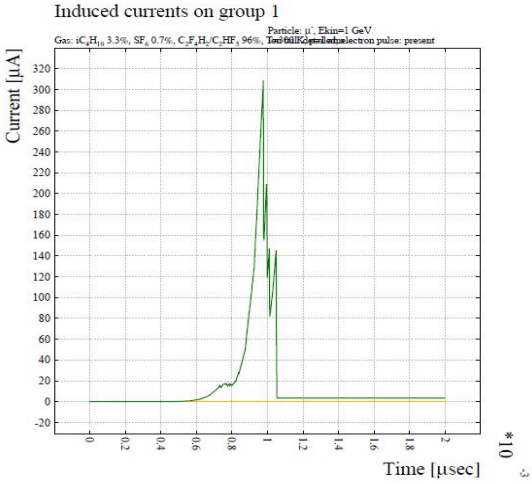

(b)

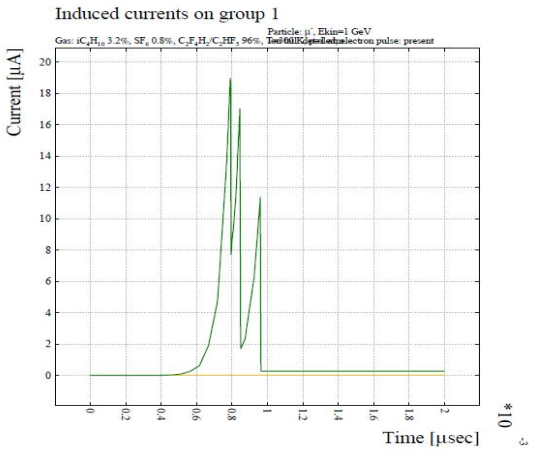

(c)

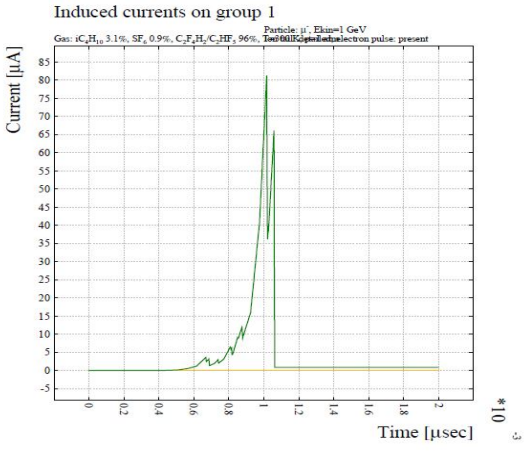

(d)

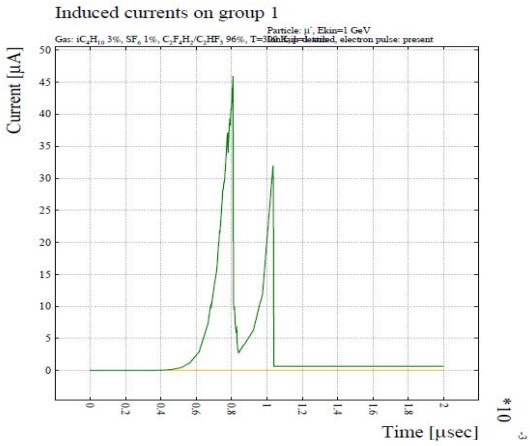

(e)

Figure 5.10: Signals obtained for 5-gap RPC with 200 micron gas-gaps and voltage across the conductive graphite electrodes being 12000 V. The signals are obtained for different concentration of SF_6, keeping the concentration of $C_2F_4H_2$ constant. Gas mixtures used are a) $i-C_4H_{10}$ = 3.4%, $C_2F_4H_2$ = 96%, SF_6 = 0.6%; b) $i-C_4H_{10}$ = 3.3%, $C_2F_4H_2$ = 96%, SF_6 = 0.7%; c) $i-C_4H_{10}$ = 3.2%, $C_2F_4H_2$ = 96%, SF_6 = 0.8%; d) $i-C_4H_{10}$ = 3.1%, $C_2F_4H_2$ = 96%, SF_6 = 0.9%; e) $i-C_4H_{10}$ = 3%, $C_2F_4H_2$ = 96%, SF_6 = 1%.

And surprisingly we observe that when the gas mixture 3.5% $i-C_4H_{10}$, 96% $C_2F_4H_2$, 0.5% SF_6 is altered (if the concentrations of SF_6 and $i-C_4H_{10}$ are changed from 3.5% $i-C_4H_{10}$ and 0.5% SF_6), the time resolution doesn't improve, rather it deteriorates and thus, we establish that the above-mentioned gas mixture suits best for this geometry as of now. We then changed another parameter i.e., voltage across the graphite electrodes (electric field in the gas-gaps) from 10 KV to 15 KV in steps of 1000 V keeping the gas mixture 3.5% $i-C_4H_{10}$, 96% $C_2F_4H_2$, 0.5% SF_6 and the geometry (as mentioned above) unchanged and performed the simulations, the results for which are given in figure 5.11.

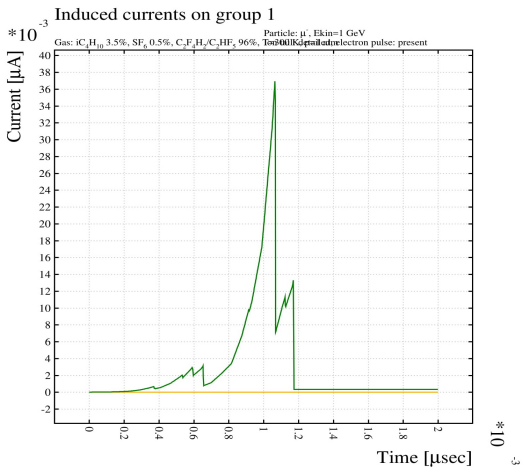

(a) 10 KV

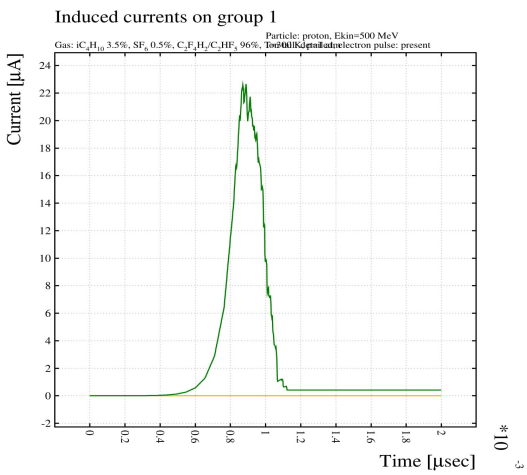

(b) 11 KV

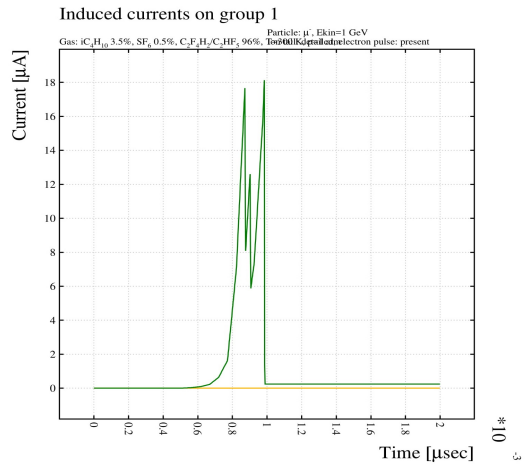

(c) 12 KV

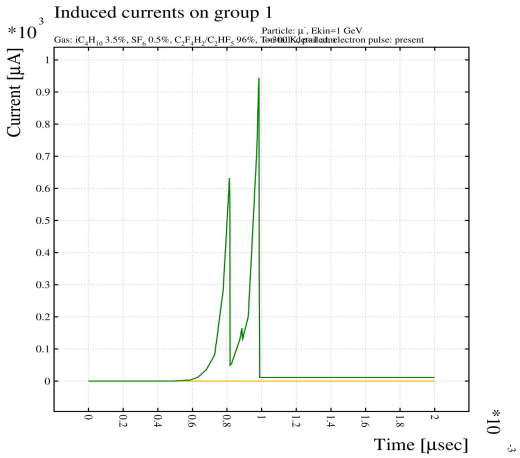

(d) 13 KV

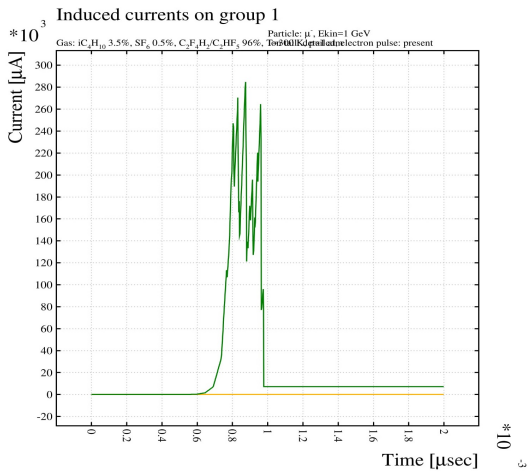

(e) 14 KV

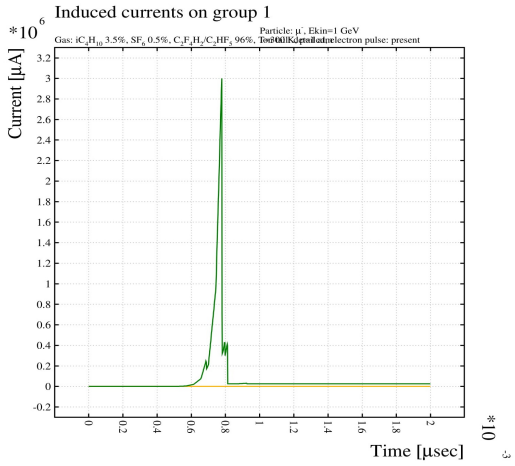

(f) 15 KV

Figure 5.11: Signals obtained for 5-gap RPC with 200 micron gas-gaps and gas-mixture 3.5% $i-C_4H_{10}$, 96% $C_2F_4H_2$, 0.5% SF_6. The voltage across the conductive graphite electrodes is changed from 10 KV to 15 KV in steps of 1 KV.

It is clear from the above results that for the 5-gap RPC with 200-micron gas-gaps and gas mixture 3.5% $i-C_4H_{10}$, 96% $C_2F_4H_2$, 0.5% SF_6, the best time resolution is obtained at 15000 V (figure 5.11 (f)) potential difference across the graphite electrodes (for which the electric field is 150 KV/cm in each gas-gap), the time resolution obtained is around 17.45 ps with the total charge being 124 pC.

We then used another gas mixture i.e., 6% $i-C_4H_{10}$, 90% $C_2F_4H_2$, 4% SF_6 with the same geometry (5-gap RPC with 200 micron gas-gaps) and varied the potential difference (ΔV) applied across the graphite electrodes from 10 KV to 15 KV in steps of 1 KV and the results for these simulations are shown in figure 5.12,

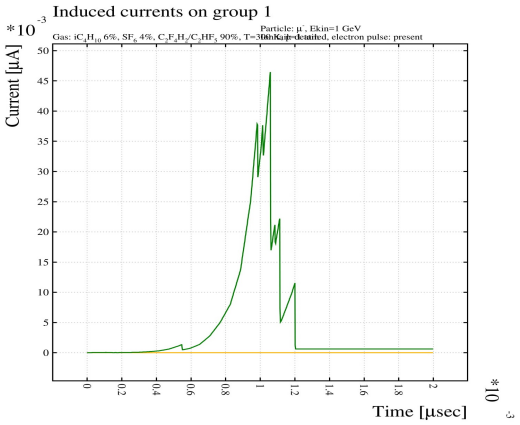

(a) 10 KV

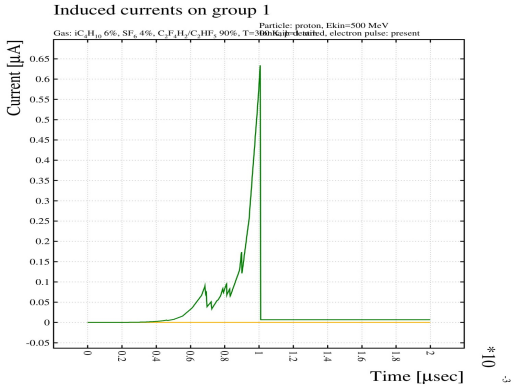

(b) 11 KV

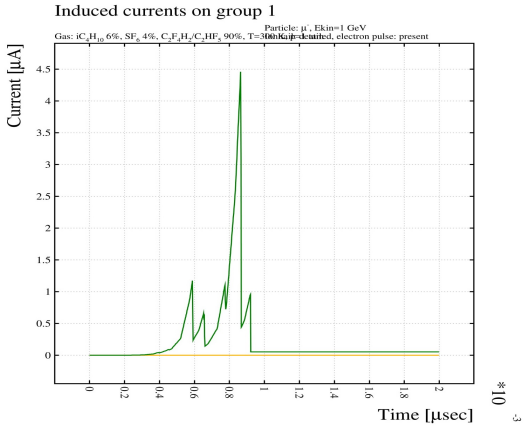

(c) 12 KV

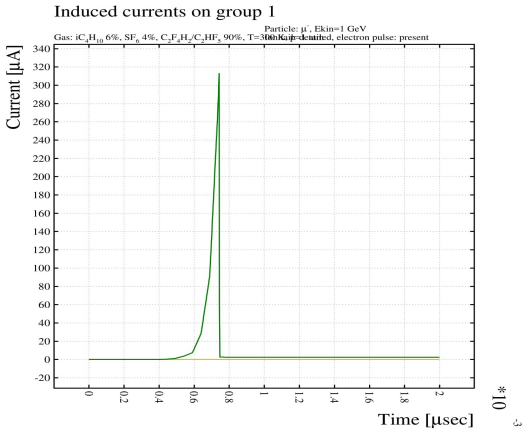

(d) 13 KV

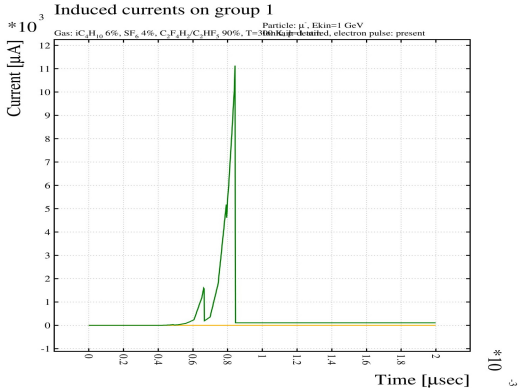

(e) 14 KV

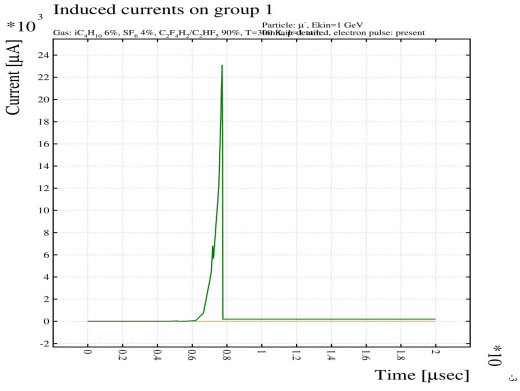

(f) 15 KV

Figure 5.12: Signals obtained for 5-gap RPC with 200 micron gas-gaps and gas-mixture 6% $i-C_4H_{10}$, 90% $C_2F_4H_2$, 4% SF_6. The voltage across the conductive graphite electrodes is changed from 10 KV to 15 KV in steps of 1 KV.

Thus, for the gas mixture 6% $i-C_4H_{10}$, 90% $C_2F_4H_2$, 4% SF_6, the best time resolutions are obtained for the potential difference 13000 V, 14000 V and 15000 V as can be seen from figure 5.12 (d, e, f). Following table shows the obtained time resolutions.

ΔV (V)	Time Resolution (ps)	Total Accumulated Charge (pC)
13000	23.71	0.016
14000	30.71	0.7
15000	18.83	0.91

5.4 Simulation of 5-Gap RPC with 250 micron gas-gaps

Till now we have altered two parameters i.e., gas-mixture and voltage to get the best possible time resolution for the 5-gap RPC with 200-micron gas-gaps. Now, we change the geometry to see if we see any improvement in the time resolution. We have created yet another geometry consisting of 5 gas-gaps with the thickness of each gap being 250 microns as against 200 microns in the previous geometry, with the dimensions of rest of the electrodes being unchanged. An important point to note is that for the smaller gas gap, due to the higher electric field, the Townsend coefficient is higher which instead results in higher gas-gain, but the avalanche has a smaller distance to travel which results in the lower gain. Whereas for larger gas gaps, due to lower electric fields, the Townsend coefficient decreases which instead results in lower gas-gain, but the avalanche has a larger distance to travel which results in an increased gas-gain. This interplay between the smaller and larger gas-gaps needs to be optimized along with the gas-mixture and applied electric field to obtain the best possible time resolution. Thus by increasing the width of the gas-gaps from 200 microns to 250 microns, we are increasing the gas-gain (since the avalanche has larger distance to travel) making sure that the electric field for the corresponding gas-gaps is same in 250 microns MRPC as that in the 200 micron MRPC by adjusting the voltage across the graphite electrodes appropriately (for example, the electric field in 200-micron gas-gaps MRPC at 12000 V potential across the graphite electrodes is same for 250-micron gas-gaps MRPC at 15000 V potential difference). We have used two gas mixtures 3.5% $i-C_4H_{10}$, 96% $C_2F_4H_2$, 0.5% SF_6 and 6% $i-C_4H_{10}$, 90% $C_2F_4H_2$, 4% SF_6 and varied the voltage that is applied on the conductive graphite electrodes from 10 KV to 17 KV. Figure 5.13 shows the results of the simulations with gas mixture-1 i.e., 3.5% $i-C_4H_{10}$, 96% $C_2F_4H_2$, 0.5% SF_6.

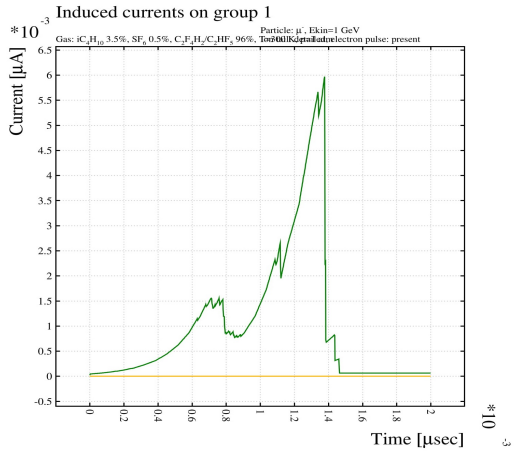

(a) 10 KV

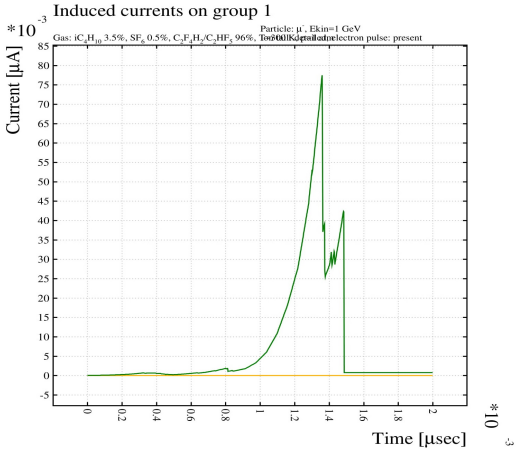

(b) 11 KV

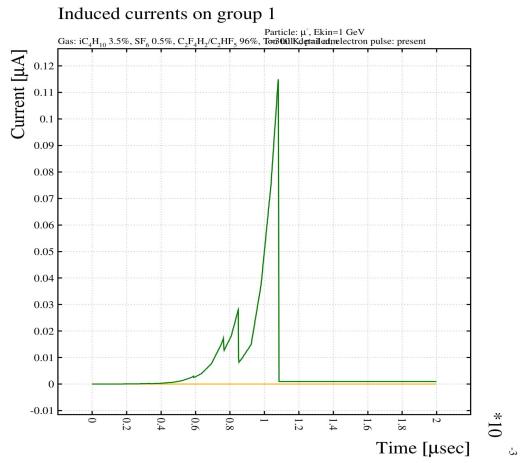

(c) 12 KV

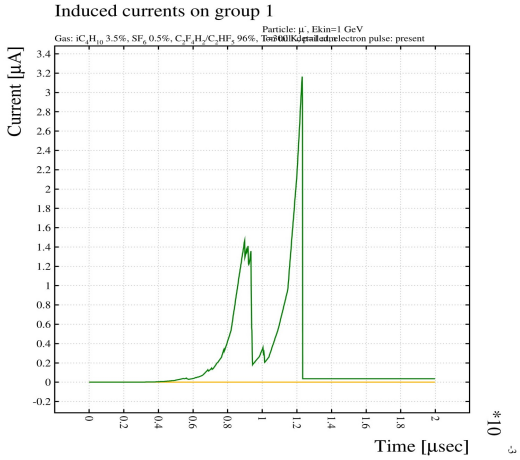

(d) 13 KV

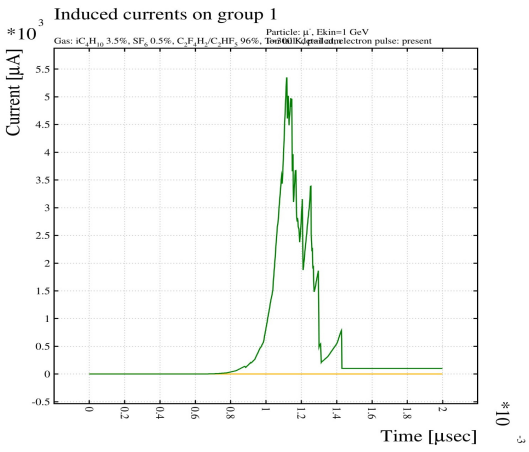

(e) 14 KV

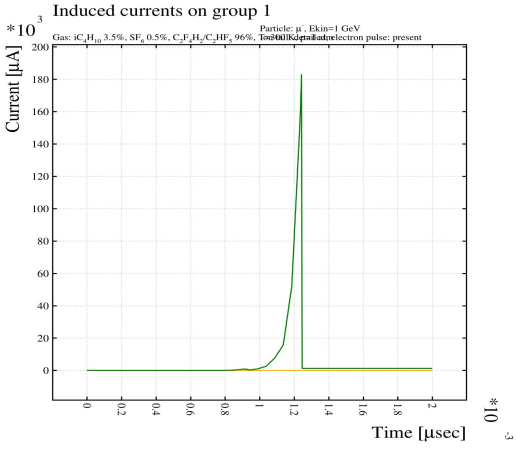

(f) 15 KV

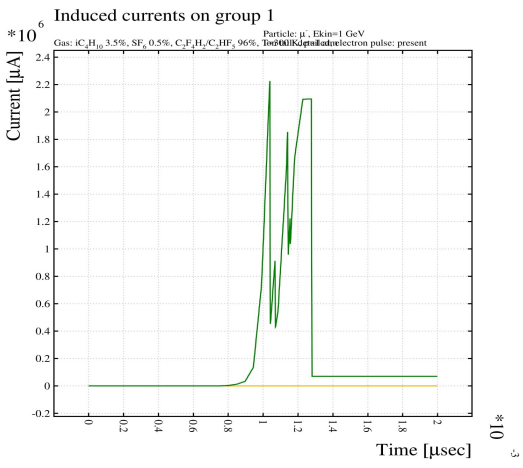

(g) 16 KV

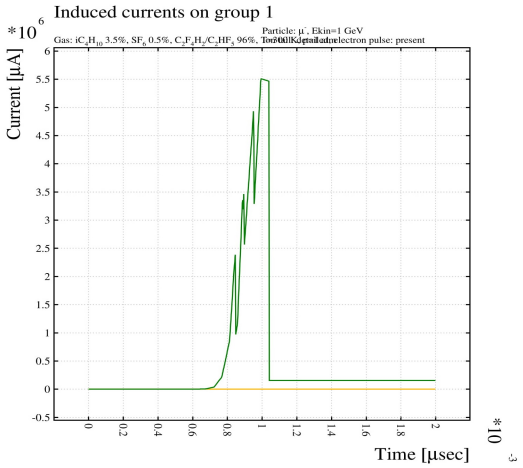

(h) 17 KV

Figure 5.13: Signals obtained for 5-gap RPC with 250 micron gas-gaps and gas-mixture 3.5% $i-C_4H_{10}$, 96% $C_2F_4H_2$, 0.5% SF_6. The voltage across the conductive graphite electrodes is changed from 10 KV to 17 KV in steps of 1 KV.

From the above results, we can see that the best time resolution is obtained when the voltage across the graphite electrodes is 15000 V for the 5-gap RPC with 250 micron gas-gaps and gas mixture 3.5% $i-C_4H_{10}$, 96% $C_2F_4H_2$, 0.5% SF_6 as shown in figure 5.13 (f). The time resolution is around 25.39 ps and the total charge accumulated is around 9.69 pC.

For the same geometry (5-gap RPC with 250 micron gas-gaps), we have used another gas mixture i.e., 6% $i-C_4H_{10}$, 90% $C_2F_4H_2$, 4% SF_6 and simulated the MRPC with different potentials from 10 KV to 17 KV applied across the graphite electrodes. The results of these simulations are shown in figure 5.14.

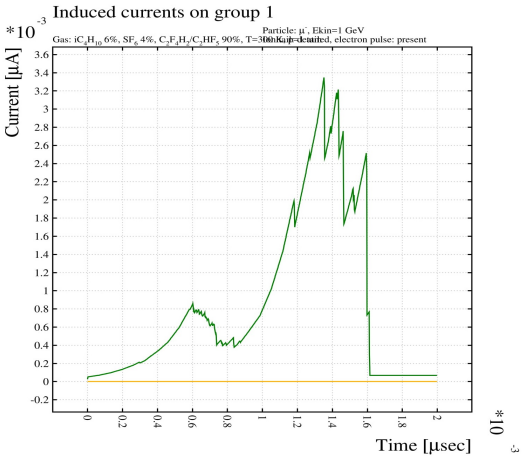

(a) 10 KV

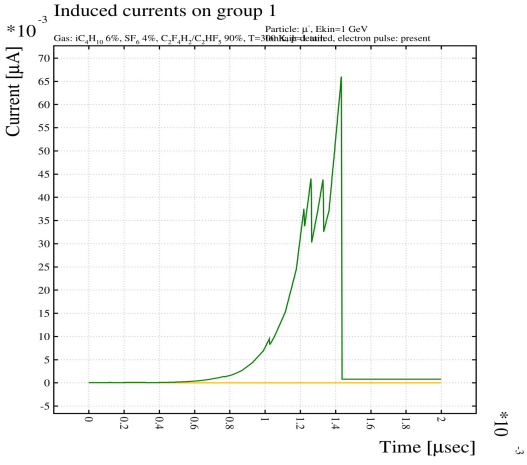

(b) 11 KV

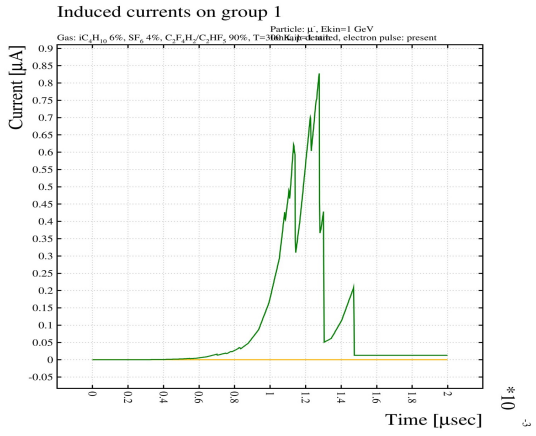

(c) 12 KV

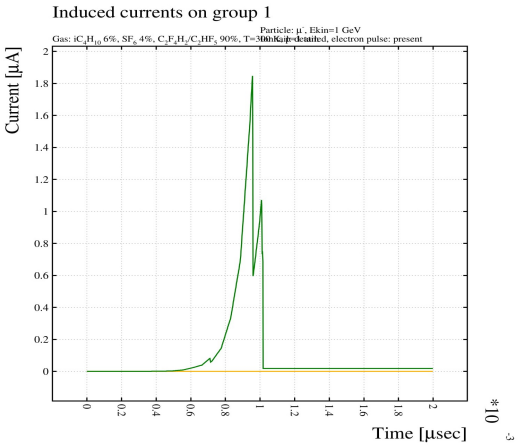

(d) 13 KV

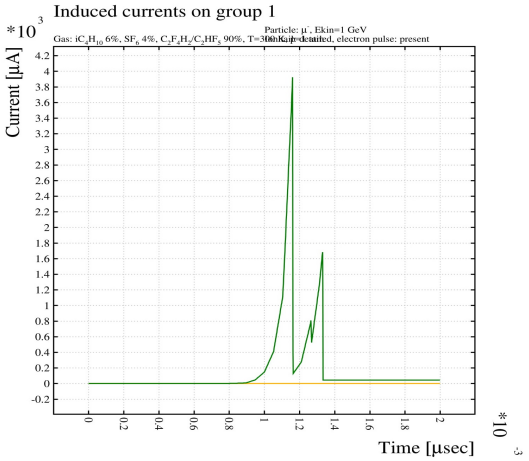

(e) 14 KV

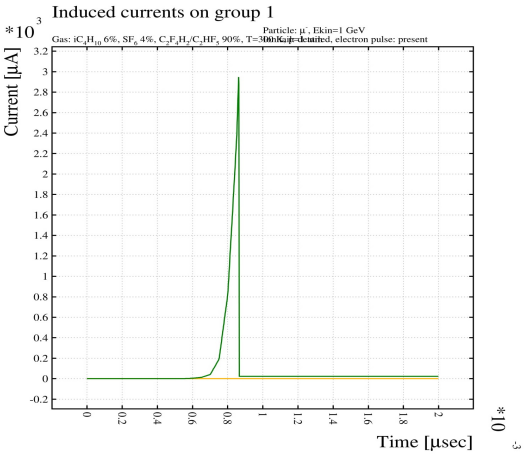

(f) 15 KV

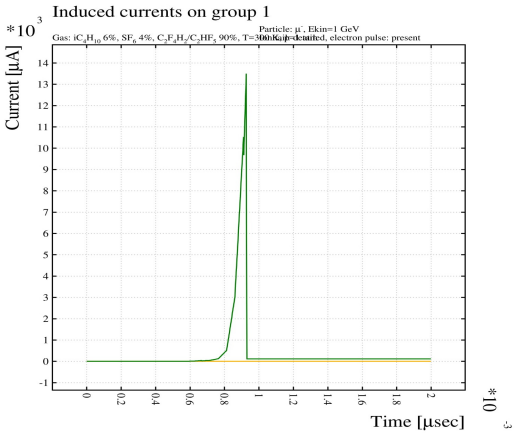

(g) 16 KV

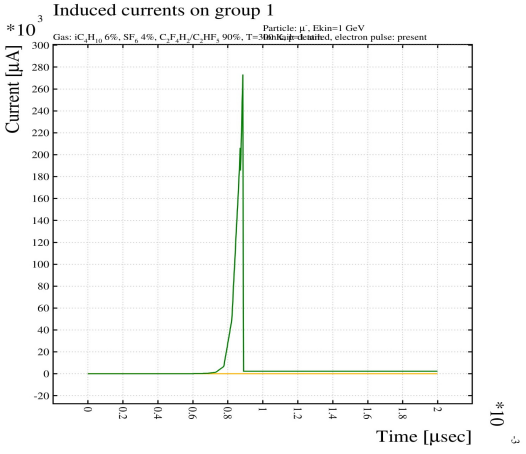

(h) 17 KV

Figure 5.14: Signals obtained for 5-gap RPC with 250 micron gas-gaps and gas-mixture 3.5% $i-C_4H_{10}$, 96% $C_2F_4H_2$, 0.5% SF_6. The voltage across the conductive graphite electrodes is changed from 10 KV to 17 KV in steps of 1 KV.

From figure 5.14 (f, g, h) we can see that the best time resolutions are obtained for the potentials 15000 V, 16000 V, and 17000 V across the conductive graphite electrodes. The obtained time resolutions are given in the following table.

ΔV (V)	Time Resolution (ps)	Total Accumulated Charge (pC)
15000	25.69	0.154
16000	25.15	0.671
17000	22.27	11.89

Following Chapter briefly summarizes the work done as part of this thesis and the results obtained for the optimization of 5-gap RPC detector.

Chapter 6

Results and Conclusion

With our main aim to optimize the 5-gap RPC to obtain the best possible time resolution, we have simulated the desired MRPC geometry using Garfield simulation package which is interfaced with other packages such as Magboltz and Heed. As we have mentioned in the previous Chapter that we have considered three optimization parameters i.e., the gas mixture, the potential across the conductive graphite electrodes (or electric field in each gas-gap) and the geometry (width of the gas-gaps). For optimizing the 5-gap Resistive Plate Chamber (RPC), we started with a geometry consisting of 5 gas-gaps each of thickness 200 microns. Fixing this geometry and the potential across the conductive graphite electrodes, we used several gas-mixtures as mentioned in the previous Chapter to arrive at the best possible gas mixtures which can give us the desired time resolution (i.e., in 10's of picoseconds). We came up with two such gas-mixtures which are gas mixture-1 (3.5% $i-C_4H_{10}$, 96% $C_2F_4H_2$, 0.5% SF_6) and gas-mixture-2 (6% $i-C_4H_{10}$, 90% $C_2F_4H_2$, 4% SF_6). We then simulated the 5-gap RPC using these two gas mixtures by changing the voltage applied across the conductive graphite electrodes from 10 KV to 15 KV in steps of 1 KV (changing the voltage essentially changes the electric field in each gap thereby affecting the gas-gain as well as the time resolution). We then altered the detector geometry by changing the thickness of the gas-gaps from 200 microns to 250 microns (increasing the thickness of the gas-gaps increases the volume for ionization thereby increasing the gain as well as affecting the time resolution of the detector). Then changing the geometry from 5-gap RPC with 200 micron gas-gaps to 250 micron gas-gaps (by 250 micron gas-gaps we mean the thickness of each gas gap is 250 microns), we again used the two gas-mixtures and different voltages to arrive at the best possible time resolutions. The time resolutions (in picoseconds) obtained from the simulation of two different detector geometries (one with 200 microns wide gas-gaps and other with 250 microns wide gas-gaps) for two gas mixtures and different voltages across the conductive graphite electrodes (ΔV) are given in

$\Delta V(V)$	**Gas mixture-1**		**Gas mixture-2**	
	200 μm gas-gap	**250 μm gas-gap**	**200 μm gas-gap**	**250 μm gas-gap**
13000	–	–	23.71 ps	–
14000	–	–	30.71 ps	–
15000	17.45 ps	25.39 ps	18.83 ps	25.69 ps
16000	–	–	–	25.15 ps
17000	–	–	–	22.27 ps

Table 6.1: Time resolutions obtained for simulations with two different gas mixtures and detector geometries by varying the applied voltage across the conductive graphite electrodes. Dashed lines indicate that the signals obtained don't have the time resolution in few 10's of picoseconds or the output pulse is not well defined.

the following table.

Consider the gas mixture-1 (3.5% $i-C_4H_{10}$, 96% $C_2F_4H_2$, 0.5% SF_6), the best time resolution is obtained for the 5-gap RPC with 200 micron gas-gaps at 15000 V potential applied across the conductive graphite electrodes, which comes out to be around 17.45 picoseconds (ps). From figures 5.11 (f) and 5.13 (f) we can see that for 200 micron gas-gaps at 15000 V potential across the graphite electrodes, the amplitude of the signal pulse is around 3 A and for 250 micron gas-gaps at the same applied potential, the amplitude of the signal pulse is around 182 mA. This difference in amplitudes arises because when 15000 V is applied across the graphite electrodes then for 200 micron gas-gaps, the electric field in each gap is 150 KV/cm and for 250 micron gas-gaps, the electric field in each gap is 120 KV/cm (increase in the electric field in gas-gaps increases the gas gain). Thus, the signal obtained from the 5-gap RPC with 200 micron gas-gaps at 15000 V potential across the graphite electrodes using the gas mixture 3.5% $i-C_4H_{10}$, 96% $C_2F_4H_2$, 0.5% SF_6 has an improved time resolution (17.45 ps) and it also does not require sophisticated electronics for signal collection as the output signal is large enough (amplitude of the pulse being around 3 A) for measurement.

Using the gas mixture-2 (6% $i-C_4H_{10}$, 90% $C_2F_4H_2$, 4% SF_6), the best time resolution is obtained for the detector geometry consisting of 200 microns wide gas-gaps at 15000 V potential applied across the conductive graphite electrodes which comes out to be around 18.83 ps. From figures 5.12 (f) and 5.14 (f) it is again clear that the when 15000 V is applied

across the graphite electrodes, the amplitude for 200 micron gas-gaps (which is around 23 mA) is more than that of 250 micron gas-gaps (which is around 2.9 mA) because of the same argument as given in the above paragraph.

If we compare the amplitudes for the two gas mixtures at 15000 V potential across the graphite electrodes and 5-gap RPC geometry with 200 micron gas-gaps, the amplitude of the output signal for the second gas mixture is relatively lower because the second gas mixture uses 4% SF_6 (SF_6 is an electron quencher and hence it effectively decreases the amplitude of the output signal which depends upon on the number of fast electrons produced in the avalanche).

Thus, we conclude that in order to obtain the best possible time resolution for the 5-gap RPC, the best-optimized gas mixture is 3.5% $i-C_4H_{10}$, 96% $C_2F_4H_2$, 0.5% SF_6 with the best-optimized geometry being the one with the thickness of each gas-gap being 200 microns and the best optimized high voltage to be applied across the conductive graphite electrodes is 15 KV. We have obtained the best possible time resolution as 17.45 ps for the said geometry and potential. The gas mixture 6% $i-C_4H_{10}$, 90% $C_2F_4H_2$, 4% SF_6 allows the operation of MRPC detector at different high voltages across the conductive graphite electrodes as can be inferred from the above table (for the gas mixture-2, we are able to get time resolution better than 50 ps for three different voltages both for the case of 200 microns gas-gaps as well as for 250 microns gas-gaps), hence, this gas mixture is also a good candidate to get the best possible time resolution (which is quite evident from the fact that the best time resolution using the gas mixture-2 is obtained as 18.83 ps which is not very different from 17.45 ps as obtained for the gas mixture-1).

Possible future endeavors include optimizing the 5-gap RPC geometry as described in this work to get the best possible time resolution using a Freon-free gas mixture to avoid any harm to the environment by the use of greenhouse gas mixtures in a large number of detectors. We will also make a prototype of the 5-gap RPC in our lab at Indian Institute of Science Education and Research and will explore further uses of MRPCs in different application through experimentation.

Appendix A

Cross sections of different gases used by Magboltz 7.1

As already mentioned in Chapter-4 that the *Magboltz* program calculates electron transport properties in gases such as the drift velocity, the Townsend and attachment coefficients, the longitudinal and diffusion coefficients etc. by numerically integrating the Boltzmann transport equations for the electrons in gas mixtures with applied electric and magnetic field at arbitrary angles. In order to calculate electron transport properties like the drift velocity, Magboltz takes into account microscopic parameters such as the scattering cross sections (the measure of how likely the collisions occur), the energy loss per collision etc. of each gas used in the detector. It uses Monte Carlo integration method (traces electrons microscopically through numerous collisions with the gas molecules) to calculate various electron transport properties in gas mixtures. Cross-sections for various gases are given in figure A.1.

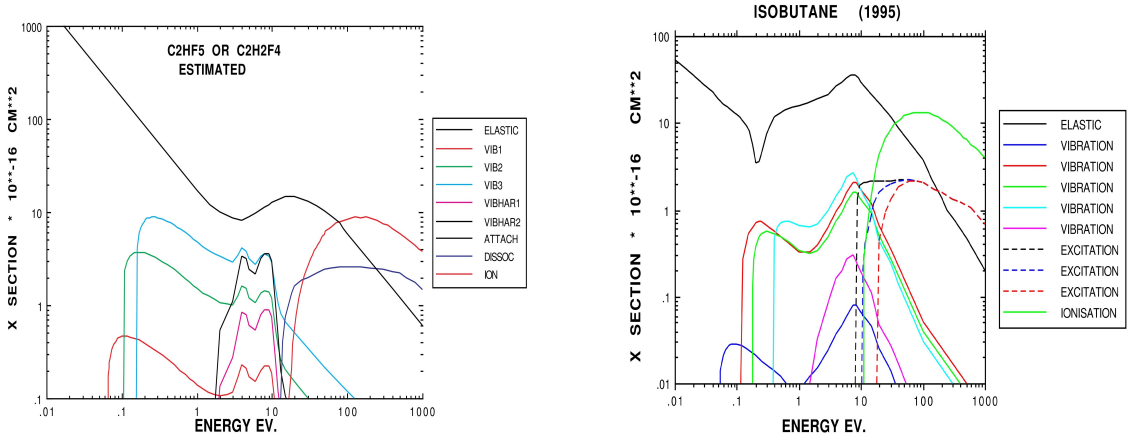

(a) $C_2F_4H_2$ (b) i-C_4H_{10}

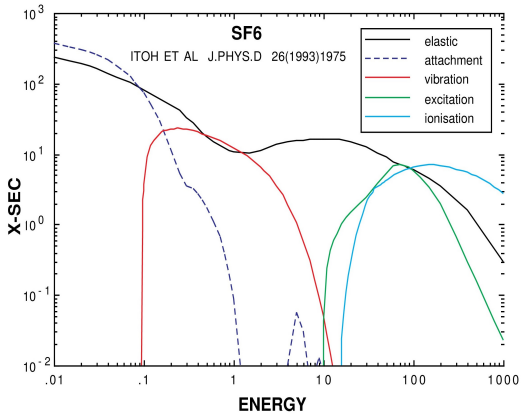

(c) SF_6

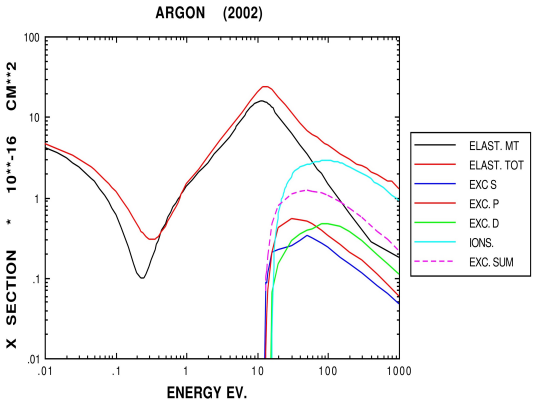

(d) Ar

Figure A.1: Cross sections of a) 1,1,2,2-Tetrafluoroethane ($C_2F_4H_2$), b) iso-butane ($i-C_4H_{10}$), c) sulfur hexafluoride (SF_6), d) argon (Ar) and d) ethane (C_2H_6) used by Magboltz 7.1. Y-axis is the cross section in cm^2 and X-axis is energy in eV [Biac].

Appendix B

Applications of Multigap Resistive Plate Chamber (MRPC)

B.1 As a Time of Flight (TOF) Detector in the ALICE Experiment

Particle identification (PID) from Pb-Pb collisions is an important aspect of the ALICE experiment at the Large Hadron Collider (LHC). Time of Flight (TOF) detector system is among the important detectors used for charged hadron identification in the central barrel of the ALICE experiment. The TOF system covers a cylindrical surface of $141 m^2$ having an inner radius of 3.7m (figure B.1) and polar acceptance of $|\theta - 90^o| < 45^o$ with fully covering the azimuthal angle. It provides PID of π (pion), K (kaon) and p (proton) in the central rapidity region with momentum of the particle $p > 0.5$ GeV/c up to a few GeV/c [06a]. In order to achieve the physics goals, the time of flight (TOF) detector needs to satisfy the requirements such as high efficiency (> 95%), rate capability as per the ALICE experiment ($\leq 50 Hz/\text{cm}^2$), time resolution better than 100 ps, simplicity and low manufacturing cost for segmentation and use in large numbers.

The gaseous detector is an ideal choice for such a detector and among the gaseous detectors, Multigap Resistive Plate Chamber (MRPC) has been identified to satisfy all the mentioned criteria for the TOF system of the ALICE experiment. As we have seen that MRPC has a time resolution of better than 100 ps with much-improved rate capability and ease of manufacturing which makes it an ideal candidate to be used in the TOF system.

Time of Flight detectors measure the time difference between the arrival of particles at two detectors. If L is the distance between TOF counters, then the time of flight difference between two particles with masses m_1 and m_2 and energies E_1 and E_2 with their velocities

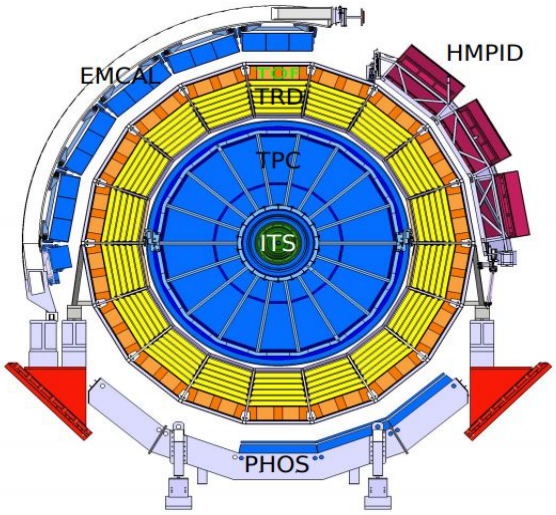

(a) Cross-section of the ALICE detector system. TOF system is above the Transition Radiation Detector (TRD).

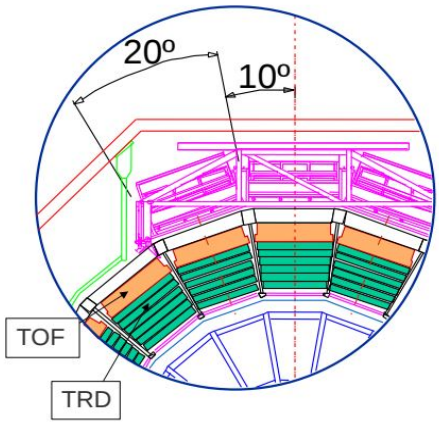

(b) Arrangement of TOF system as a barrel with radius 3.7 m.

Figure B.1: TOF detector system at ALICE experiment.

being v_1 and v_2 is given by [Sta],

$$\Delta t = \tau_1 - \tau_2 = \frac{L}{c}\left(\frac{1}{\beta_1} - \frac{1}{\beta_2}\right)$$

$$\Delta t = \frac{L}{c}\left(\sqrt{\frac{1}{1-(m_1c^2/E_1)^2}} - \sqrt{\frac{1}{1-(m_2c^2/E_2)^2}}\right)$$

In the relativistic limit where, $E \simeq pc \gg m_i c^2$ (i.e., assuming the same momentum $p_1 = p_2 = p$ and the same energy $E_1 = E_2 = E$ for two particles), the time of flight difference is given by,

$$\Delta t = \frac{Lc}{2p^2}(m_1^2 - m_2^2)$$

As we can see that the faster a detector records the arrival time of an incoming particle, the more precisely the particle identification process can be performed. Thus, a detector with an excellent time resolution as well as high rate capability is desirable and what could be better than the MRPC detector which in addition to having a time resolution of better than 100 ps, has much lower manufacturing cost thereby allowing its use in large numbers.

B.2 In Homeland Security

Multigap Resistive Plate Chamber (MRPC) is also being used an active detector in *Muon Scattering Tomography (MST)* which is a novel technique for identifying higher atomic number (Z) materials. Cosmic-ray Muon Scattering Tomography uses cosmic-ray muons to generate three-dimensional images of objects using information from the muons scattered from these objects due to Coulomb scattering. The basic principle of MST is the *multiple Coulomb scattering* in which the muons are decelerated and deflected upon encountering a material with high atomic number (Z) solely due to the Coulomb force (negatively charged muons are deflected by negatively charged electrons present in the material) as shown in figure B.2. Information about the density of a material can be collected by carefully analyzing the angles of deflection of the muons before and after passing through the material. Since X-rays cannot penetrate deep inside a material with a larger atomic number, they are generally not useful for the identification of such materials. Muons, on the other hand, can penetrate deep through the materials and hence can be conveniently used for identifying high-Z materials. Muon Scattering Tomography can be efficiently used for identifying any threat materials (nuclear materials which can be used for destructive purposes) which are generally shielded using highly dense materials such as lead. This instead prevents any smuggling of the nuclear materials across borders.

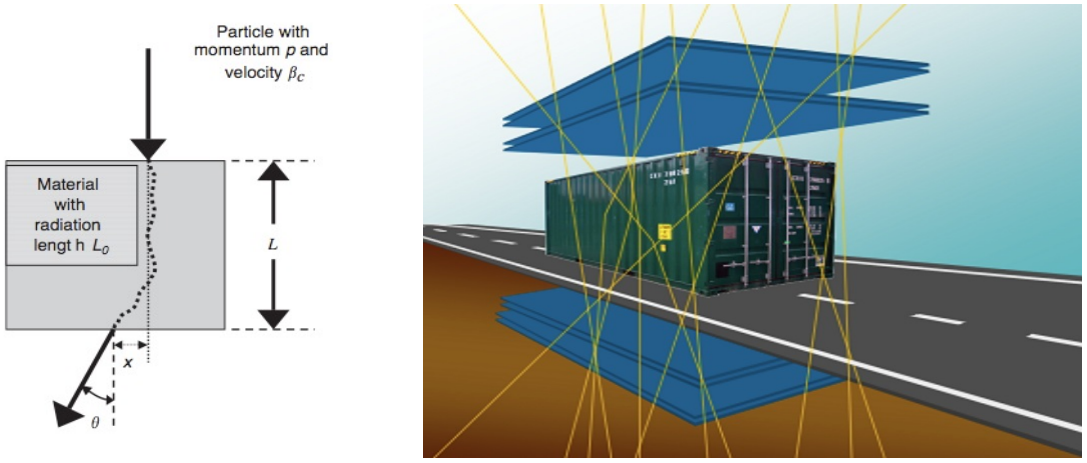

(a) Schematic of Multiple Coulomb Scattering (MCS) of a charged particle passing through a material.

(b) Application of Muon Scattering Tomography for identifying high-Z materials at ports and borders as an efficient technology for homeland security.

Figure B.2: Multiple Coulomb Scattering of a charged particle and application of Muon Scattering Tomography in homeland security.

Apart from the application in homeland security, MST is also used in industries for precision measurement of the material composition and building stability. It is also used for

controlling trucks at the gates of steel foundries. It can also be used for geological surveys (determining the depth of volcanos, mines etc.)

B.3 In Medical Imaging

Positron Emission Tomography (PET) is a nuclear imaging technique which provides metabolic information of the body thereby helping in the diagnosis of various physiological diseases. In PET, a positron-emitting radionuclide is introduced into the body for labeling metabolically active compounds. In this process, positrons with energies of the order of 1 MeV are emitted and they have a short range of about 1-2 mm in human tissue [Nec]. An emitted positron after losing most of its energy through collisions with the surrounding molecules forms a short-lived particle called *positronium* by combining with an electron as shown in figure B.3. Positronium undergoes an annihilation within around 10^{-10} s and produces two photons each of energy close to 511 KeV in an exactly opposite direction (to conserve momentum). Simultaneous detection of these photons can be used to trace the position of the positron annihilation which instead can be used to track the metabolic processes in the body. PET is based on this process of simultaneous detection of the two gamma rays each of energy 511 KeV. These two 511 KeV photons are detected by two detectors placed in opposite direction and an event (positron decay) is registered using a narrow time window of around 15 ns.

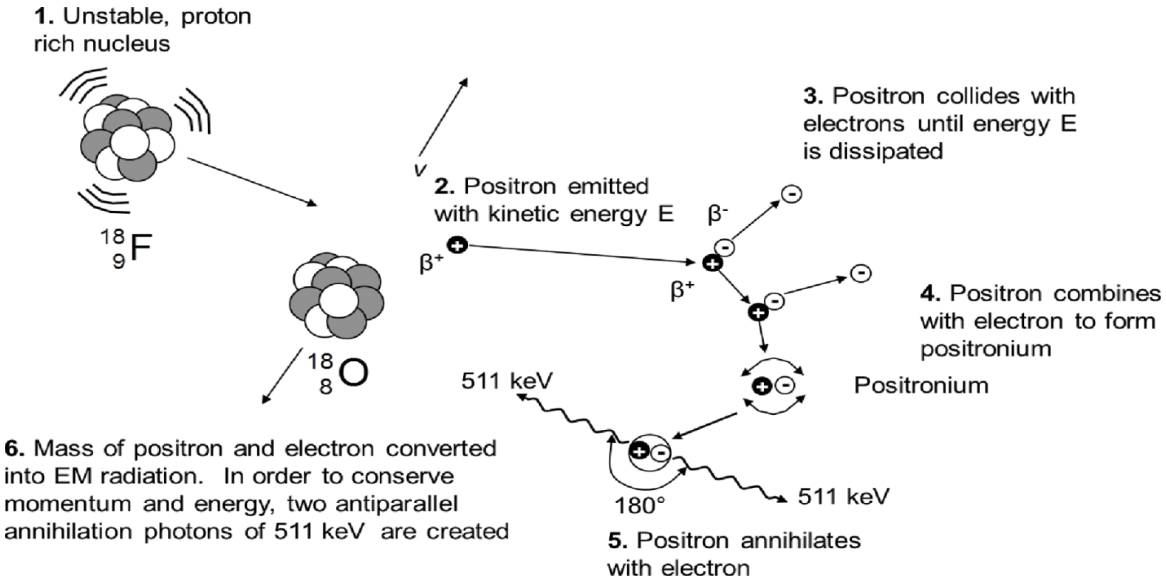

Figure B.3: Schematic diagram of the positron emission and annihilation process involved in the working of Positron Emission Tomography.

The first positron medical imaging technique was developed by Brownell and Sweet at Massachusetts General Hospital back in 1951. Scintillation detectors coupled to photo-multiplier tubes are commonly used in Positron Emission Tomography due to their good energy resolution and stopping efficiency. Figure B.4 shows the properties of commonly used scintillators in Positron Emission Tomography.

Property	NaI(Tl)	BGO	LSO	YSO	GSO	BaF_2
Density (g/cm^3)	3.67	7.13	7.4	4.53	6.71	4.89
Effective Z	50.6	74.2	65.5	34.2	58.6	52.2
Decay constant (ns)	230	300	40	70	60	0.6
Light output (photons/keV)	38	6	29	46	10	2
Relative light output	100%	15%	75%	118%	25%	5%
Wavelength λ (nm)	410	480	420	420	440	220
Intrinsic $\Delta E/E$ (%)	5.8	3.1	9.1	7.5	4.6	4.3
$\Delta E/E$ (%)	6.6	10.2	10	12.5	8.5	11.4
Index of refraction	1.85	2.15	1.82	1.8	1.91	1.56
Hygroscopic?	Yes	No	No	No	No	No
Rugged?	No	Yes	Yes	Yes	No	Yes
μ (cm^{-1})	0.3411	0.9496	0.8658	0.3875	0.6978	0.4545

Figure B.4: Properties of commonly used scintillators in PET. The energy resolution and attenuation coefficient (μ) are measured at an energy of 511 KeV [Nec].

The use of scintillation detectors in PET has some limitations such as the measurement of a large number of random counts due to the large coincidence time window and the inaccurate measurement of the arrival time of photons, short field of view, poor image quality, poor measurement of attenuation by different tissues and the cost of using scintillation detectors is also relatively more [06b]. The difference in the arrival time of the two photons which has to be measured using detectors with excellent time resolution can also provide an estimate of the annihilation point. This process of estimating the arrival times of the two photons is known *Time of Flight measurement*. This process results in the improved signal to noise ratio in the acquired image. The Multigap Resistive Plate Chamber, which as we have already seen has a very good time resolution (better than 100 ps), is found to be an excellent candidate to be used as a time of flight detector in PET. MRPC also offers other advantages such as high spatial resolution and high detector sensitivity which is why it is more preferred to be used as active detectors in PET. MRPCs can also be implemented in larger areas due to their ease of manufacturing and effective cost, thereby increasing the field of view as well as the counting rate. Since photons are not directly detected in MRPCs, the incident 511 KeV photons produce electrons by a Compton or photoelectric interaction at the electrodes of the MRPC and these electrons are then detected and traced back to get information about the incoming photons. PET imaging technique can be used to examine brain functions and cancerous tissues. Figure B.5 shows a PET image of tumor-bearing mice injected with 18F-ICMT-11 radiotracer used for anticancer therapy.

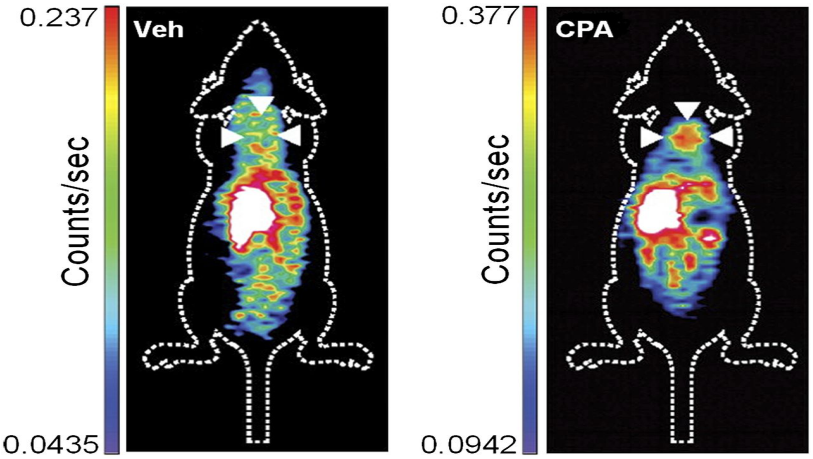

Figure B.5: [^{18}F]ICMT-11 coronal PET images of tumor-bearing mice. on left is the non-treated case and on right is the treated one with cyclophosphamide (CPA). White arrow-heads indicate the tumors [NQE09].

Bibliography

[AC80] W. W. M. Allison and J. H. Cobb, *Monte carlo calculation of electron transport coefficients in counting gas mixtures i. argon-methane mixturess*, Annu. Rev. Nucl. Part. Sci. **30** (1980).

[Bae] Paolo G. Baesso, Feasibility study and preliminary results of a Positron Emission Tomograph prototype based on Resistive Plate Counters, Page 50.

[Biaa] S. Biagi, Imonte, program to compute gas properties, Version 4.5.

[Biab] Stephen Biagi, Cross sections used by Magboltz 7.1, `http://rjd.web.cern.ch/rjd/cgi-bin/cross`.

[Biac] ———, Cross sections used by Magboltz 7.1, `http://rjd.web.cern.ch/rjd/cgi-bin/cross`.

[Bin12] M. Bindi, *Operation and performance tuning of atlas rpcs through the detector control system at the startup of 2009 lhc run*, Nucl. Instr. and Meth. **A661 Suppl. 1** (2012), no. S10.

[Cam09] P. Camarri, *Operation and performance of rpcs in the argo-ybj experiment*, Nucl. Instr. and Meth. **A 414** (2009), no. 317.

[Col17] The ICAL Collaboration, *Physics potential of the ical detector at the india-based neutrino observatory (ino)*, Pramana-J Phys (2017).

[DGD16] J. Gonzalez Huangshan Chen D. Gonzalez-Díaz, F. R. Palomo, *Detectors and concepts for sub-100 ps timing with gaseous detectors*, arXiv:1606.08172v2 (2016).

[ECZ96] D. Hatzifotiadou J. Lamas Valverdea R.J. Veenhof M.C.S. Williams A. Zichichi E. Cerron Zeballos, I. Crotty, *Avalanche fluctuations within the multigap resistive plate chamber*, Nucl. Instr. and Meth. **A 381** (1996), no. 512.

[ED05] G.T. Ewan and W.F. Davidson, *Early development of the underground sno laboratory in canada*, PHYSICS IN CANADA (2005).

[Fer09] F. Ferroni, *The second generation babar rpcs: final evaluation of performances*, Nucl. Instr. and Meth. **A602** (2009), no. 649.

[Gai90] Thomas K. Gaisser, *Cosmic rays and particle physics*, Cambridge University Press, 1990.

[GF86] E. MATHIESON G.W. FRASER, *Monte carlo calculation of electron transport coefficients in counting gas mixtures i. argon-methane mixturess*, Nucl. Instr. and Meth. **A 247** (1986).

[GUP14] S K GUPTA, *High energy astroparticle physics at ooty and the grapes-3 experiment*, Proc Indian Natn Sci Acad (2014).

[IA95] J.LamasValverde D.Hatzifotiadou M.C.S.Williams I.Crotty, E.CerronZeballos and A.Zichichi, *The wide gap resistive plate chamber*, Nucl. Instr. and Meth. **A 360** (1995), no. 512.

[Jan] Jeremy Janney, A Guide to Garfield, .

[Kno10] Glenn F. Knoll, *Radiation detection and measurement*, John Wiley Sons, Inc., 2010.

[Leo87] William R Leo, *Techniques for nuclear and particle physics experiments: A how-to approach*, Springer-Verlag, 1987.

[LP69] J. J. Lowke and J. J. Parker, *Theory of electron diffusion parallel to electric fields. ii: Application to real gases*, Phys. Rev. (1969), no. 181 302.

[MAH12] RUPAK MAHAPATRA, *Dark matter direct detection with supercdms soudan*, PRAMANA - journal of physics **79** (2012), no. 5.

[Maj02] Pawel Majewski, Sand-Glass: a novel position sensitive micro-pattern gaseous detector for ionisation and X-ray radiation, 2002, .

[Man] Paul Mantsch, *Building the pierre auger observatory*.

[Nec] Maria Monica Necchi, *Resistive plate chambers: from high energy physics to biomedical applications*.

[NQE09] Glaser M Perumal M Arstad E Nguyen QD, Smith G and Aboagye EO, *Positron emission tomography imaging of drug-induced tumor apoptosis with a caspase-3/7 specific [18f]-labeled isatin sulfonamide*, Proc Natl Acad Sci USA **106** (2009).

[RAM39] SIMON RAMO, *Currents induced by electron motion*, Proceedings of the I.R.E. (1939).

[Ref] Cosmic rays: particles from outer space, `https://home.cern/about/physics/cosmic-rays-particles-outer-space`.

[Rie02] Werner Riegler, *Induced signals in resistive plate chambers*, Nucl. Instr. and Meth. **A 491** (2002).

[Sau77] F. Sauli, *Principles of operation of multiwire proportional and drift chambers, cern 77–09, geneva*.

[SC81] R. Santonico and R. Cardarelli, *Development of resistive plate counters*, Nucl. Instrum. Meth. A **187** (1981), no. 377.

[SC15] D Speller and SuperCDMS Collaboration, *Dark matter direct detection with supercdms soudan*, J. Phys.: Conf. Ser. (2015), no. 606 012003.

[Sch] Heinrich Schindler, Microscopic Simulation of Particle Detectors, .

[S.F99] S.F.Biagi, *Monte carlo simulation of electron drift and diffusion in counting gases under the influence of electric and magnetic fields*, Nucl. Instr. and Meth. **A 421** (1999).

[Sku68] H R Skullerud, *Monte carlo calculation of electron transport coefficients in counting gas mixtures i. argon-methane mixturess*, J. Phys. D: Appl. Phys. **1** (1968).

[Sta] Johanna Stachel, Detectors in Nuclear and Particle Physics, .

[Sta08] Giacomo D'Ali Staiti, *The argo-ybj experiment in tibet*, Nuclear Instruments and Methods in Physics Research Section A (2008), no. 588 (2008) 7–13.

[79a] Jean-Marie *et al.*, *Systematic measurements of electron drift velocity and study of some properties of four gas mixtures: A-ch4, a-c2h4, a-c2h6, a-c3h8*, Nucl. Instr. and Meth. (1979), no. 159 213.

[79b] L. G. Christophorou *et al.*, *Fast gas mixtures for gas-filled particle detectors*, Nucl. Instr. and Meth. (1979), no. 163 141.

[99] R. Arnaldi *et al.*, *Study of resistive plate chambers for the alice dimuon spectrometer*, Nucl. Phys. B (Proc. Suppl.) **78** (1999), no. 84.

[04] A.N. Akindinov *et al.*, *Space charge limited avalanche growth in multigap resistive plate chambers*, Eur Phys J **C 34** (2004), no. 512.

[06a] A.Akindinov *et al.*, *The mrpc detector for the alice time of flight system: Final design and performances*, Nuclear Physics B **158** (2006).

[06b] G. Belli *et al.*, *Rpcs in biomedical applications*, Nuclear Physics B **158** (2006).

[09a] A. Colaleo *et al.*, *The compact muon solenoid rpc barrel detector*, Nucl. Instr. and Meth. **A602** (2009), no. 674.

[09b] R. Arnaldi *et al.*, *Final results of the tests on the resistive plate chambers for the alice muon arm*, Nucl. Instr. and Meth. **A602** (2009), no. 740.

[10a] D N McKinsey *et al.*, *The lux dark matter search*, J. Phys.: Conf. Ser. (2010), no. 203 012026.

[10b] W.D.Apel *et al.*, *The kascade-grande experiment*, Nuclear Instruments and Methods in Physics Research Section A **620** (2010).

[vCLaK] von Christian Lippmann aus Kronberg/Ts., *Detector physics of resistive plate chambers*.

[Veea] Rob Veenhof, &CELL: SOLIDS, `http://garfield.web.cern.ch/garfield/help/garfield_19.html#Ref0183`.

[Veeb] ———, Complete Garfield help file, `http://garfield.web.cern.ch/garfield/help/garfield_full.html`.

[Veec] ———, DRIFT: methods, `http://garfield.web.cern.ch/garfield/help/garfield_79.html$#$Ref0673`.

[Veed] ———, Garfield - simulation of gaseous detectors, `http://garfield.web.cern.ch/garfield/`.

[Vee93] ———, *Garfield, a drift-chamber simulation program, user's guide, version 4.29*.

[Vee09] ———, *Numerical methods in the simulation of gas-based detectors*, JINST (2009).

[VP12] UNAM Mexico V. Peskov, *Challenges for rpcs and resistive micropattern detectors in the next few years*, XI Workshop on Resistive Plate Chambers and Related Detectors (2012).

[Wal08] Christopher W. Walter, *The super-kamiokande experiment*, arXiv:0802.1041v1 [hep-ex] (2008).

[Wil04] M.C.S. Williams, *Space-charge limitation of avalanche growth in narrow-gap resistive plate chambers*, Nucl. Instr. and Meth. **A 525** (2004), no. 512.

[WR03] Rob Veenhof Werner Riegler, Christian Lippmann, *Detector physics and simulation of resistive plate chambers*, Nucl. Instr. and Meth. **A 500** (2003), no. 512.